ABSTRACT

Title of Document:	HEAT DISSIPATION IN CURRENT CARRYING MULTIWALLED CARBON NANOTUBES
	Norvik Voskanian Kordi, Doctor of Philosophy 2014
Directed By:	Professor John Cumings, Department of Materials Science and Engineering

Understanding thermal transport is of great interest in combatting the excess heat generated in current electronic circuits. In this dissertation we provide insight and progress in thermal transport in current carrying MWCNT. Chapter 1 gives an overview of the work presented in this dissertation, quickly discusses the motivation for studying heat dissipation in current carrying carbon nanotubes, and outlines the key findings. The chapter outlines the unique remote heating phenomena observed in Joule heated MWCNTs, as well as, the process in which the research led to the discovery of a detection method for near-field heat transfer. The physical properties of carbon nanotubes are discussed in Chapter 2 and the relevant heat transfer mechanisms are introduced. Chapter 3 outlines some of the previous experimental work in studying thermal properties of nanotubes. The results presented in this dissertation rely on previously measured thermal conductivity and thermal contact resistance for nanotubes and thus a discussion of these results is critical. The

fabrication process for the measured devices is presenter in Chapter 4. In addition, chapter 4 provides a detailed discussion of the measurement technique employed to probe the thermal properties of the devices presented in Chapter 5 and 6. Chapter 5 discusses the findings in regard to heat dissipation for a current carrying MWCNT supported on a SiN substrate. The results provide definitive proof of substrate heating via hot electrons; a process which can not be explained using traditional Joule heating model and requires the presence of an additional remote heating mechanism. Analysis of the results indicate a reduction in remote Joule heating which led to a series of controlled experiments presented in Chapter 6 in an effort to study substrate thermal conductivity, k_{SiN}, variations as a function of voltage. In this chapter we outline the experimental and simulated results which indicate the remarkable ability of our technique to detect near-field thermal radiation. The enhanced thermal transport via near-field radiation is of great interest for scientific and engineering purposes but its detection has proven difficult. This thesis provides evidence of the sensitivity of the electron thermal microscopy technique to measure near-field radiation.

HEAT DISSIPATION IN CURRENT CARRYING MULTIWALLED CARBON NANOTUBES

By

Norvik Voskanian Kordi

Dissertation submitted to the Faculty of the Graduate School of the
University of Maryland, College Park, in partial fulfillment
of the requirements for the degree of
Doctor of Philosophy
2014

Advisory Committee:
Professor John Cumings, Chair
Professor Liangbing Hu
Professor Bao Yang
Professor YuHuang Wang
Professor Yifei Mo

Dedication

To my parents, for their love and support.

Acknowledgements

First and foremost I would like to thank my advisor Prof. John Cumings. He has been extremely supportive and has guided and motivated me throughout the past 5 years. He is a remarkable scientist and teacher and has always been open to discuss new ideas. Most importantly, I have consistently been amazed at his ability to quickly come up with ideas to resolve problems.

I would like to thank all the members in the Cumings group at Maryland. I would like to specially acknowledge Kamal Baloch and Merijntje Bronsgeest who collaborated with me in my research. I would like to thank Kamal Baloch for sharing his knowledge and training me as a new graduate student. Merijntje has been a great colleague and has been generous with her time and I've enjoyed and benefited from our discussions. Hanna Nillson has been a great help and collaborator. I have sat next to Jeremy Ticey and Khim Karki the past few years, they have been great colleagues and better friends. I would also like to thank Stephen Daunheimer, Paris Alexander, Jasper Drisko, Vladimir Oleshko, and Kai He for their friendship and help throughout the past 5 years.

Most of all, I would like to thank my family. They have been extremely supportive of me and I owe everything to them. My Mom and Dad for always encouraging me and my sister for always being there for me.

Table of Contents

List of Tables

List of Figures

Chapter 1: Introduction

The size of electronics has been consistently decreasing since the invention of the transistor in efforts to increase operation speeds and frequencies of devices. However, the imposed geometric constraints have given rise to a number of issues, such as increasing temperature, which must be managed to ensure stable device operation. Therefore, there needs to be a detailed understanding of thermal transport in the nanoscale to improve on the present heat management technologies.

As the size of the material approaches the phonon mean free path, the conventional heat transfer mechanisms must be altered to incorporate new physics at the nanoscale. At these regimes, there are additional means of heat transfer mechanisms, such as near-field radiation, which can be utilized in designing thermal management devices. In addition, material at the nanoscale exhibit unique thermal properties, which can be incorporated in future technologies.

Carbon nanotubes, CNTs, are one such example which are considered to have some of the highest thermal conductivity of any known material. Many experimental approaches have been used in studying their thermal properties but there still remains a great deal of unanswered questions regarding their heat dissipation mechanism and their interaction with surrounding material, quantified by their thermal boundary resistance, *TBR*.

In this work, we explore the heat dissipation from a current carrying CNT to a SiN membrane. The study relies on observing the temperature gradient across the SiN membrane by Joule heating a MWCNT on its surface. The temperature gradient of

the supporting membrane is inferred from the solid to liquid transition of indium, In, islands as they undergo phase change at 429 K. Previous work [1] using this technique has explored the relative thermal contact resistance between CNT and SiN membrane. It was observed that due to the small contact area between the nanotube and the substrate there is a very large *TBR*, 250 $m.K/W$, which indicates that a CNT will serve as an inefficient heater for a supporting flat surface. However, it was observed that the *TBR* can be drastically reduced, to 4.2 $m.K/W$ by increasing the contact area by covering a portion of the nanotube with Pd. The *TBR* measurements quantified thermal transfer between the nanotube and substrate by elevating the temperature of the CNT passively, via a connecting joule heated metal wire.

The technique was also employed to study heat dissipation in actively heated CNTs, where the nanotube is biased using electrical contacts connected to its ends. From the previous *TBR* experiments, one would expect that the majority of the heat in the nanotube will be dissipated via the contacts at either end and thus the islands under the Pd pads will melt first. However, experimentally, melting at the center of the nanotube was observed, suggesting an improved thermal coupling. To further explore heat dissipation in current carrying nanotubes, a cross nanotube geometry is designed for the present studies which indicates heating of the substrate in the current carrying region of the nanotube. Simulations of the cross nanotube device, based on conventional conductive heat transfer model, fail to replicate the experimental temperature gradient across the membrane. To match the experimental results, the model is altered to include an enhanced energy dissipation from the energetic

electrons in the nanotube to the substrate, which indicate a remote Joule heating of the substrate [2].

To study the dependence of the phenomena on the bias voltage of the electrons, the melting profile is evaluated for a range of biases. Preliminary simulations suggest that the amount of remote Joule heating decreases for increasing voltages, which seems counter intuitive, since the nanotube conductance is increasing in the experimental voltage range, suggesting an increase in population of hot electrons. To explore the nature of a decreasing amount of remote joule heating, a control experiment is conducted to ensure that there are no other bias dependent changes in the thermal properties of the device which have not been considered in our simulations. As such, a simple Pd heater wire device is designed and the heat dissipation is evaluated over a range of voltages. At a given voltage, heat transport from the Pd to the SiN substrate can be quantified using conductive heat dissipation and relies on the thermal conductivity of the interacting lattice structure. However, comparison of substrate thermal gradient at each voltage step indicates monotonic change in the thermal properties of the material, mainly the thermal conductivity of the SiN, k_{SiN}. With the simulations, the results point to an increasing k_{SiN} for increasing voltage.

To explore the origin of variation in thermal properties of the material, a number of contributing factors are evaluated. Effects of temperature, stress, TEM electron beam, and variation in thermal conductivity due to individual In islands are considered, all of which failed to explain the change in the thermal properties. It was observed that an explanation for such a variation in the k_{SiN} must incorporate a spatial

dependence. One plausible explanation that would be manifested as a spatial dependent k_{SiN} is the presence of near-field radiation which is strongest near the heat source and weakens at increasing distances. Quantifying heat dissipation due to near-field radiation is extremely difficult and demonstrating the ability of the imaging technique in conducting such measurements is of great interest.

This PhD work demonstrates conclusive evidence for remote Joule heating of SiN membrane via a current carrying MWCNT. In addition, the work provides preliminary evidence for the sensitivity of the imaging technique to measure near-field heat dissipation across the surface of the membrane, although further modeling may be necessary to understand these results.

Chapter 2: Background

In recent years, carbon nanotubes (CNTs) have been proposed to play a large role in creating new thermal management systems. Their unique thermal [3] and electrical [4] properties have made them a candidate to be incorporated in future transistor technologies [5-7]. Others have suggested integrating CNTs in present transistor designs to facilitate improved heat management [8].

2.1 Motivation

The consumer and market demands for faster, cheaper, smaller and more energy-efficient electronics are greater than ever and continue to grow. The industry has successfully maintained Moore's law by consistently increasing the number of transistors that fit on integrated circuit [9]. However, in order to maintain this trend and continue to shrink the size of the transistor we need to have a better understanding of the physical phenomena that occur in these dimensions.

From the smallest handheld devices, to the largest servers, all electronic systems require transistors, all of which use silicon-based technology. In these devices, a large percentage of the input power is lost in the form of heat. Solving this problem is crucial in preventing device failure caused by overheating and overcoming the barrier of achieving high current densities. Moreover, cooling devices requires additional energy, which becomes problematic as energy costs continue to increase. These issues provide motivation for a better understanding of heat transport at the nanoscale and development of better thermal management techniques.

There are two strategies for developing better thermal management techniques: (1) efficiently moving heat away from a region, requiring materials with high thermal conductivity, or (2) thermally isolating a region, which requires materials with low thermal conductivity. The use of carbon nanotubes (CNTs) is a potential solution in combating the heat problem, due to their high thermal conductivity. This requires knowledge not just of the inherent properties of the CNT, but also an understanding of the mechanism by which the CNT will be connected to the rest of the device, such as their interfacial thermal resistances.

2.2: Heat transfer at the nanoscale

The exchange of thermal energy in matter is governed by the second law of thermodynamics as two objects will exchange heat to maximize their entropy by reaching thermal equilibrium, moving heat from hot to the cold reservoir.

2.2.1: Conductive Heat Transport

In the simplest case, conductive heat transport is described in terms of Fourier's Law, $Q = -k\nabla T$, where Q is the heat flux, k is the thermal conductivity and ∇T is the temperature gradient. The total thermal conductivity of a solid is the sum of the thermal conductivity of the electrons, k_e, and the phonon thermal conductivity, k_l; such that $k = k_e + k_l$. In non-metals, phonons are responsible for the majority of heat transport, where in particular phonons with small wavelengths (1-100nm at room temperature) contribute the most to the heat transfer [10]. Based on the Boltzmann equation, the phonon thermal conductivity can be expressed as

$$k_l \approx \frac{1}{3} l v_g c_v = \frac{1}{3} \tau {v_g}^2 c_v \quad (2.1)$$

where l is the phonon mean-free path, v_g is the group velocity, c_v is the phonon heat capacity and τ is the relaxation time [11]. Consequently, phonon transport depends greatly on the carrier scattering mechanisms, including scattering within the material as well as interfacial scattering. It is therefore not surprising that thermal transport has a more complex behavior in nanoscale devices.

The role of interfaces and their influence on heat dissipation has been a subject of extensive studies since 1940s, when Kapitza explored the interfacial thermal resistance in liquid helium [12]. The induced thermal impedance at the interface between two materials is commonly referred to as the thermal boundary resistance (*TBR*). As an extension of the Fourier's Law, *TBR* can be expressed as

$$R_{th} = \frac{(T_2 - T_1)}{Q} \quad (2.2)$$

where T_2 and T_1 are the temperatures on the either side of the interface and Q is the heat flux created due to the temperature gradient [13].

There have been a number of theories developed to explain the phenomenon including the acoustic-mismatch (AM) model and the diffusive-mismatch (DM) model [12]. In the AM model there is no scattering at the interface and the impedance arises due to a mismatch in the propagation of sound speeds resulting in a mismatch in the acoustic impedances. Alternatively, in the DM model the scattering probability is a function of the available phonon density of states. Despite the information that the present models provide, it is difficult to predict experimental results using these theories. There still remains a need to extract the *TBR* value experimentally as it can have great implications on managing the heat generated in electronics, specifically,

for current carrying nanowires that are used in the manufacturing of integrated circuits.

2.2.2: Near-Field Radiation

All matter with a finite temperature, $T > 0$, radiate energy as electromagnetic waves. Based on quantum mechanics, the source of this radiation can be understood by the energy loss of electrons as they transition from their energy state, E_2, to a lower energy state E_1, emitting a photon in the process. The interaction of the emitted photon with other matter can be explained in terms of absorption, transmission, or reflection [14].

The principle of radiative heat transfer is generally described based on an idealized emitter, known as a black body, which constitutes an object that absorbs all incident electromagnetic radiation. Conventionally, the concept of black body radiation is expressed in terms of Max Planck's law of black-body radiation and Wilhelm Wien's displacement law [15,16]. Planck's law characterizes the spectrum of electromagnetic radiation from a black body in terms of the wavelength, λ, and frequency, v, and Wien's displacement law demonstrates the dominant λ for a given temperature. However, Planck's law is based on the fundamental assumption that the distance, d, between radiating bodies is much greater than the wavelength of the radiation [17]. Consequently, one must differentiate between the mechanism of radiative heat transfer for bodies with large separation, $d >> \lambda$, known as far-field regime, and for bodies with distances less than the wavelength of the emitted radiation, $d < \lambda$, commonly known as the near-field regime [18].

In the far-field limit, the radiation is understood as the propagation of electromagnetic waves due to the thermal and quantum fluctuations of the emitting material. However, this fluctuations also generate evanescent waves which propagate along the surface. It is possible to ignore the contribution of these surface waves in the far-field regime since they decay exponentially with increasing distances from the heat source. However, at small distances, the contribution of the evanescent waves can dominate the thermal transport mechanism and thus must be included in the model of heat dissipation. The nature of the evanescent waves in sub-micron dimensions is explained in terms of photon tunneling [19].

From classical optics, described by Snell's law, it follows that an electromagnetic wave at the boundary of two media can be completely reflected if its angle of incident is greater than the critical angle, a process known as total internal reflection. Although the reflected wave carries no energy across the second medium, it travels as an evanescent wave across the boundary. However, if a third medium is placed within the decay length of the evanescent waves, an energy transfer process can occur, which is commonly referred to as phonon tunneling. Consequently, at dimensions below the characteristic wavelength of thermal radiation, there may be considerable enhancement in the heat transfer mechanism [20].

2.3: Carbon nanotubes

Since Ijima's 1991 paper [21], there has been a great deal of interest in carbon nanotubes. However, other groups had observed evidence of CNTs since the 1950s, visualized using transmission electron microscopes [22]. The research conducted over

the years has shown that the structure possesses some very unique and desirable mechanical, electrical, and thermal characteristics and, for these reasons, CNTs have become a popular candidate to be incorporated in future technologies [23, 24].

2.3.1: Lattice Structure

Carbon nanotubes are cylindrical nanostructures from the fullerene structural family and are formed as a monolayer of graphite, graphene, is rolled into a hollow tubular structures. They can either be single walled (SWCNT) or multi-walled (MWCNT) in which case the nanotube consists of multiple rolled graphene layers, with 3.4 $\AA$ interlayer distance [25].

The structure of graphene is based on the hexagonal arrangement of carbon atoms in a single layer with sp^2 chemical bonding [26]. The direction in which the CNT is rolled, specified by its chiral vector $\boldsymbol{C_h}$, defines the chirality of the nanotube.

$$C_h = na_1 + ma_2 \tag{2.3}$$

where a_1 and a_2 are the lattice vectors of graphene [27] and n and m denote the number of unit vectors. Since $\boldsymbol{C_h}$ is one of the main defining parameters for the structure of a nanotube the indices *(n, m)* are used to specify its chirality; CNTs are classified as armchair for *(n, n)* indices and zigzag for *(n, 0)* indices.

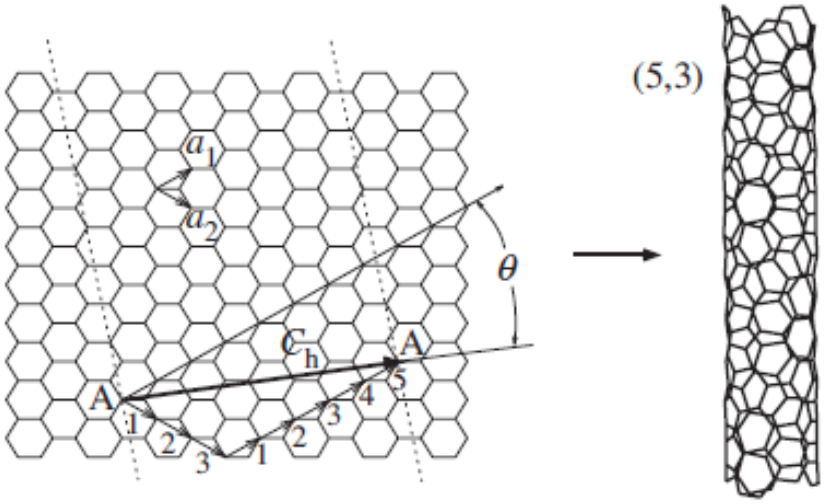

Figure 2.1: Structure of a honeycomb graphene lattice and rolled-up CNT, with the nanotube defined by the vector C_h [25].

2.3.2: Electric Properties

Carbon nanotubes, much like graphene, have unique electronic properties. Graphene is considered a zero-bandgap semiconductor, a semi-metal, since it can be either semiconducting or metallic [28]. The conduction of electrons in the material can be understood from the behavior of the Fermi energy E_F evaluated as a function of wavevector k, figure 1.2.

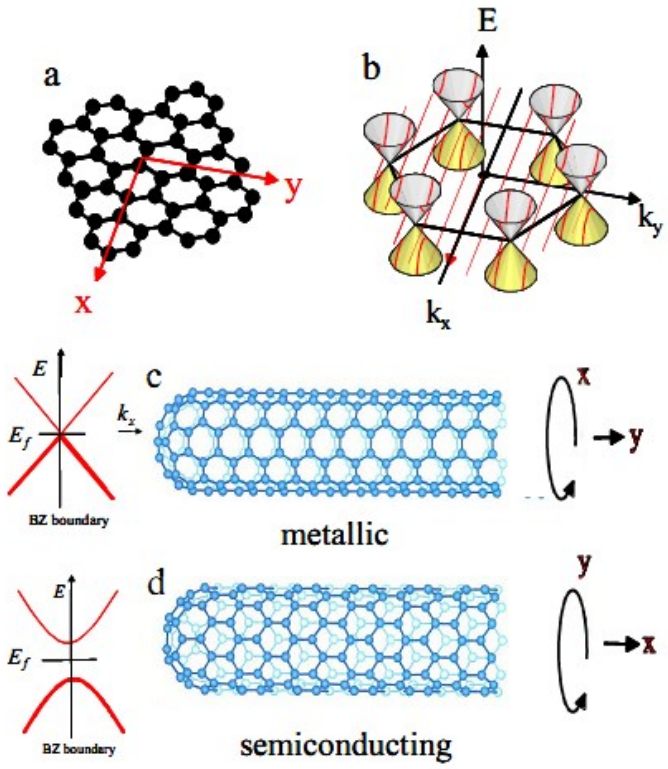

Figure 2.2. (a) Honeycomb lattice of graphene. (b) Energy dispersion in graphene. Depending on how the graphene sheet is rolled the CNT can be either (c) metallic or (d) semiconducting [28]

The band structure of graphene demonstrates that the conducting states exist only at specific points, at which the material is metallic. Outside these sites the material has an energy band gap similar to a semiconductor due to backscattering of electrons by the atoms in the lattice [28]. In CNTs, the rolling of the graphene sheet imposes a periodic boundary condition on the wavefunction, quantizing k_n, and its 1-D band structure is represented as a slice through the graphene cones [29].

Consequently, depending on the tube axis, and thus the chirality, the nanotube will be either metallic or semiconducting. Armchair nanotubes, with *(n, n)* indices are metallic while other CNTs are semiconducting. MWCNTs are almost always metallic for statistical reasons, since it only takes one metallic SWCNT inside to make the

CNT metallic as a whole. Metallic nanotubes are of extreme interest due to their ability to maintain very high current densities, on the order of 10^9 A/cm^2 [30, 31].

2.3.3: Thermal Conductivity

Another characteristic of CNTs is their high thermal conductivity, they have been shown to have thermal conductivity as high as 3000 *W/m.K* [32]. Due to their high long-range crystalline order and long phonon mean free path, it is believed that CNT's can have thermal conductivity exceeding that of diamond [33].

At low temperatures the thermal conductivity is dominated by the following four acoustic modes: two transverse modes, a longitudinal mode, and a torsional mode [34]. The corresponding increase in heat capacity due to rising temperature, coupled with the long phonon mean free path results in a linear increase in thermal conductivity as shown by J. Hone [35, 36]

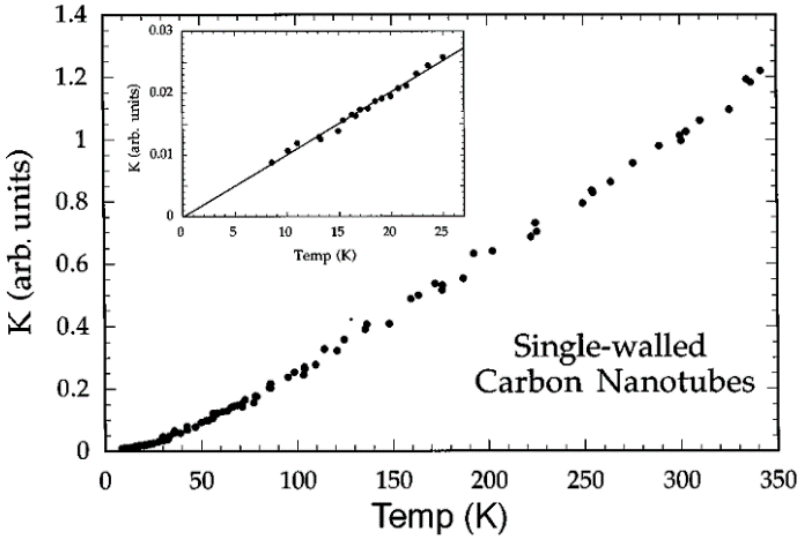

Figure 2.3. Increase in thermal conductivity of SWCNT from 8 K to 350 K [35].

With increasing temperature, the optical phonon modes begin to contribute, which further increases the k_{CNT}. The domination of the optical phonons causes a rapid increase in conductivity and becomes nonlinear as the specific heat follows a $T^{1.5\text{-}2.5}$ trend [36]. The behavior is seen above 8 K for SWCNT as the energy of the system exceeds the energy gap of the lowest optical modes, $\hbar\omega_{op}$ [37]. The slope and the starting temperature for this trend differs for MWCNTs since $\hbar\omega_{op}$ depends on the radius and chirality of the nanotube. As the temperature further increases, thermal conductivity reaches a maximum as phonon scattering begins to dominate, resulting in a reduction of k_{CNT}.

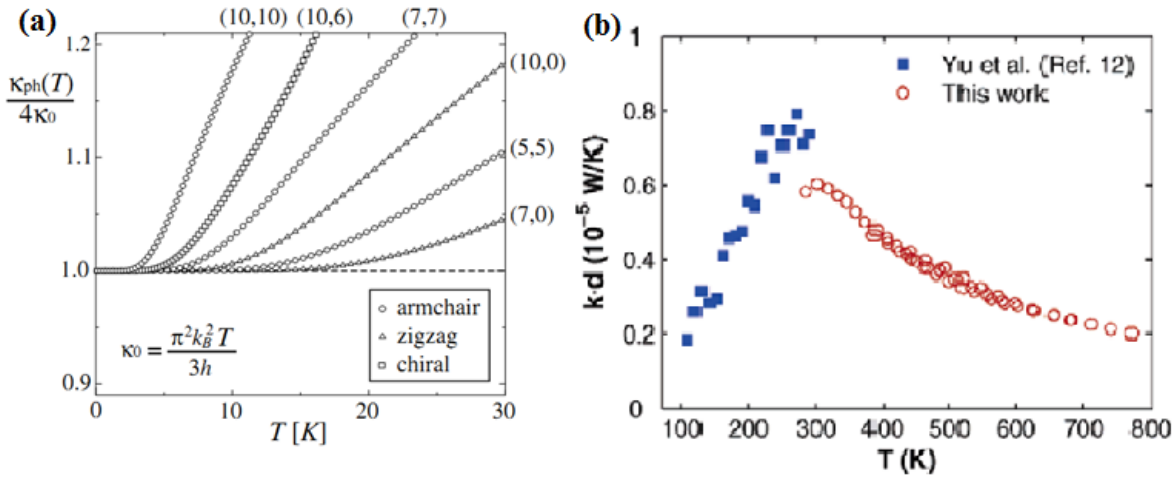

Figure 2.4: (a) At low temperatures the thermal conductivity increases due to contribution of additional optical modes [36]. (b) Demonstrates the reduction of thermal conductivity due to increase in phonon scattering at elevated temperatures [38].

The regime which exhibits minimal phonon scattering along the length of the nanotube is known as the ballistic regime. In this regime, the k_{CNT} will not demonstrate a length dependence. However if the CNT is longer than the phonon mean free path, the diffusive regime, the k_{CNT} will decreases as a function of CNT

length due to the increase in phonon scattering [38]. Consequently the transition from the ballistic regime to the diffusive regime will depend on the length and temperature of the CNT as shown by Eric Pop in 2006.

2.3.4: CNT-CNT Junction TBR

Understanding the total thermal conductivity, k_{CNT_total}, of multiple CNTs in contact with each other becomes increasingly difficult as it depends on a number of additional variables, most important of which is their orientation relative to each other. It is clear that a poor contact between individual nanotubes will result in a drastic reduction in the k_{CNT_total} due to the increase of the CNT-CNT interfacial thermal boundary resistance. The TBR will depend on the contact area which makes perpendicular and parallel oriented CNTs have the lowest and highest k_{CNT_tota} [39] respectively. Additionally, the thermal contact resistance will depend on the structure of the CNTs and the distance between them. In CNT junction systems, the added pressure may deform the structure of the CNT thus increasing or decreasing the contact area accordingly. Simulation results have shown [39] that the deformation increases the contact area for perpendicular nanotubes while decreasing it for parallel CNT-CNT systems. Moreover, the induced pressure increases the van der Waals bonding stiffness which leads to an increase in junction thermal conductance. Another contributing factor to the high contact resistance is the increase in phonon scattering and the junction site.

Despite the many difficulties in studying CNT junction thermal conductance it is without a doubt that there is a very large junction thermal contact resistance which

leads to a much lower k_{CNT_total} compared to the thermal conductivity of an individual CNT.

2.3.5: CNT – Bulk material (TBR)

For practical reasons, understanding the thermal properties of carbon nanotubes requires considering the *TBR* between CNTs and connecting materials. Panzer and Goodson [40] demonstrated that the change in geometry from 1D system to a 3D or a 2D system modifies the phonon modes that participate in energy transmission and may be a source of increased *TBR*. They found that longitudinal phonons will dominate phonon transmission across the interface and transverse phonons will have minimal effect.

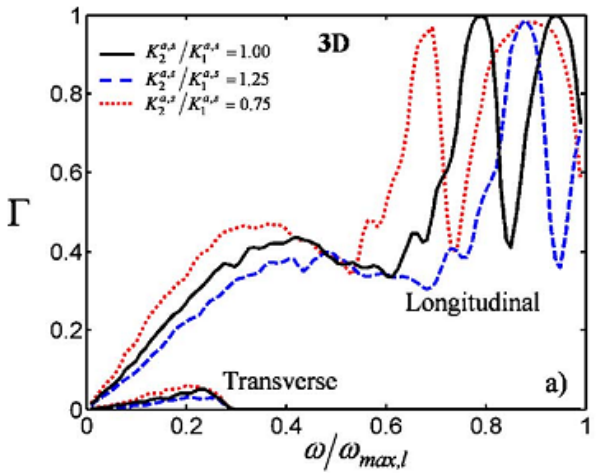

Figure 2.5. Transmission coefficient for longitudinal polarizations incident on a junction of 1D and 3D system dominates over the transverse polarization. [40]

The *TBR* also depends on the contact area and the van der Waals interaction between the nanotube and the connecting material [41]. Work by Hertel and Avouris [42] have demonstrated that the van der Waals interaction between a nanotube and a supporting substrate depend on the tube diameter and the number of shells. The

contact area of the nanotube is inversely proportional to the *TBR*. In the case of a nanotube in contact with a flat material the contact resistance, R_c, can be expressed as:

$$R_c = \frac{1}{w\pi k_{CNT}} \ln\left(\frac{2D}{b}\right) - \frac{1}{2wk_{CNT}} + \frac{1}{\pi w k_{sub}} \ln\left(\frac{D}{\pi b}\right) \quad (2.4)$$

Where D is the nanotube diameter, b is the contact area, w is the length of the contact region, and k_{cnt} and k_{sub} are the thermal conductivity of the CNT and the flat substrate respectively [43]

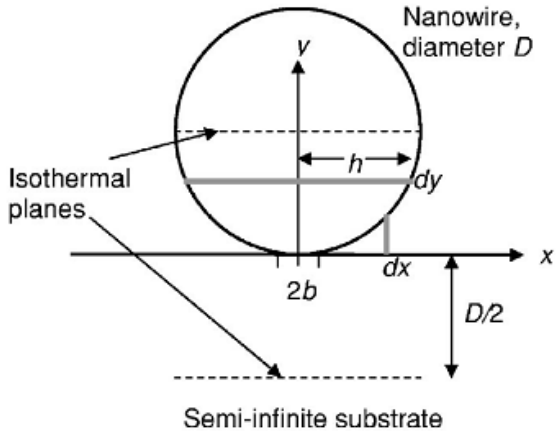

Figure 2.6: The contact area of a CNT-Substrate system responsible for heat conduction [43].

2.3.6: Substrate Phonon Scattering

Heat dissipation from a CNT is governed by its thermal contact resistance with its surrounding, as discussed above. However, in the case of a current carrying nanotube the interaction of the charge carriers with lattice phonons can also contribute to the dissipation process. At low biases the electron mobility in CNTs is considered to be ballistic. However, as the electrons gain more energy in the high bias regime they begin to undergo a backscattering process with the optical phonons thus

causing a reduction in mobility [44]. The optical phonon energies, $\hbar\omega_{OP}$, in graphene and nanotubes are calculated to be around 160-200meV [45] (seen figure 2.7) and thus the electrons must be accelerated to have sufficient energy to interact with the nanotube phonons.

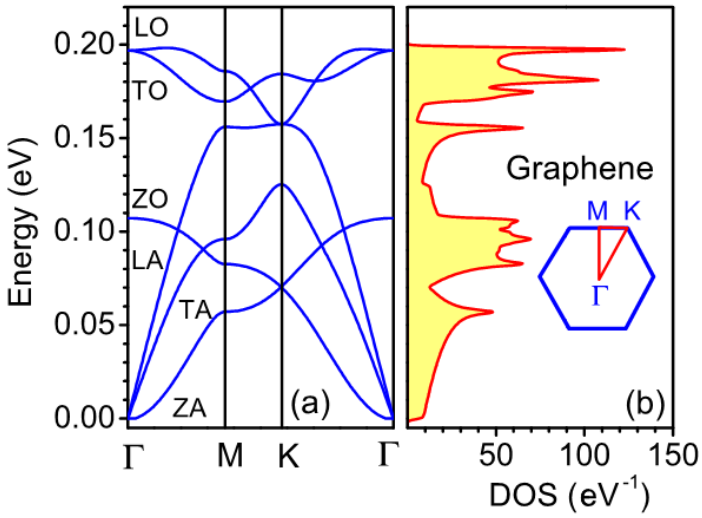

Figure 2.7: (a) Graphene phonon energies. (b) The phonon density of states of graphene [45].

Recent theoretical work [46] suggests that the presence of certain electromagnetic surface modes in the vicinity of a current carrying nanotube can introduce an additional heat dissipation mechanism. The surface EM modes required for such a transfer process necessitate the presence of a supporting polar substrate, which support surface phonon polaritons (SPP) with frequencies close to their optical phonons frequencies. Since the substrate optical phonon energy is considerably lower than the CNT $\hbar\omega_{OP}$ it would be favorable for the hot charge carriers to release energy into the SPP channel. Such a system would drastically limit the electron-phonon scattering within the nanotube while facilitating enhanced heat transfer to the

substrate, despite the large interfacial TBR. Even though there is great interest in characterizing such a phenomena, there has been little experimental verifications of it, with the exception of work published in 2013 in Nature Nanotechnology [2], and there are many unanswered questions regarding the properties of such a transfer mechanism.

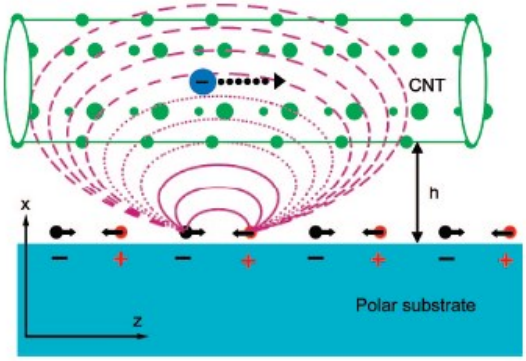

Figure 2.8: Schematic demonstrating the interaction of the hot electron in the nanotube with the EM field of the polar substrate [2].

Chapter 3: Thermal metrology of CNT

There are many difficulties in conducting experimental studies of heat transfer in carbon nanotubes. Most experimental studies could be categorized in two groups. Either via self-heating of nanotube, *active heating*; or using external heat sources, *passive heating*, to generate a temperature gradient across the nanotube [47].

3.1: Passive Heating Studies

3.1.1: Microdevices

One way to generate a temperature gradient across a CNT is by using microfabricated devices [48]. Kim et al. pioneered the use of microfabricated resistive elements to study thermal properties of individual suspended MWCNTs. In this technique, two Pt thin film resistors, R_h and R_s, are fabricated and biased individually with a MWCNT suspended in between them, shown in the inset of figure 3.1.

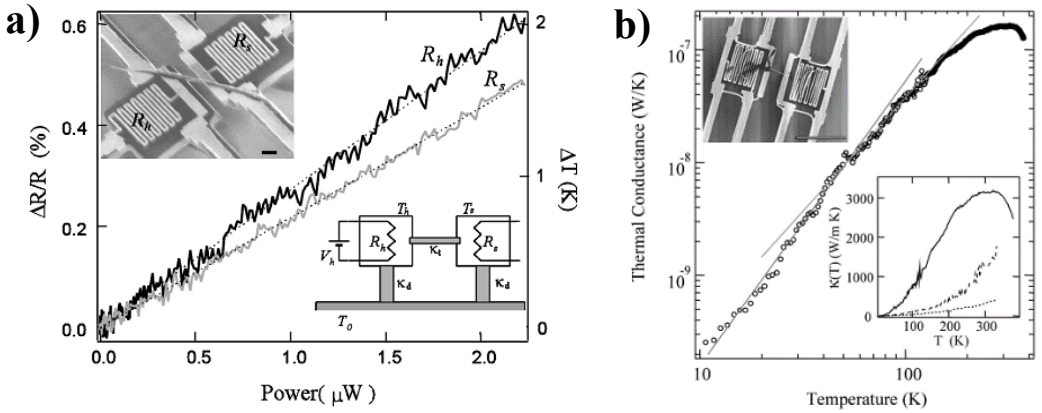

Figure 3.1: (a) The change in the resistance of the heater, R_h, and the sensor, R_s, as a function of applied power is shown. (b) The measurements are used to calculate the thermal conductivity of the nanotube [48].

The resulting temperature increase due to joule heating of the Pt resistors creates a temperature gradient across the suspended nanotube. Additionally, since electrical resistance changes as a function of metal temperature, due to increase in

scattering events, the temperature of the either side of the nanotube can be extracted from the resistance of the Pt. By applying a potential V_h on R_h, the metal is heated to temperature T_h. The MWCNT facilitates heat transport to the Pt metal on the opposite side raising its temperature to T_s. Using the technique, the group was able to extract the thermal conductivity of the nanotube, k_{CNT}, from

$$T_h = T_0 + \frac{K_d + k_{CNT}}{K_d(K_d + 2k_{CNT})} P \qquad\qquad T_s = T_0 + \frac{k_{CNT}}{K_d(K_d + 2k_{CNT})} P$$

where P is the joule power applied to R_h, T_0 is the initial equilibrium temperature, and K_d is the thermal conductivity of the Pt resistors supporting material. For a 2.5 μm long nanotube with diameter of 14 nm the group found that k_{CNT} = 3000 $W/m.K$ at room temperature (see figure 3.1b). Additionally, the thermal conductivity demonstrated a temperature dependence, which was discussed and explained in Chapter 2. The same technique was used to extract the thermal conductivity of SWCNTs with different diameters, which showed that k_{CNT} increased from 3000 $W/m.K$ to 9000 $W/m.K$ for decreasing nanotube diameters [33].

An intrinsic problem with using the mentioned micro-fabricated resistor technique is the inability to isolate the effect of CNT-heater contact TBR from the conductivity measurements. Thus the k_{CNT} value extracted represents a lower limit. Michael Pettes and Li Shi estimated the TBR between the CNT and the Pt electrodes to be 78-585 $m.K/W$ and were able to show a decrease in the contact resistance by deposition of amorphous Pt-C composites, by effectively increasing the contact area [49].

CNT	k_{CNT}	Reference
MWCNT	3000 W/(mK)	[48]
SWCNT	3000 – 9000 W/(mK)	[33]
MWCNT	50 – 350 W/(mK)	[49]
SWCNT	600 W/(mK)	[49]
SWCNT	2000 W/(mK)	[50]

Table 4.1 shows the room temperature thermal conductivity values extracted using this technique.

The results support that CNTs have very high thermal conductivity with SWCNTs showing higher thermal conductivity than MWCNTs. The results by Pettes [49] were attributed to the low quality of their CVD grown CNTs which indicate the influence of phonon scattering due to defects.

3.1.2: Optical Measurement

As mentioned, the inability to separate the CNT TBR may be the main reason for the large variety in the thermal conductivity measurements extracted from microdevice experiments [50]. To remedy this issue, Hsu et. al. used a laser as an external power source to heat suspended nanotubes and monitor their temperature change through shifts in the G band Raman frequency [51]. Since the frequency downshift of the G band corresponds to the lengthening of the C-C distance [52], it is possible to characterize the temperature of the nanotube based on induced thermal expansion due to heat generated from the laser. From the technique one is able to extract a ratio between the TBR and the intrinsic nanotube thermal resistance as well as monitoring the mechanism of phonon transport.

Using a 532 *nm* laser with a 0.36 μm diameter spot size, a 4.7 μm suspended SWCNT was heated while simultaneously the G band Raman frequency along the

length are measured at different laser powers. The change in temperature, ΔT, is then extracted from the temperature induced shift in the G band frequency as seen in figure 3.2.

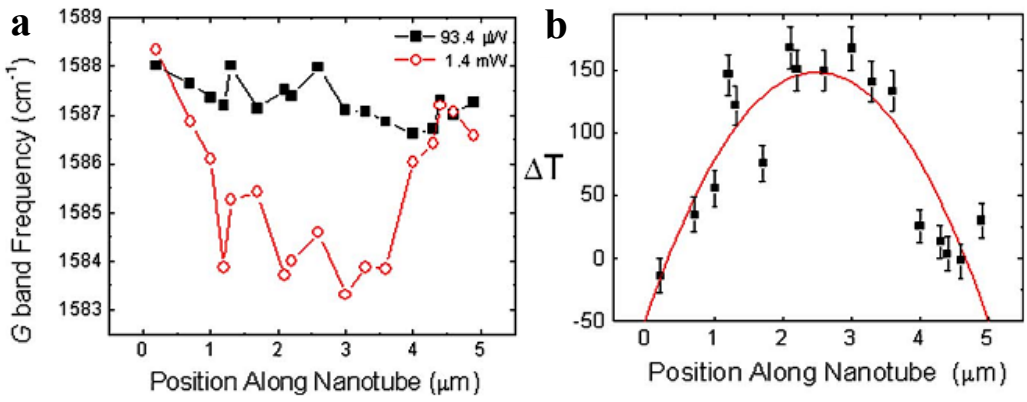

Figure 3.2: (a) G band Raman frequency measurements. (b) The temperature profile of the suspended nanotube extracted from the corresponding shift in the G band [6].

Considering diffusive phonon transport with negligible *TBR* at the contacts, the change in the nanotube temperature can be expressed as $\Delta T(x) = \frac{Q}{k_{CNT}AL}(-x^2 + Lx)$, where A and L are the cross sectional area and the length of the CNT respectively. Furthermore, by considering a contact TBR it is possible to modify the governing CNT temperature equation and extract the ratio between the CNT and contact thermal resistance. Using this method, Hsu et. al. extracted a ratio between 0.02 to 17.

3.2: Active Heating

To study Joule heating phenomena in material, one must have a good understanding of material's electrical and thermal properties. In particular, their thermal conductivity and contact resistance with the surrounding area need to be well defined. Consequently it is necessary to attain information regarding the temperature as well as electrical power dissipation within a given material. Characterizing the electrical dissipation can be accomplished by evaluating the *I-V* measurements with high precision. However, the temperature profile is much harder to obtain and requires special tools or techniques to measure.

3.2.1: Raman

As described in the section 3.1.2 it is possible to use the shift in the G band frequency to deduce the temperature change of nanotube. However, instead of using an external heating source, such as a laser, it is possible to heat the nanotube directly via Joule heating [53, 54]. An advantage of this technique is its ability to isolate the effect of contact resistance from the thermal conductivity measurements. Like the optical measurement technique, the nanotube is suspended across a gap with only the ends connected to the electrode and positioned on the substrate (see figure 3.3). Similarly, the temperature profile can be extracted by measuring the shift in the G band frequency, both at the suspended region and near the contacts. Consequently, by simply subtracting the temperature at the contacts, it is possible to extract a k_{cnt} value that does not include the TBR. The technique was successfully used by Qingwei Li et.

al. for measuring the thermal conductivity of MWCNT and SWCNT, for which they extracted values of 1400 W/mK and 2400 W/mK respectively [55].

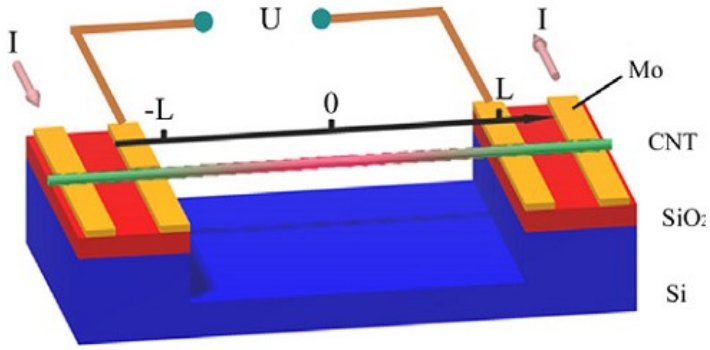

Figure 3.3: Schematic of conducting Raman measurements on a suspended Joule heated nanotube [55].

3.2.2: Electric Breakdown Method

Experimental observations have shown that nanotubes under high bias breakdown [56, 57] and in the case of biased MWCNTs the measured current drops as individual walls disintegrate at approximately 900 K. By assuming a well-defined breakdown temperature for a given nanotube it is possible to use the mechanism as a thermal probe.

The technique has been extensively used to study suspended and supported SWNTs [58]. In addition, by burning individual shells in a MWCNTs, their thermal and electrical properties have been explored [56]. In the experiments I-V measurements are carried out across the nanotube. Although the behavior of the I-V curves varies for different device designs and nanotube types, they all share abruptly terminate at high biases when the breakdown occurs. A drawback of the method is its reliance on knowing the breakdown temperature. At elevated temperature, the peeling of the walls of nanotubes is associated with the oxidation of the outermost carbon

shells. For a pure carbon graphitic material the oxidation requires extremely high temperatures, which are unlikely to be reached via joule heating. It is more likely that the breakdown is the consequence of current-induced defect formation. [56]. Consequently, the technique is relying on the applied current instead of the temperature of the CNT, which makes the extracted thermal effects more model-dependent.

3.2.3: 3ω

The *3ω* method is a common technique used in measuring the thermal conductivity of thin films [59]. Applying an *AC* current at frequency ω to a resistor, $I_{AC} = I_0 sin(\omega t)$, produces joule heating at frequency *2ω* and a *2ω* fluctuation in the resistivity measurements. In turn the change in resistivity is manifested in the voltage measurement as *3ω* fluctuation, which can be expressed as a function of the thermal conductivity of the substrate the resistor rests on. By fabricating a heater wire resistor on thin films it is possible to extract the k_{sub} from careful voltage measurements.

Similarly, it possible to use the *3ω* technique to extract the thermal conductivity of a CNT. However, such measurements require the CNT to be suspended and not in contact with the substrate along its length, with only the end contact point thermally secured to the system. In such a set up the $V_{3\omega}$ can be expressed as:

$$V_{3\omega} = \frac{\sqrt{2} I_0^3 R R' L}{\pi k_{CNT} A} \qquad \tan(\varphi) = \frac{2\omega L^2}{\pi^2 \alpha}$$

Where *R* is the resistance of the nanotube, *A* and L are its cross-sectional area and length, *α* is the thermal diffusivity, and *φ* is the phase lag of the *3ω* signal [60].

Experimental measurements of CNT thermal conductivity using this technique have shown a room temperature thermal conductivity of approximately 3000 *W/m.K* [38].

3.2.4: Joule Heating

As discussed above Joule heating of individual nanotubes is a viable technique to induce a temperature gradient across them. In such measurements characterizing the electrical properties of the nanotube is relatively easy and can easily be quantified using the direct *I-V* measurements. However, information regarding the temperature profile of the nanotube is much more difficult to attain and requires clever techniques, some of which have already been described in this chapter. Alternatively, it is possible to evaluate the temperature of the nanotube directly from the electrical measurements given a well characterized relationship between temperature and resistance of the CNT.

Consequently, the thermal properties of SWCNT have been studied by evaluating their electric behavior during Joule heating. In one study [61], individual SWCNTs were suspended from Pt contacts, with 2 μm separation, and biased up to 1.5 *V*. By suspending the nanotube and thermally isolating it from a substrate the heat can be assumed to be conducted entirely along the length of CNT. Therefore, any change in the electrical properties of the nanotube can be considered to be direct consequence of the temperature variations. The resistance of the SWNT can be defined in terms of the electron mean free path, λ, using the Landauer-Buttiker approach,

$$R(V,T) = R_C + \frac{h}{4q^2}\frac{L+\lambda_{Total}(V,T)}{\lambda_{Total}(V,T)},$$

and the temperature profile of the system can be computed using the heat conduction equation

$$A\nabla(k\nabla\mathrm{T}) + I^2(R - R_C)/L$$

Using this system of equations, it is possible to relate the electrical properties of the nanotube to its thermal properties. Consequently, using a finite elemental model the experimental parameters were simulated by using the thermal conductivity of the nanotube as a free parameter. From this technique, a temperature dependent thermal conductivity was extracted for the nanotube which indicate a 1/T dependence with thermal conductivities ranging from 3500 to 1000 *W/m.K*.

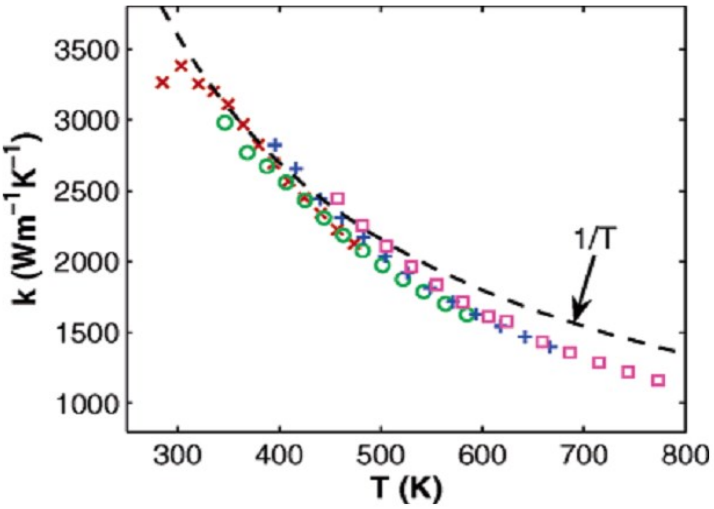

Figure 3.4: The reduction of nanotube thermal conductivity as a function of increasing temperate [61].

The problem in using this technique is that the results are valid only if the model used is correct, an assumption which can not be independently verified for the entire temperature spectrum. Also, the model used relies on several parameters that are difficult to characterize. Alternatively, it would be more convenient to measure the temperate of the CNT directly.

3.2.5: Scanning thermal Microscopy

Li Shi et al used a nano thermocouple to directly measure the temperature across a joule heated nanotube [62]. The technique employs a custom fabricated AFM tip from a combination of Pt and Cr which together act as a thermocouple. By scanning the tip across the length of the nanotube, it is possible to extract its thermal profile.

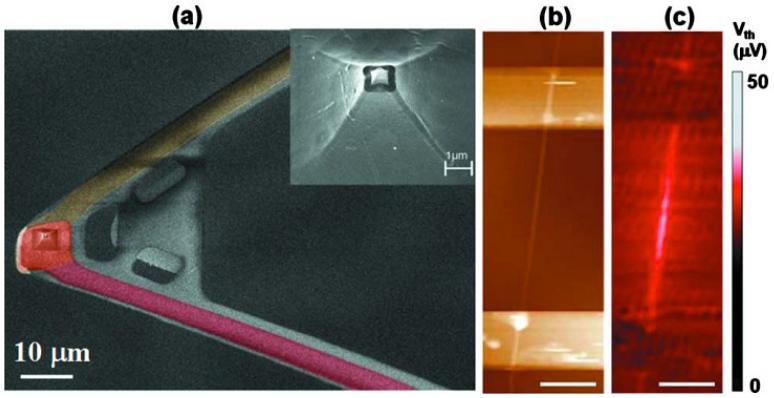

Figure 3.5: (a) SEM image of the thermocouple probe, with the false color representing the position of the different metals (Pt and Cr). (b) AFM image of the nanotube and (c) its corresponding thermal image at 0.73V and 20.1 μA current [62].

The scanning thermal microscopy technique was employed to study the temperature profile of both Joule heated SWCNT and MWCNT supported on SiO_2 substrate. In both cases it was observed that the maximum temperature occurs at the middle of the nanotube, suggesting a diffusive heating of the CNT. However, the temperature gradient near the center is much higher for the MWCNT as compared to the SWCNT. This is attributed to the poor thermal contact resistance between the MWCNT and the supporting SiO_2, which effectively forces most of the heat to be conducted away through the electrodes. The higher thermal contact resistance of the

MWCNT as compared to SWCNT is due to the larger nanotube diameter which in turn reduces the effective contact area with the substrate.

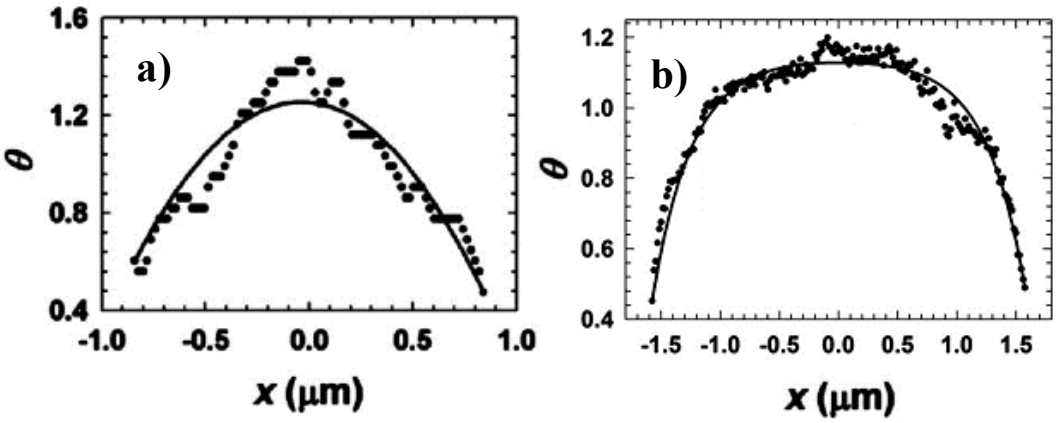

Figure 3.6: (a) Dimensionless temperature profile along the length of a (a) MWCNT and (b) SWCNT. [62]

3.3: Electron Thermal Microscopy

To overcome the shortcomings of present metrology techniques, a measurement system was developed and optimized for the present work to study nansocale heat dissipation in a transmission electron microscope (TEM) based on the solid-to-liquid phase transition of Indium (In) islands.

To characterize and test the reliability of the imaging technique, the heat dissipation of a Joule-heated Pd heater wire was evaluated. A 30 *nm* thick, 54 *nm* wide, and 870 *nm* long Pd heater wire was fabricated on top of a 100 *nm* thick SiN membrane. Using an external *DC* power supply connected to the sample by a custom built TEM holder, the Pd wire was gradually biased from 0 to 250 *mV*. The induced joule heating creates a temperature gradient across the membrane and as the temperature of the membrane reaches the melting point of In, 156 ^{o}C, the islands begin to melt [63].

The islands melt beginning at the center of the wire, consistent with the Joule heating model. By ramping the voltage, the heater wire temperature increases and more islands begin to melt. Figure 3.7 shows the melting profile of the islands as a function of applied current, measured from the power supply, where the color shows the current that the islands melted. In additional to providing qualitative understanding of heat dissipation the experiment serves to quantitatively characterize the heat dissipation. By simulating the experimental setup using finite element analysis and matching it to the experimental results it is possible to extract precise values of the device's thermal or electrical properties.

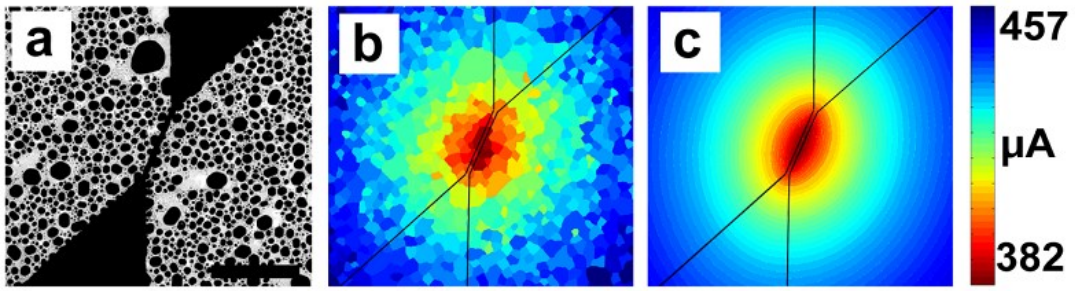

Figure 3.7: (a) TEM image of a heater wire device, the dots in the image are the In islands. (b) Experimental thermal map, the colors correspond to the current at which a given island melts. (c) Simulated melting profile from finite element analysis software. [63]

By monitoring the current and voltage values throughout the experiment it is possible to extract the resistivity and the thermal coefficient of resistivity, TCR. Through an iterative process and by matching the experimental current density the TCR was found to be $1.8 \pm 0.1 \times 10^{-3}\ K^{-1}$. With the extracted resistivity values the thermal conductivity of the metal can be deduced from the Wiedemann-Franz law. Consequently, with all parameters known, the thermal conductivity of the SiN can be

set as a free parameter and varied to match the melting profile, which gives a value of 3.6 *W/m.K* [63].

Using the electron thermal imaging technique, thermal properties of CNT have been studied both by passively heating them and actively heating them.

3.3.1: Passive – Prior Work

Individual MWCNTs are heated using a Pd heater wire fabricated on SiN membranes. Due to the large thermal conductivity of the nanotube, the entirety of the nanotube quickly reaches thermal equilibrium. By observing the heat dissipation to substrate, the TBR of CNT system can be reliably extracted.

A Pd heater wire was fabricated on top of a MWCNT such that the heater wire was oriented at 90^{o} relative with the nanotube and it was positioned such that the nanotube was on one side of it (right in the image). In a Pd heater wire the melting profile is symmetrical. However, since the nanotube quickly reaches thermal equilibrium, it can more efficiently facilitate heat transport into the substrate. Thus depending on its thermal contact resistance with the SiN, it will cause an asymmetry in the melting profile of the In islands. The lack of asymmetry in the experimental results is an indication of a very high thermal contact resistance between the CNT and membrane. Using finite elemental analysis technique the value of 250 *m.K/W* was extracted. This is largely due to the small contact area between the nanotube and the membrane as discussed in 2.3.5.

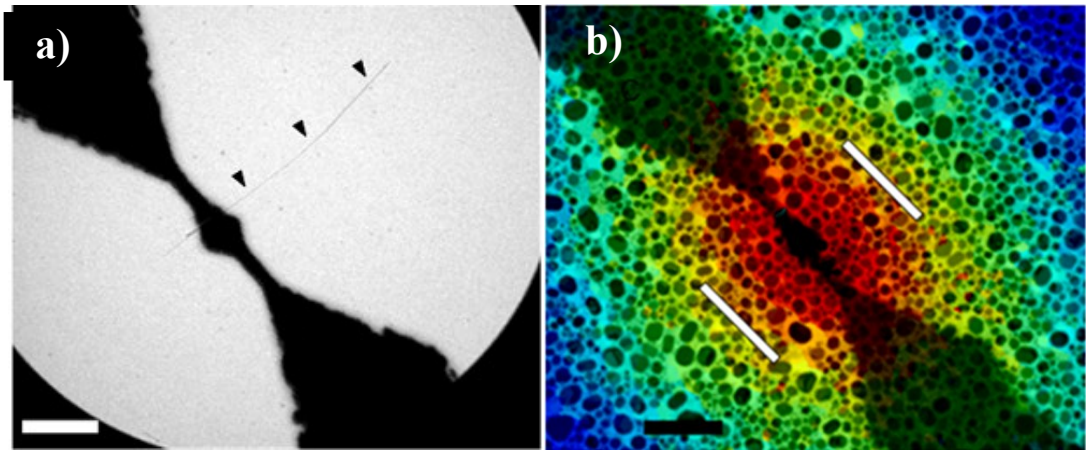

Figure 3.8: (a) TEM image of a passive CNT device. (b) Experimental thermal map of the passive device [1].

To increase the contact area, Pd was deposited on top of the CNT, seen in figure 3.9, as before, the heater wire was biased and the melting profile was observed for asymmetry. With the addition of the Pd patch a small but distinct asymmetry was observed which suggests a reduction in thermal contact resistance (see figure 3.9b). This can be explained in terms of contact area, as the Pd deposited on top of the CNT drastically increases the contact area.

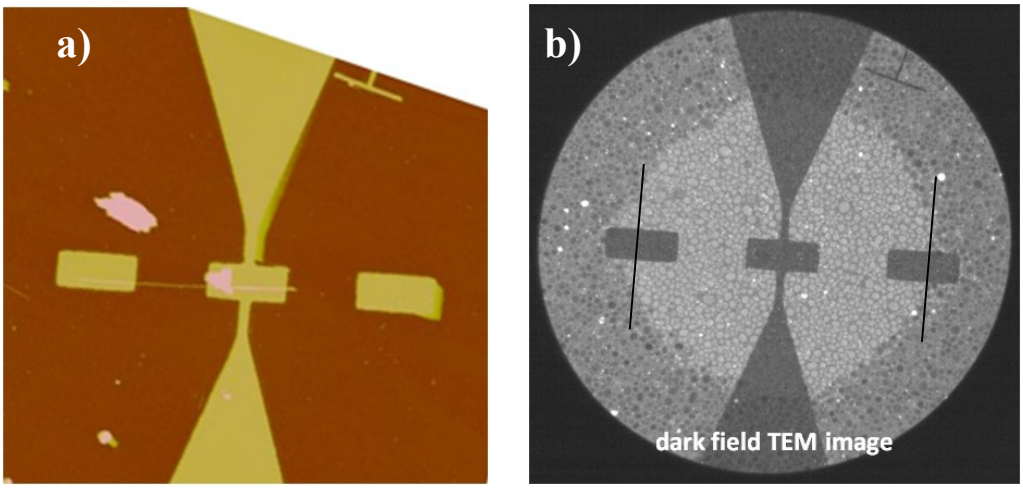

Figure 3.9: (a) AFM image of a thermally anchored CNT passive device. (b) Melting profile of the In islands, with the black lines indicating a noticeable

asymmetry due to reduction in thermal contact resistance (image courtesy of Merijntje Bronsgeest).

3.3.2: Joule Heating of CNT– prior work

Additionally, the technique was used to study heat dissipation in a MWCNT by directly biasing the nanotube [2]. Based on the extracted TBR values from the passive experiment when the nanotube is biased, it will heat up and reach thermal equilibrium. Due to the high CNT-SiN TBR the nanotube will have a difficult time dissipating its heat to the substrate. The much lower TBR of Pd-SiN system will cause most of the heat to be dissipated in those regions. Therefore, it is expected to see islands melt under the Pd electrode first, but the opposite is observed and the islands under the middle of the CNT melt first.

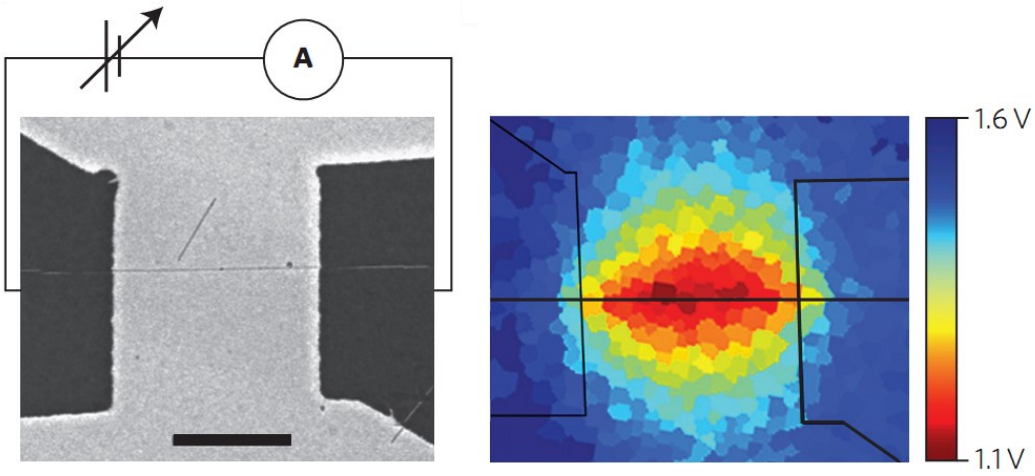

Figure 3.10: TEM image of an actively CNT device with its corresponding thermal map [2].

It is possible that, when biasing the nanotube, we are in a different temperature regime and there are different means of heat dissipation which cause much lower *TBR* between the CNT and the membrane. To test this hypothesis, a different device was made, in which a MWCNT was again biased. However, only a

small section of the nanotube was biased while the rest of it stretched on the substrate and was anchored down by Pd, as shown in figure 3.11. In this system the nanotube should heat up again to the same temperature regime and due to its high thermal conductivity it should quickly reach thermal equilibrium. Also, because of the increased contact area from the Pd anchor and its distance away from the heat sinking of the electrodes the islands under the anchoring Pd should melt first. However, it was experimentally observed that the islands under the biased regions melted. Additionally, no asymmetry was seen towards the patch which suggests that the nanotube was cold as it wasn't moving any heat towards the patch. This means that the heat generated due to the electrons is heating the substrate to the melting point of In while the nanotube stays cold. This is most unusual as it contradicts traditional Joule heating process. One possible hypothesis is that the electrons are coupling with the surface polaritons more efficiently and thus heat the substrate directly instead of heating the nanotube.

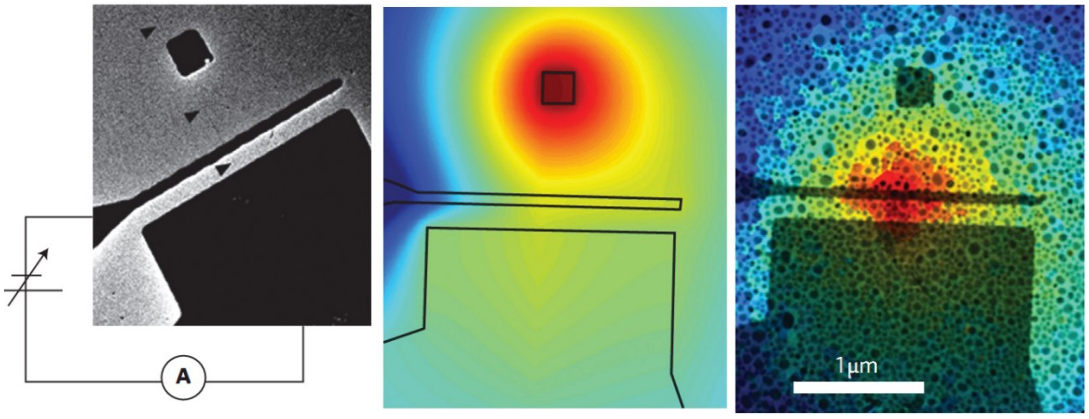

Figure 3.11: (a) TEM image of the nanotube device, showing applied bias to only a small section of it. (b) Simulations of heat distribution across the membrane. (c) Experimental temperature gradient across the membrane [5].

3.4: Conclusion

The work already presented by Baloch et. al. provided initial evidence for the remote heating of a supporting membrane [2], previously only predicted to exist in theoretical models [46]. Taking advantage of such a transport mechanism could be extremely beneficial in designing future nanoscale thermal management devices. Consequently, it is of great scientific and engineering interest to carefully examine and fully characterize the phenomena. The inability to explain the experimental results using a traditional Joule heating model suggests the presence of a remote heating mechanism. In such a model, the amount of heat dissipated is expected to depend on the energy of the electrons and thus should depend on the bias voltage. Evaluating the voltage dependence of the heat dissipation would help in validating the model in addition to providing valuable insight into the overall effect.

Furthermore, Baloch et. al. concluded that at least 84% of the electrical power supplied to the nanotube is dissipated directly into the substrate. Quantifying the exact power dissipation requires a precise understating of the thermal properties of the device. Here, we present new work to address both of these problems. We will present work examining the bias dependence of heat transport in actively biased CNT devices in Chapter 5, and then we will move on to a more detailed study of the thermal transport properties of the nanoscale structures and materials that comprise these devices in Chapter 6, with an eye toward providing better quantitative measures for the remote Joule heating effect.

Chapter 4: Experimental technique and device fabrication

The electron thermal microscopy technique employed in these experiments relies on capturing the solid-liquid phase transition of the In islands on the back of the SiN membrane. Operating the TEM in the appropriate dark field condition, one is able to see a contrast between the molten and solid In islands. The islands are able to retain their shape due to a surrounding oxide layer, and by observing the melting profile of the islands for the different voltages it is possible to generate a thermal map for a given experiment [63]. These techniques have also been used for prior studies of CNT, as described in the previous chapter [1,2].

4.1: Transmission Electron Microscope

A transmission electron microscope (TEM) operates much like an optical microscope with the exception of having an electron source as opposed to a light source. It employs the interaction of the electrons with a sample to produce a magnified image and other information about the sample. In conventional optical microscopy there is a fundamental limit to the resolution, based on the wavelength of the light source. Even an ideal optical microscope cannot resolve images smaller than few hundred nanometers as its resolution, d, is diffraction limited [64]. The resolution, d, can be expressed as a function of the wavelength, λ, by

$$d \approx \frac{\lambda}{2NA}$$

where NA is the numerical aperture of the system.

In 1930s, based on advances in quantum mechanics, the wave nature of the electron fueled many new scientific hypothesis. Realizing that the De Broglie

wavelength of electrons is much smaller than that of light many suggested that it would be possible to overcome the diffraction limited resolution of an optical microscope by employing an electron source, thus drastically improving the imaging resolution to atomic scales [65]. Additionally, progresses in cathode ray technologies led the way for the development of electromagnetic lenses used in focusing electron beams. Consequently, it became possible to manipulate an electron beam and focus it as first electron microscope were conceived. Over the years, there has been many improvement in TEMs, drastically improving their resolution and giving them additional functionalities to characterize different materials. In some imaging modes, the resolution can be as good as 0.05nm, but it is still limited by the aberrations (imperfections) in the lenses [67].

4.1.1: Components – Electron Beam

The operation of TEM relies on the generation of stable electron current, either via thermionic or field emission process. In a thermionic emission process, the material is heated to a temperature where the electrons energy exceeds its work function. Tungsten filaments are common sources for thermionic emission electron microscopes. However, the low work function, high emissivity, and long lifetime of lanthanum hexaboride (LaB_6) makes them a better candidate for TEMs [66]. In field emission systems (FEG) a potential is applied to a fine tip, typically tungsten wire, with a very small radius which in turn reduces the work function barrier and facilitates electron tunneling. Typically, a FEG system produces a more monochromatic electrons, however the low operational cost of a LaB_6 system has made them the most popular source used in TEMs.

4.1.2: Components – Lenses

Similar to an optical microscope, the resolution of the microscope is dependent on its ability to focus. In a TEM a series of electromagnetic lenses placed in the column are used to manipulate and form a focused electron beam, based on the Lorentz force. Before the beam reaches the sample it is important to align it and prepare it for the appropriate imaging condition. To this end a number of lenses, called condenser lenses (C1, C2, ..) are used to either converge or make the electron beam from the source parallel. Since not all the beams coming from the electron source can be collected using the lens, an aperture is often used to limit the incoming electrons and thus improve the imaging quality. After the beam passes through the specimen the objective lens is used to focus the beam. The objective lenses are the most important component of the TEM and usually have very strong magnetic fields which should be taken under consideration when imaging magnetic materials. As a final step, the projector lens expands the beam such that a magnified image can be seen [67].

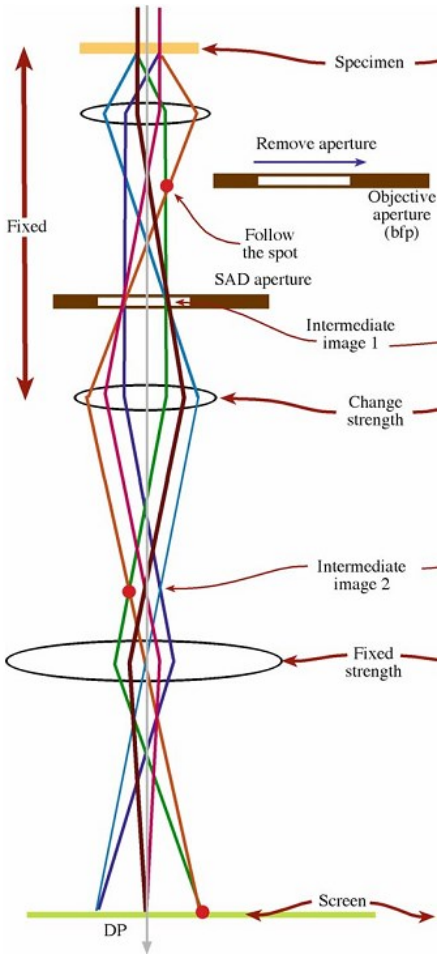

Figure 4.1: Simplified ray diagram showing the interaction of the lenses with the electron beam for the basic operation condition of a TEM [67].

4.1.3: Imaging Mode

Under normal conditions, an aligned and focused TEM provides an image of the sample from the unscattered electrons. However by manipulating the beam, it is possible to record a diffraction pattern which can yield information about the crystal structure of the sample. Using a selected-area diffraction (SAD) aperture, it is possible to exclude the undesired electrons from appearing on viewing screen, which can yield a much more useful diffraction pattern.

A SAD pattern contains both the scattered and unscattered electrons from the sample (see figure 4.2). The image is called a bright field (BF) image if it is formed from the unscattered electrons. On the other hand, if the image is formed only from the scattered electrons, it is called a dark field (DF) image. One can operate the TEM in the DF condition by either moving the objective aperture, displaced aperture DF (DADF), or by tilting the beam to only select the desired scattered electrons [68]. A disadvantage of using DADF is the induced aberration and astigmatism caused by selecting electrons that travel off the optical axis (figure 2b). Consequently, depending on the desired DF conditions the further the objective aperture is moved the more drastic the image distortion will be. Alternatively, it is possibly to tilt the beam such that the incident electrons hit the specimen at an angle equal and opposite to the scattering angle, (figure 2c). In this mode the electrons will be aligned with the optical axis and make it easier to focus on the DF image [67].

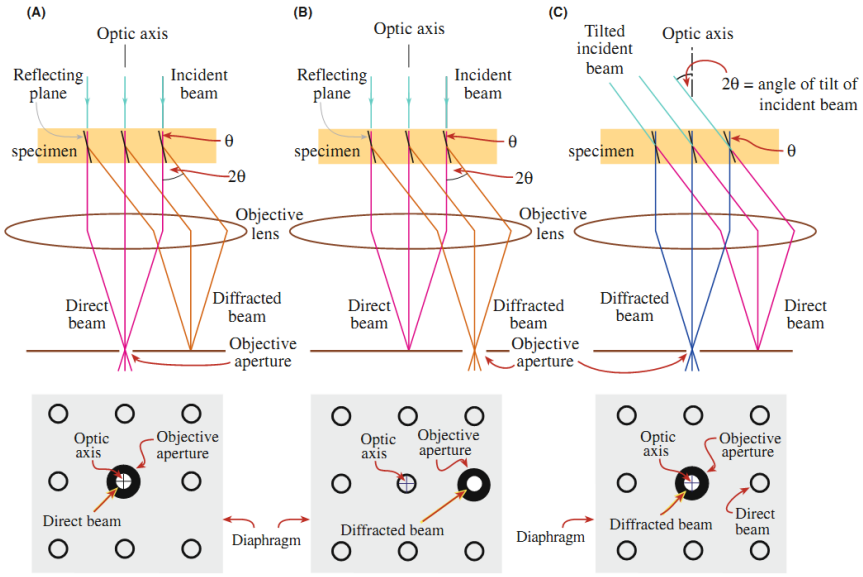

Figure 4.2: (a) showing the TEM conditions to produce a BF image. (b) and (c) show the required condition for taking a DF image, either by using the objective aperture or by tilting the beam.

4.2: Thermal Imaging

4.2.1: Method and Calibration

A remarkable benefit of DF imaging is its ability to differentiate between materials of solid and liquid phase as their crystal structure changes due to phase transition. It is possible to see evidence of this change in the crystalline structure in a TEM by observing the difference in the scattered electrons from the lattice. Figure 4.3 shows a composite diffraction image of solid and liquid indium (In) metal on an electron transparent SiN membrane. From the image, it is clear that imaging the In in BF mode, using the unscattered electrons, it will be impossible to differentiate between solid and liquid In. However, electrons scatter differently from solid In as compared to liquid In, thus by imaging the metal in the DF condition, by selecting the scattered electrons, it is possible to gain information about the phase of the island by observing differences in the contrast [63].

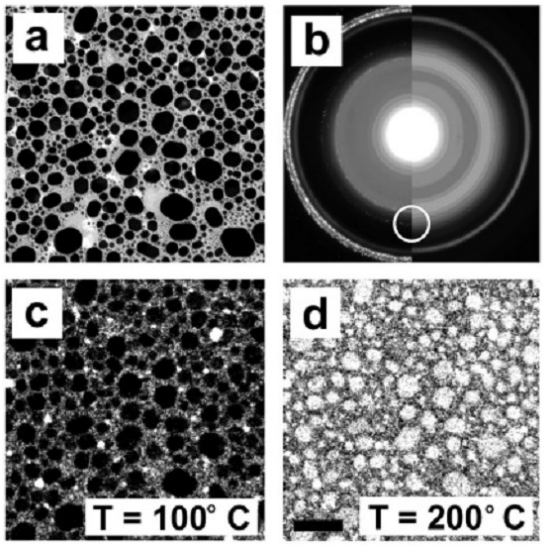

Figure 4.3: (a) TEM image of the In islands taken at the BF condition. (b) Composite diffraction pattern of solid (left) and liquid (right) In islands. DF images, (c) and (d) show the observed contrast difference for the solid and liquid In islands respectively.

A notable characteristic of In is that when deposited in thin layers, it coalesces in the form of small hexagonal islands. Additionally, the surface quickly oxidizes in air, thus coating the islands by a thin oxide layer with a much higher melting point. Consequently, when imaging In islands, it is possible to heat them above their melting point while maintaining their shape. Additionally, the low vapor pressure of In allows the molten islands to not diffuse and thus it is possible to cool an island and solidify with no change in the structure of each island.

For the present study, the DF imaging condition was calibrated to find a tilt to show the maximum contrast between solid and liquid islands. To do this, half the islands in the field of view were melted and the beam was gradually tilted while simultaneously checking the contrast between the solid and molten In for each tilt angle. For thermal imaging on membranes of the same thickness and the same dimension In islands, the DF imaging condition do not change.

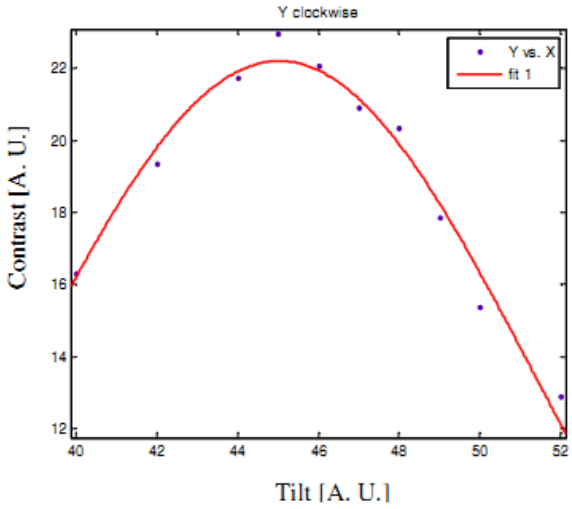

Figure 4.4: Calibration of the DF condition for a 50nm membrane, demonstrating the optimum tilt to achieve maximum contrast between solid and liquid islands.

Since In islands melt at 156.6 ºC, it is possible to use their solid to liquid phase transition as boolean thermometers. The temperature of the supporting substrate can be deduced by monitoring the phase of the In while imaging in DF conditions.

4.2.2: Beam Heating

In order to characterize the thermal profile of a given material, it is important to ensure that the measurement technique does not influence the temperature. Consequently, the influence of the beam on the sample must be put under careful consideration such that the imaging condition does not induce a temperature gradient which could affect the melting profile of the In islands. As such, the beam must be uniform in its intensity across the field of view and the imaging condition must be selected such that there is no beam heating from the energetic electrons.

The uniformity of the beam across the field of view can be simply addressed by avoiding the use of a fully-focused illumination. During high-magnification imaging, the electron source is fully focused and its image is formed at the specimen plane. In this setup the illumination diameter is less than one micron which is necessary for high-magnification imaging. However, to maximize the contrast of a crystalline sample or to record electron-diffraction pattern it is more useful to defocus the illumination such that the incident electrons form a parallel beam. The process of focusing and defocussing of the illumination is achieved by the manipulation of the second condenser lens (C2) which directly influences the current density at the specimen. As shown in figure 4.5, when fully focused the current density has an

approximately Gaussian shape with a maximum at the center of the optical axis. However, when defocused, such in the dark-field condition used for our electron thermal microscopy technique, the current density is uniform across the sample and any potential heating from the beam will also be uniform [66].

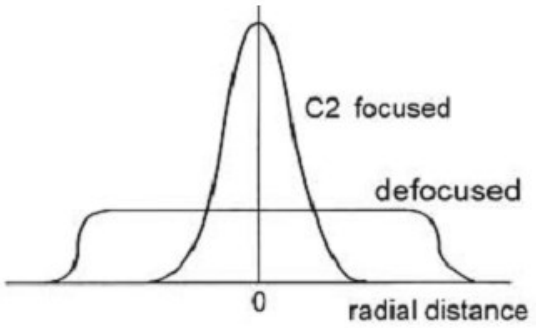

Figure 4.5: The current density as a function of distance from the optical axis for focused and defocused illumination [66].

To ensure that there is negligible beam heating, the beam effects were evaluated using a TEM heating holder. The holder uses a resistive heating element to heat the sample. With the use of the holder, the melting of In islands was monitored by increasing the temperature across the membrane. Due to the heat sinking of the supporting Si the effects of beam heating will be most prominent at the center of the free standing SiN and will diminish close to the edge of the membrane. To assess the effects of beam heating, the temperature required to melt the islands was evaluated for varying electron beam intensity. The condenser system allows the intensity of the emitted electrons to be altered, either by modifying the aperture or by changing the spot size. A condenser aperture works by limiting the amount of electrons that interact with the sample and as such directly reduces the intensity of the beam. On the other hand, the spot size reduces the beam intensity by varying the maximum energy

density of the beam by manipulating the focal point of the condenser lens. The melting point of the In islands at the center of the membrane were observed for different spot sizes in a JEM-2100 LaB6 TEM, with and without a condenser aperture [69].

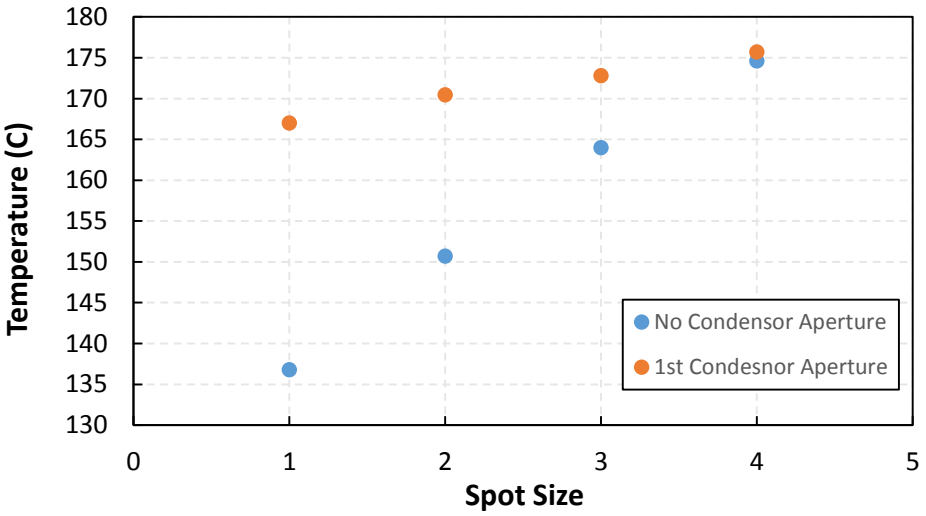

Figure 4.6: Heater temperature required to melt indium in the middle of a 50 nm thick SiN membrane, 250 µm square. At the edge of the membrane, the heater temperature required is 156 ± 1 ^{o}C, which is the accepted melting point for In.

At spot size 4, the melting of the Indium islands changed less than 1 ^{o}C regardless of the presence of a condensor aperture which indicates no beam induced heating on the sample. Consequently, from systematic study of the intensity effects, spot size 4 was chosen as optimum imaging condition to avoid the heating of the In islands by the electron beam.

4.2.3: Holder

Using a custom TEM holder with electrical contacts, it is possible to bias a sample and study its electrical properties inside a TEM. In addition, combining an electrical holder with the thermal imaging technique described above makes it

possible to study heat dissipation in a joule heating sample. This electron thermal microscopy technique provides in-situ real-time temperature measurement.

Using this technique joule heating behavior of CNT and metal wires on a SiN membrane were studied. The details of this holder are described in a previous research dissertation [69].

4.3: Device Fabrication

Using the in-situ TEM technique described above, it is possible to study heat dissipation of nanoscale materials. We have conducted a number of experiments exploring the thermal properties of metallic nanowires as well as MWCNTs. The devices examined are fabricated on 50 *nm* electron transparent SiN membranes in a multi-step process described below:

I. First the membrane is prepared for e-beam lithography, facilitating the patterning of alignment markers and the large electrical contact pads.

II. Next the patterns are coated with 30 *nm* of Cr/Au, which serve as a contact point between the electrical holder and the sample.

III. Following a successful liftoff procedure, MWCNTs are spin casted on the surface of the SiN membrane and their position relative to the alignment markers is evaluated using the TEM.

IV. To complete the circuit, the device is again patterned using e-beam lithography and additional Pd contact pads are created to connect the nanotube to the Cr/Au electrodes.

V. Finally, In is deposited at the back side of the membrane which serve as our temperature probes.

4.3.1: Patterning

All the samples studied are fabricated on commercially available 50 *nm* SiN membranes [70]. The membranes provide a 250 μm x 250 μm electron transparent SiN window supported on a 2.65 *mm* x 2.65*mm*, 200 μm thick silicon frame.

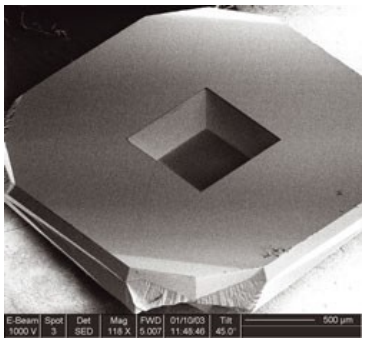

Figure 4.7: SEM image of the back side of the TEM membranes used in device fabrication [70].

Using electron beam lithography, electrical pads are patterned on the top surface of the membrane to fabricate electrical contacts. A positive resist bi-layer, using a combination of polymethyl methacrylate (PMMA) and its copolymer of methyl methacrylate (MMA), is used to prepare the samples for precision e-beam writes. Since the SiN membrane are hydrophobic it is necessary to plasma treat them before depositing the resist. The initial under layer of MMA is chosen to give an undercut to the write process. The MMA is deposited on the substrate as it spins at 4500 *rpm* for 45 seconds and is subsequently baked for 10 minutes at 150 ^{o}C. Once

the MMA hardens a layer of PMMA, with a molecular weight of 950,000, is deposited on the membrane while spinning at 6000 *rpm* for 45 seconds which is again baked for 10 *min* at 180 ^{o}C to harden the resist. The slower spin speed of the MMA is to ensure that the resist will be thick enough for successful liftoff in the later steps. After preparing the resist a layer of conductive polymer, aquaSAVE [71], is spin casted on top. The aquaSAVE coats the resists and avoids problems due to charging and other electro static problems during the e-beam write process.

To attain the highest resolution, it is necessary to focus the e-beam as well as possible. For that, the finest features are written at the smallest aperture with the lowest current with the highest possible accelerating voltage. To ensure optimal focus a contamination spot size is burned into the resist by exposing it to the electron beam for 120 seconds. Focusing on the spot provides an optimum condition for the write process and additionally will show evidence of any possible stigmation.

After finishing the e-beam write the samples are developed by first removing the top layer of aquaSAVE using deionized (DI) water. After removing the aquaSave the membranes are blown dry using nitrogen. The PMMA and MMA are developed for 50-60 seconds in a 1:3 solution of methyl isobutyl ketone: isopropyl alcohol (MIBK:IPA). The samples are quickly sprayed by IPA to neutralize the MIBK and avoid overexposure of the pattern.

4.3.2: Metal Deposition

After developing the samples, high purity metal is deposited on the membrane. Thermal evaporation is used for depositing gold (Au) and chromium (Cr)

and an e-beam evaporator is used for palladium (Pd). The deposition thickness and rate are monitored using a crystal monitor. In both cases the chamber is pumped down to below $2x10^{-6}$ *Torr* to ensure clean metal evaporation. Furthermore, the samples and the source are kept under vacuum for 10 minutes after metal deposition to avoid damage due to rapid cooling.

4.3.3: Lift-off

After metal deposition the samples are placed in acetone for 45-60 min to remove the resist from the top of the membrane. As the resist dissolves, and is removed from the substrate, it also removes the metal deposited on top of it, consequently only leaving metal in the parts exposed by the electron beam during lithography. To ensure successful liftoff process the samples are sprayed by acetone as they are taken out. Finally, the samples are sprayed by IPA and dried using nitrogen gas to remove the acetone. It is important to note that the samples should be checked carefully for successful liftoff before removing them from acetone as it becomes extremely difficult to remove the metal from the substrate once the acetone has dried.

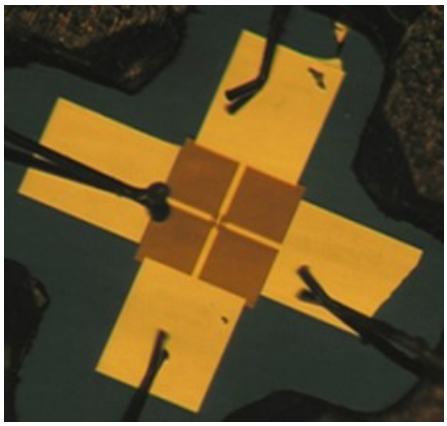

Figure 4.8: Image of a device inside the 4 probe TEM holder, showing Cr/Au contact pads.

4.3.4: CNT Deposition

Heat dissipation properties of individual MWCNTs were studied by incorporating them in devices and heating them either passively or actively. As described earlier, CNTs have many unique thermal characteristics due to their well-ordered crystalline structure. As such their properties greatly change due to defects and it is important to use high quality MWCNTs when studied for their fundamental thermal properties. We use commercially available arc-discharge grown MWCNTs purchased from Aldrich in fabricating our devices [72]. These CNTs are of much higher quality compared to CVD grown nanotubes. The supplied nanotubes are surrounded by a fused carbon shell ~1 *cm* diameter, which must be broken to gain access to the MWCNT core. After breaking the shell, the nanotubes are gently scraped off for later use by a steel razor blade.

Since the work aims to study the thermal transport of individual nanotubes the bundles need to be separated. First, the scraped off bundles are mechanically grinded to powder form. The powder is then dispersed in IPA and bath sonicated for 15 minutes. To reduce graphitic contaminants from interfering with the device, the nanotube-IPA solution is further sonicated using a probe sonicator at 20% power and centrifuged, after which the nanotubes separate and float above the heavier graphitic material. Finally, using a pipet, the nanotube is spin casted on the SiN membranes as they spin at 5000 *rpm*.

The nanotube selected for device fabrication are chosen based on their high quality and their relative position to the electric contacts and graphitic contaminants on the substrate. As such, a careful characterization of the CNT is necessary before

making electrical contacts. To reduce beam damage, the imaging is done by TEM at 100kV, the nanotube position relative to the markers on the SiN is measured and is used to make electrical contacts or heater wires in the later steps. To ensure low electric contact resistance between the electrodes and the CNTs, the devices are plasma etched using O_2 at 8 *watts* and 150 *mTorr* for 60 seconds using a March Jupiter III O_2 plasma system.

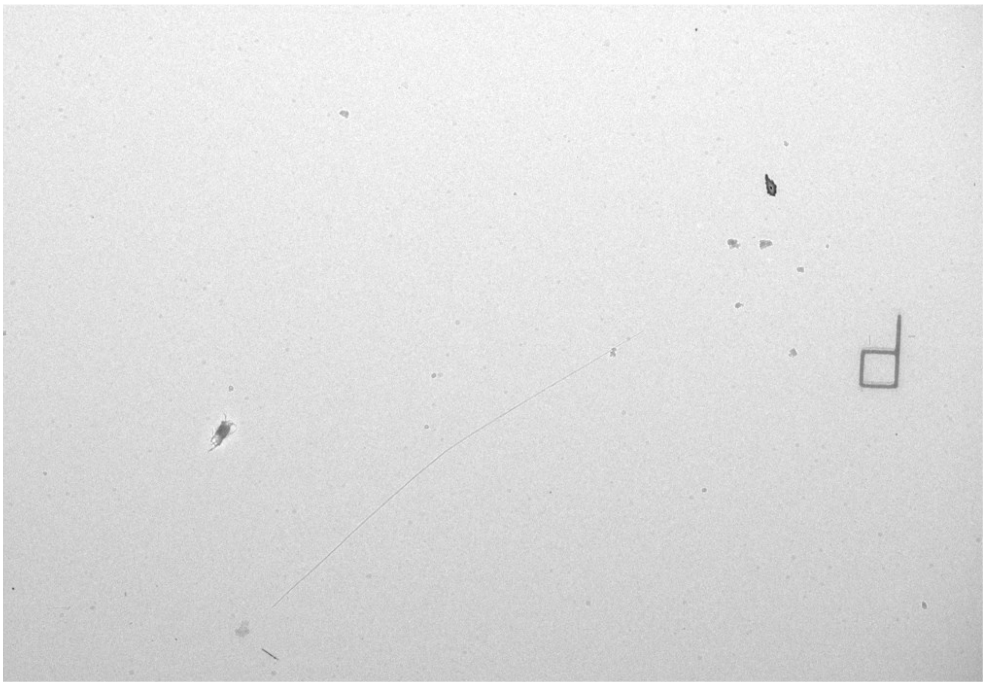

Figure 4.9: TEM image of a MWCNT spin casted on a SiN membrane with its position indicated relative to an alignment marker.

4.3.5: Indium Deposition

The final step of device fabrication is the deposition of Indium islands on the back side of the substrate using thermal evaporation. The sample is carefully placed upside down on a deposition holder and placed inside the chamber and pumped to pressures below 10^{-7} *Torr*. As mentioned before, the In islands are surrounded by an oxide layer and the low pressure is required to minimize the oxidization of the metal.

Additionally, the size of the islands is also of importance for high quality thermal imaging. If the islands are too large then the thermal imaging will have low resolution, but if the islands are too small then it will be difficult to monitor the phase change of all islands at the same beam tilt. The easiest way to control the size of the islands, is by monitoring the deposition rate, and it has been observed that depositing between 3-8 *Å/sec* will yield the best island geometry. After depositing the islands it is important to keep the samples in vacuum for 10-15 *min* to allow the sample to cool, to avoid creating excess oxide layers on the In.

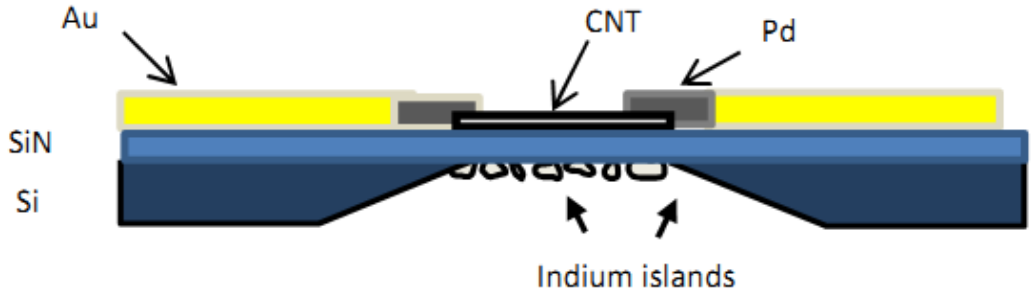

Figure 4.10: Final schematic of a device with the electrodes and the nanotube on the top of the SiN membrane and the In islands deposited on the bottom.

4.3.6 Biasing

By connecting the electrical holder to an external power supply it is possible to bias the samples and conduct in situ electrical measurements. A LabVIEW program is used to collect the data with capabilities to remotely communicate with the TEM software and take pictures with specific exposure times. Depending on the resistance of the devices, a great deal of caution must be taken to avoid damage due to electrostatic charges. Grounding the goniometer is one such precaution, the TEM goniometer operates at a 4 *V* potential relative to the ground and consequently

contacting the holder with the goniometer during loading and unloading can damage the samples. A simple potentiometer circuit is built to ground the goniometer during loading and unloading to avoid exploding the sample.

4.4: Analysis

4.4.1: Image Processing

To process the data using our thermal imaging technique, TEM images are taken in the dark field condition at each voltage increment as the islands begin to melt. By assigning a color to each melting voltage it is possible to create a composite voltage map of the device which shows the change in substrate temperature as a function of voltage. The visual representation gives a quantitative representation of heat transport and further simulations are used to gain better qualitative understanding. This processing is carried out with MATLAB aided by the Image processing Toolbox.

4.4.2: Modeling

The experimental results obtained from the thermal microscopy studies provide a quantitative understanding of heat transport. However, to gain a better comprehension, the experimental results are further investigated using a finite elemental analysis software (COMSOL) which allows us to simultaneously study the electrical and thermal behavior of the devices.

The model geometry is drawn using a CAD software based on measurements from the TEM images taken during the experiment. The electrostatic physics is modeled using the steady-state current continuity equation

$$-\nabla \cdot \left(\frac{1}{\rho}\nabla V\right) = 0 \tag{4.1}$$

Where ρ is the resistivity of the material and is represented by

$$\rho = \rho_0\big(1 + \alpha(T - T_0)\big) \tag{4.2}$$

The model uses the temperature coefficient of resistivity, α, to incorporate the change in resistivity of the material as a function of temperature. Here, ρ_0 is the resistivity at the reference temperature T_0. Considering the supporting 200 μm SiO_2 layer as a thermal heat sink the thermal boundary condition is set at the ambient temperature of $T_0 = 293\ K$ and the rest of the model thermally insulated.

The heat transfer physics is modeled using the steady state heat diffusion equation with the boundary condition of $T = T_0$ at the edge of the substrate.

$$\frac{1}{\rho}|\nabla V|^2 = -\nabla \cdot (k\nabla T) \tag{4.3}$$

Where k is the material thermal conductivity, and the left side of the equation is the heat source do to the applied potential. For metals the thermal conductivity is expressed by the Wiedemann-Franz law as

$$k = \frac{1}{\rho}LT \tag{4.4}$$

where L is the Lorenz number and is expressed as $L = \frac{\pi^2}{3}\left(\frac{k_e}{e}\right)^2 = 2.44 \times 10^{-8}\ W\Omega K^{-2}$ [73].

The model solves the current continuity and heat equation for voltage (V) and temperature (T) respectively. Simulations are carefully chosen to produce qualitative

understanding of the physical parameters of the devices studied. In each model certain variables are left as free parameters and their value extracted by matching the simulated results to the experimental *I-V* data and thermal profile of the molten islands. A more detailed description of modeling is given, as needed, in the following chapters.

Chapter 5: Heat dissipation in current carrying nanotubes

The previous work concerning Joule heated carbon nanotube on SiN membranes demonstrated their surprising characteristic which allows them to stay cold [2]. As discussed, despite the flow of electrons within the CNT, its temperature does not increase and instead the energy from the hot electrons appears to contribute to increasing the temperature of the supporting membrane directly.

Taking advantage of the electrical properties of the MWCNTs and their high thermal conductivity we aim to devise an experiment to provide definitive proof for the prominence of a remote Joule heating phenomena in current carrying carbon nanotubes. As such, the goal was to formulate an experiment in which the heating of the substrate via hot electrons could be switched on or off depending on the current path of the nanotube system.

5.1: Measurements and Results

Consequently, a cross nanotube geometry device was designed, such that two MWCNTs are perpendicularly positioned on top of each other, schematic of such a crossed geometry can be seen in figure 5.1. Three Pd pads are fabricated to allow three possible current paths. As demonstrated, it is possible to pass current through the device, employing two of the electrodes and floating the third, in three different configurations, demonstrated in figure 5.2. The current paths are color-coded, black, red, and blue for straight, short cross, and long cross path respectively. Additionally, prior to depositing the metal, the nanotubes are gently plasma etched to reduce the electrical contact resistance in the circuit.

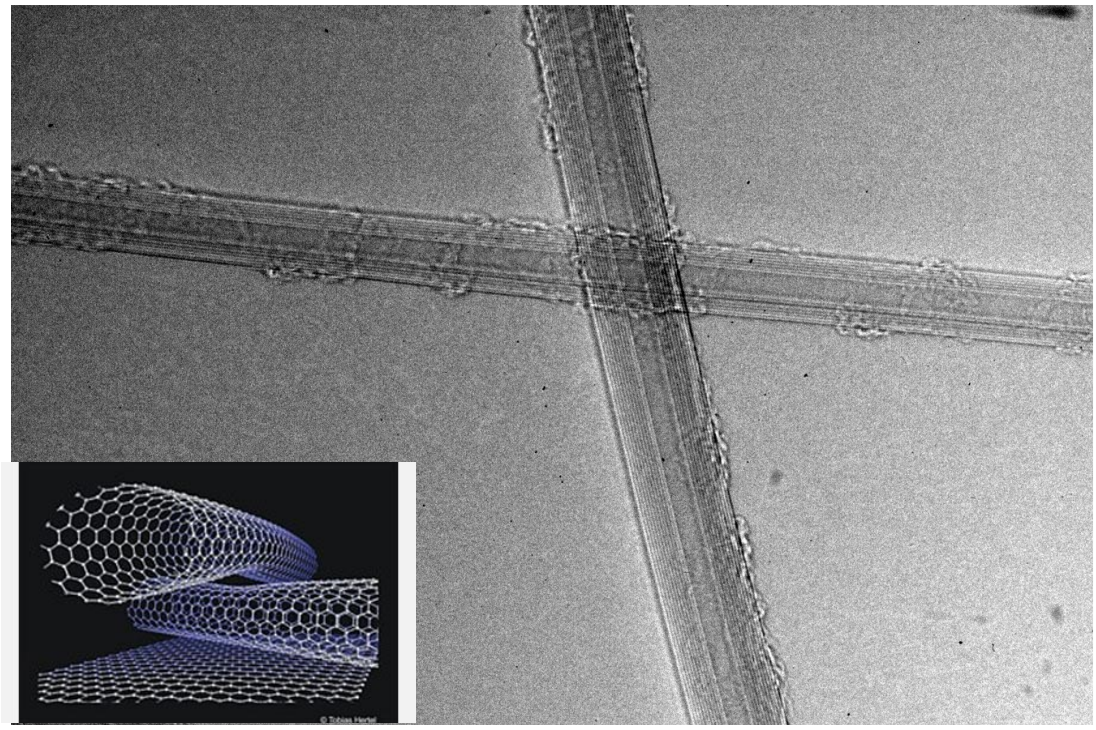

Figure 5.1: TEM image of a two crossing MWCNTs, clearly showing each individual wall. The inset shows the 3D structure of such a crossed CNT setup [74].

As shown in figure 5.2a, the vertical nanotube was connected to electrodes A and C while the horizontally positioned nanotube was connected to electrode B. The length and diameter of the two nanotubes are attained using TEM images, the vertical nanotube was measured to be 30 *nm* in diameter and the horizontal nanotube was measured to be 26 *nm*. The length of the vertical nanotube, measured from the edge of electrode A to C is 3.18 μm while the length of the horizontal nanotube from the edge of electrode B to its free end is 1.19 μm. The device configuration is such that the distance from each electrode to the nanotube junction varied from 1.1 μm, 620 μm, to 2.05 μm. Electrical biasing is carried out using a Keithley 236 power supply.

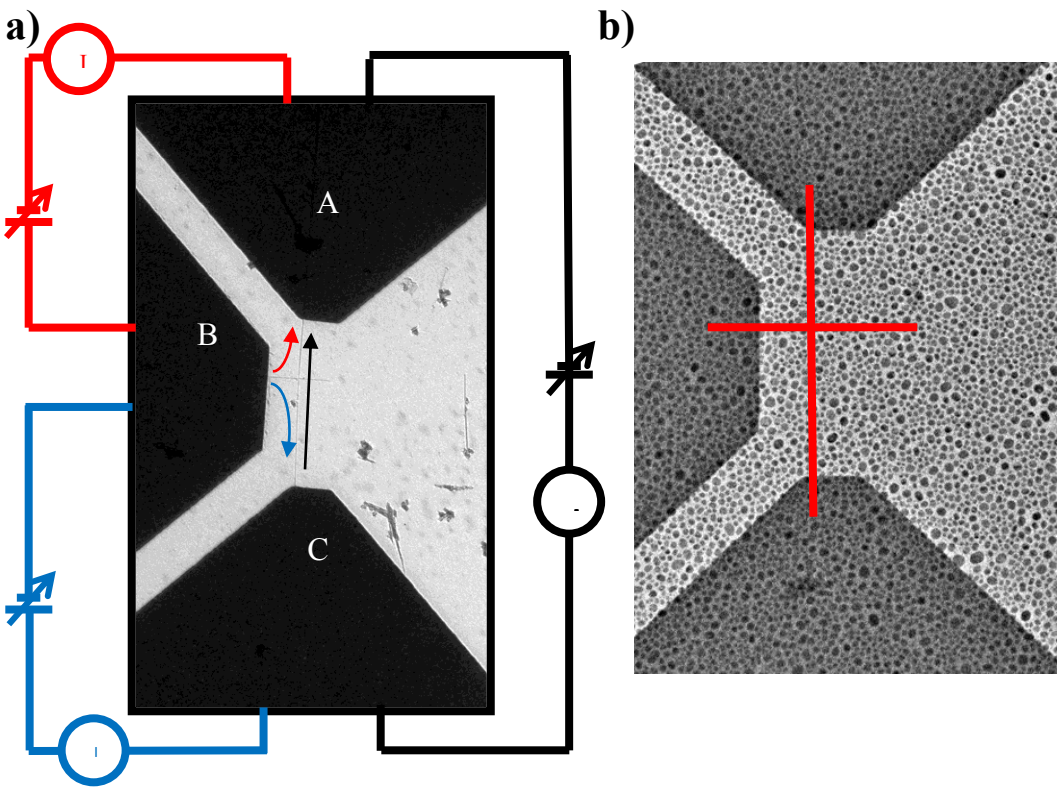

Figure 5.2: (a) TEM image of the cross nanotube device with the 3 possible current paths. (b) BF image of the device after deposition of In on the back of the membrane, red line indicates the position of the CNT.

Based on the described schematics, a *DC* potential gradient is applied across electrodes A and C, straight path, biasing the vertical nanotube. From the *I-V* readings of the power supply the resistance of circuit was monitored as the voltage is ramped to 2.26 *V*. The device is initially slowly ramped to stabilize after the initial current-induced annealing of the contact pads. Imaging the nanotube in dark-field conditions, the first islands are observed to melt at 1.93 *V*, at 105 *nm* below the junction, figure 5.3a. The resistance is calculated to be 71.48 *kΩ* at the initial melting voltage. As the potential is further ramped up more and more islands began to melt until the

maximum voltage of 2.26 *V* where most of the islands along the length of the nanotube have undergone a phase change, figure 5.3b.

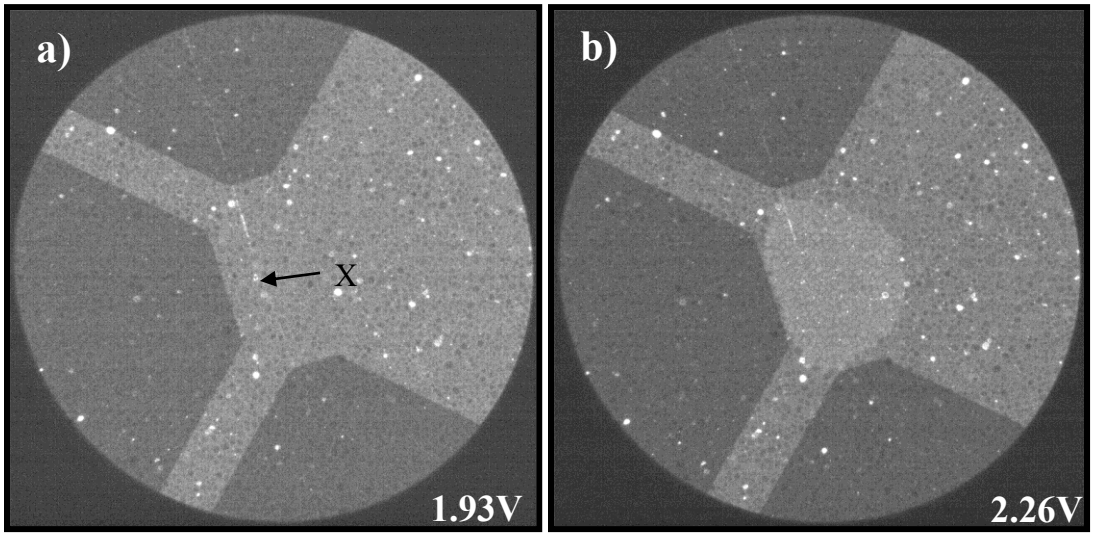

Figure 5.3: DF image of the device with potential applied across electrode A-C at (a) 1.93V, showing initial melting (marked by X), and at (b) 2.26V.

By assigning a unique color to the In islands that melt at a given voltage a color map of the melting profile is created, figure 5.4, which qualitatively demonstrates the temperature gradient across the substrate. The temperature profile indicates the hottest area to be at the region close to the center of the nanotube with slight asymmetry, perpendicular to the nanotube, due to heat sinking from electrode B.

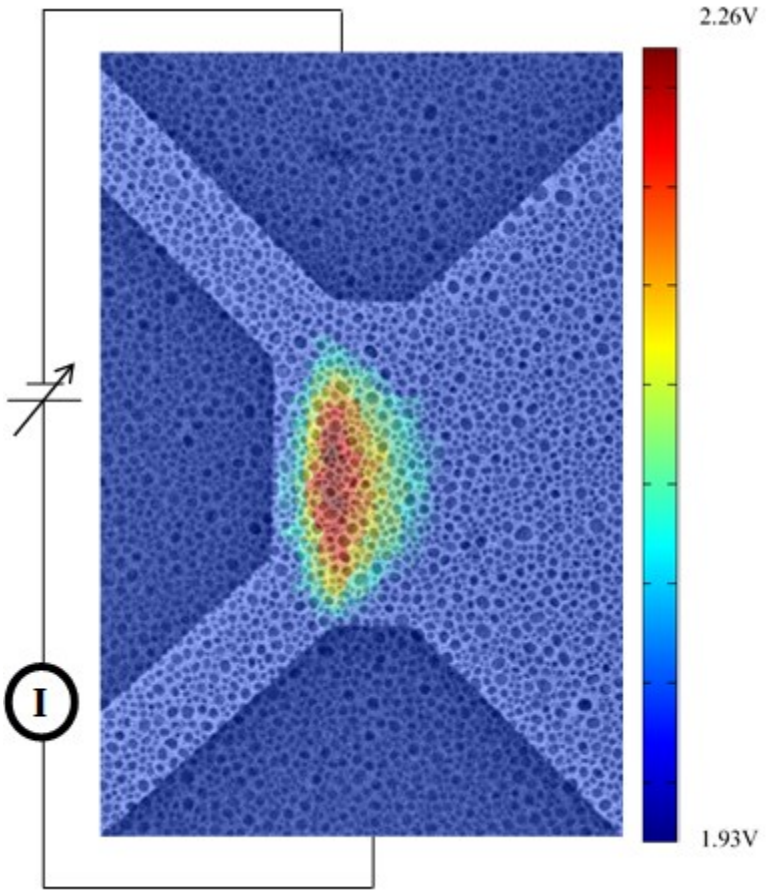

Figure 5.4: Thermal map of A-C biased device. The colors correspond to the voltages needed to melt each island.

By changing the circuitry, the procedure is repeated by applying a potential difference across the two nanotubes, through the junction, first through A – B (short cross) and then through B – C (long cross), (figure 5.5). Similar to before, the electrical and thermal measurements are collected for the two configurations. Applying a potential across B – C the islands are initially observed to melt at 1.825 V, and the resistance is calculated to be 67.59 $k\Omega$. The melting position of the initial islands is measured, from the dark-field images, to be 229 nm below the junction. The DC voltage is slowly ramped in 5mV increments until the maximum voltage of 2.33V

where the melting front reaches the vicinity of the large Pd electrical pads, figure 5.6a.

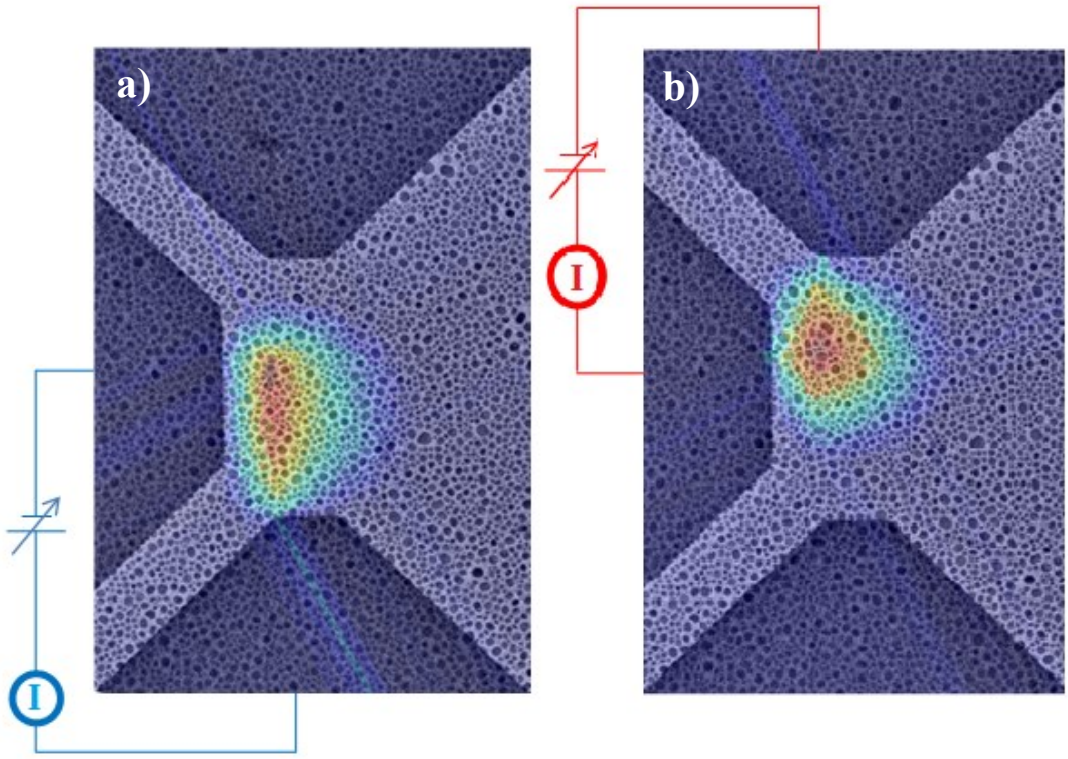

Figure 5.5: Thermal map of (a) B-C biased device and (b) A-B biased device. Both images clearly indicate heating under the current carrying region of the nanotube.

Lastly, the potential difference is applied to electrodes A and B. In this setup, the melting occurs at 1.295 *V*, 105 *nm* above the CNT junction and the resistance at the initial melting voltage is calculated to be 38.09 *kΩ*. The voltage is increased to 1.69 *V* until the melting profile expands, once again reaching the Pd pads, figure 5.6b.

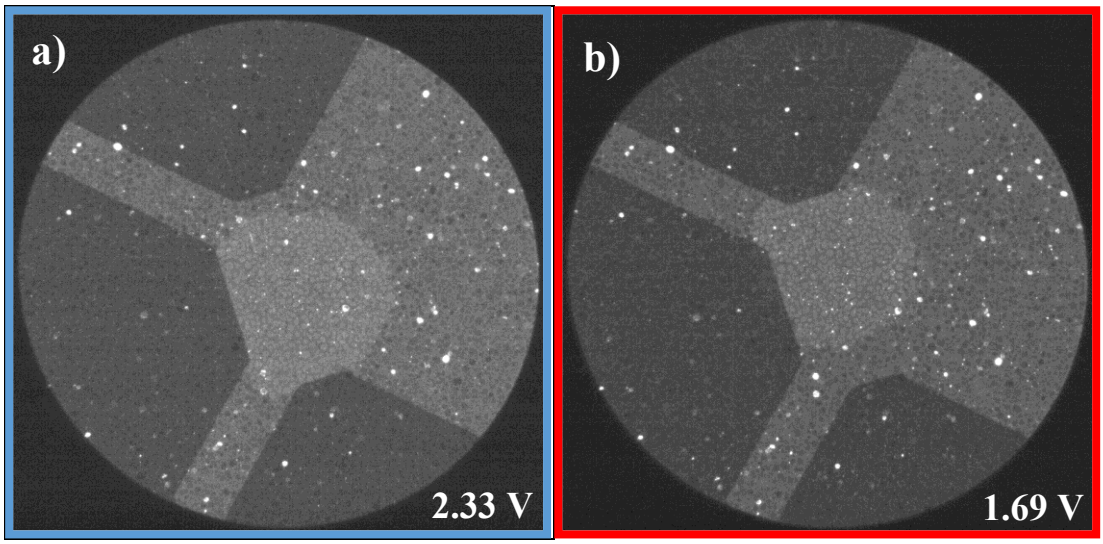

Figure 5.6: DF images taken at the maximum voltage for the (a) B-C and (b) A-B current paths respectively

From the TEM images, the total nanotube length for A-C, B-C, and A-B is measured to be 3.186 μm, 2.702 μm, and 1.796 μm respectively. From the resistance values the relative resistivity is calculated to be 22.4 $k\Omega/\mu m$, 25.01 $k\Omega/\mu m$, and 21.21 $k\Omega/\mu m$. The discrepancy in the resistivity values is attributed to non-uniformity of the nanotube, apparent from contrast variation along its length as seen in figure 5.7.

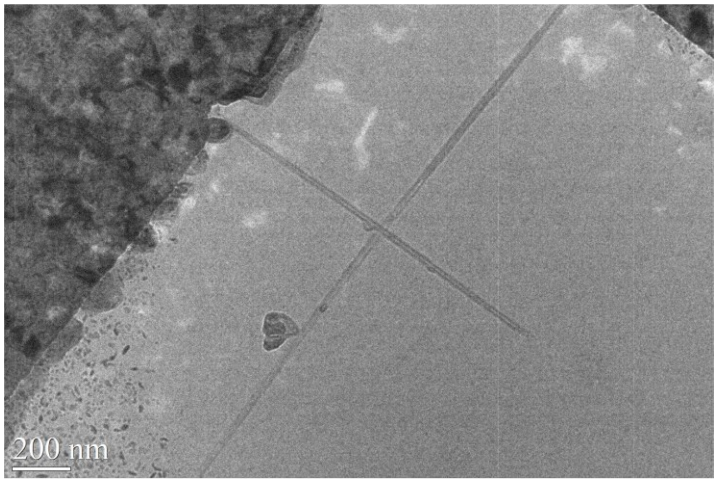

Figure 5.7: TEM image of the nanotube. The difference in contrast along the length may be correlated to the variation in the resistance.

Additionally, unlike the straight path, the measured resistance value for short path and long path includes the CNT-CNT junction resistance. Although the exact junction resistance can not be calculated, due to variation along the length of the nanotube, the small variation in the calculated resistivity values suggests that it is relatively small.

Current path	Path length	Resistance V/I
A-C (straight)	3.186 µm	71.48 kΩ (22.4 kΩ/µm)
B-C (long cross)	2.702 µm	67.59 kΩ (25.01 kΩ/µm)
A – B (short cross)	1.796 µm	38.09 kΩ (21.21 kΩ/µm)

Table 5.1: Length and resistance of the three current paths.

5.1.1: I-V Characterization

In a study of Joule heating characteristics of a material it is of utmost important to have a good understanding of its current carrying ability. Consequently, the *I-V* behavior of the nanotube devices should be well studied. For all three cases, the current is increasing and the *I-V* has a positive curvature which in turns indicates a decreasing resistance (see figure 5.11). Since MWCNTs can be considered to be composed of several nested SWCNTs it is reasonable to compare their electrical properties with SWCNTs, as a simpler model. Most notable features of the I-V curve of SWCNTs are their negative curvature and current saturation at high voltages (see figure 5.8).

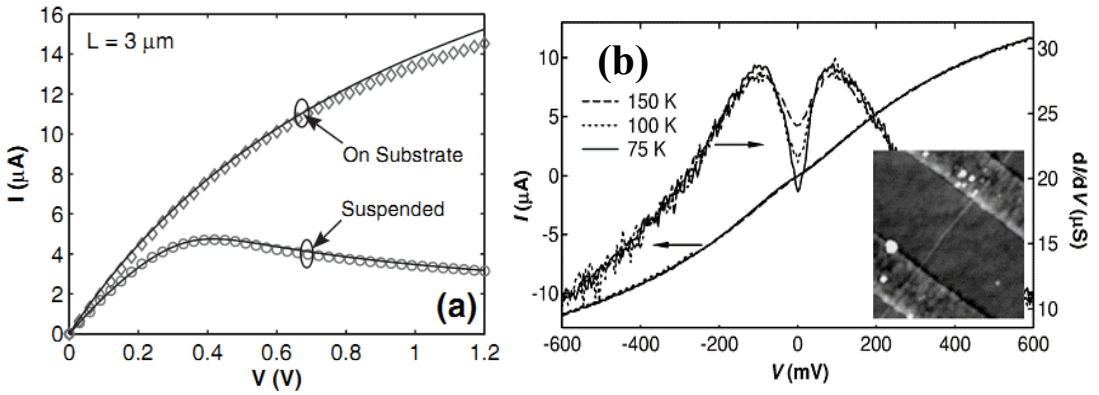

Figure 5.8: (a) Experimental I-V curve demonstrating the saturation of the current for a SWCNT. The theoretical model without joule heating predicts the curve at low voltages [75]. (b) I-V curve for a SWCNT with its corresponding conductance, which decreases for increasing voltage [44].

SWNT

The current saturation of on substrate SWNTs has been well documented [44] and studied by a number of groups. Due to heat sinking of the supporting substrate, the models used to explain the behavior assume an isothermal condition [6,44,45]. In these models the non-ohmic behavior is attributed to the change in the total scattering mean free path, $\lambda_{total}(V)$, as a function of applied bias [76]. At low biases the electrons scatter from the low-energy long wavelength acoustic modes of the lattice [77]. The weak scattering mechanism results in a correspondingly large mean free path and thus a ballistic transport mechanism. However, as the energy of the electrons is further increased, at the high bias regime, the electrons emit optical phonons and are immediately backscattered which result in current saturation [75, 76], as seen in figure 5.8. Consequently the $\lambda_{total}(V)$ depends on the combined acoustic phonon scattering mean free path, λ_{ac}, and the optical phonon emission mean free path, λ_{op}, by the relation

$$\lambda_{total} = \left(\frac{1}{\lambda_{ac}} + \frac{1}{\lambda_{op}}\right)^{-1}. \quad (5.1)$$

In theory, there are additional available states for optical phonon emission at higher energy levels and as such the λ_{op} is dependent on the accelerating field of the electrons, and is dependent on the applied voltage, V, by

$$\lambda_{op}(V) = \frac{\hbar\omega_{op}L}{eV} + \lambda_{op,min} \quad (5.2)$$

Where L is the length of the nanotube. Using the model the I-V behavior of on substrate SWNTs can be accurately predicted, plotted as a solid line in figure 5.8a, which shows ohmic behavior at low bias and current saturation at high biases. Even though the theory predicts the correct trend, its predicted value begins to diverge at elevated voltages, as it overestimates the current, which indicates the onset of self-heating as the nanotube can no longer be treated as an isotherm and the model must incorporate Joule heating.

The electron-phonon scattering at the high bias regime results in a decrease in differential conductance, dI/dV, measurements, (see figure 5.8b). However, below 100mV dI/dV increases with increasing voltage. This positive slope is sometimes extended to much higher bias ranges by increased contact resistance of the device. The phenomena is attributed to suppressed tunneling density of states due to finite contact resistance.

MWCNT

By treating MWCNTs as a series of concentric SWCNTs it is reasonable to expect that their electrical properties will depend on the properties of each individual constituting SWCNT as well as their interaction with each other. Therefore, the mean

free path, λ_{total}, the number of current-carrying shells, N_{shell}, and the number of available conducting modes must be evaluated, N_{mode} [79]. The current measured across the nanotube depends on the energy level gap between the top of the valence subband and the bottom of the conduction subband as electrons tunnel across. At elevated biases, more conducting modes become available as the electric field reduces the tunneling barrier and thus results in an increasing differential conductance. In addition, the number of current-carrying shells is also believed to increase at higher potentials. By removing individual carbon shells of MWCNTs, it has been shown that at low bias only the first few shells contribute to conduction [56, 80, 81]. However, at high biases additional shells begin to contribute to conduction, which in turn results in an additional increase in differential conductance. Consequently, MWCNTs have a much wider bias range for which they exhibit a positive differential conductance. Nevertheless, at sufficiently high voltages, after all available conducting modes and carbon shells have become engaged, the electron-phonon scattering starts to dominate and results in saturating the current.

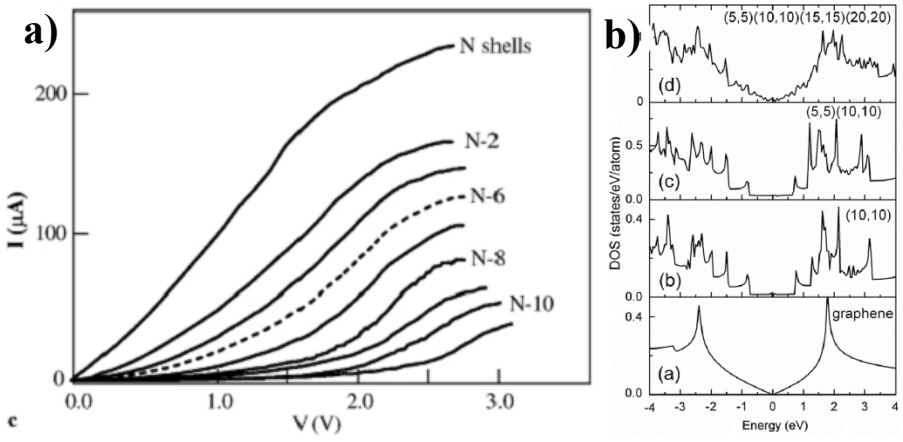

Figure 5.9: (a) Experimental I-V curve from MWCNTs by removing each individual wall [81]. (b)Comparison of graphene, SWCNT, and MWCNT DOS [82].

For our devices the Indium islands undergo their phase change before the high bias regime, where the current begins to saturate, and thus the I-V data exhibits a positive curvature in the range of interest (see figure 5.11). In the SWCNT model the low bias regime, before current saturation, was accurately modeled without invoking a Joule heating model purely based on the variation in the electron mean free path [75]. Thus, it is possible to quantify the start of resistive heating from electrical measurements. The fact that we do not observe indications of current saturation implies that the nanotubes are not heating during our measurements which is consistent with prior reported results [2].

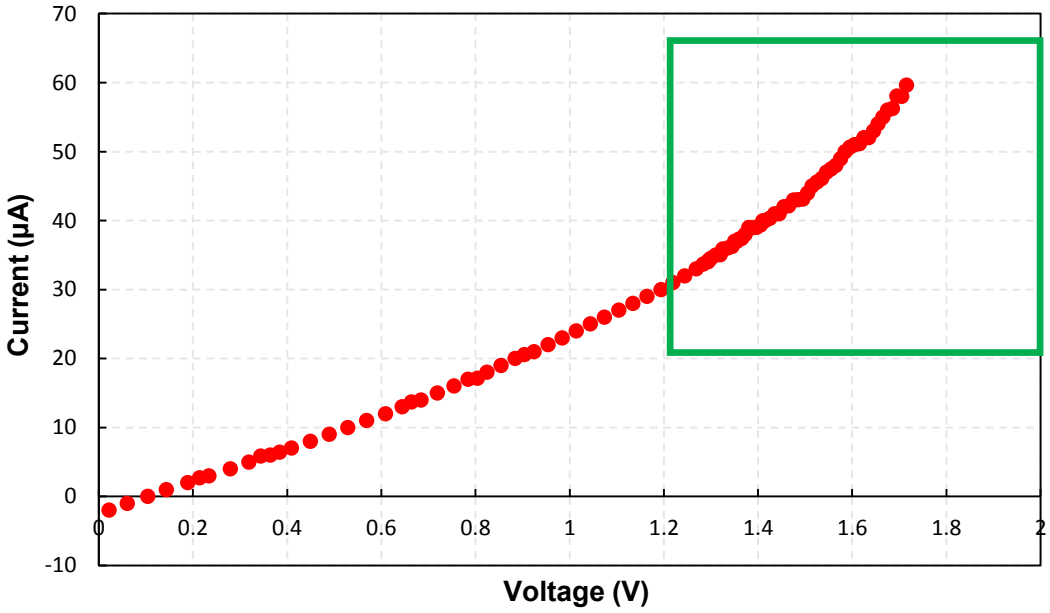

Figure 5.10: Experimental I-V curve for the crossed nanotube device, with voltage applied between electrodes A and B.

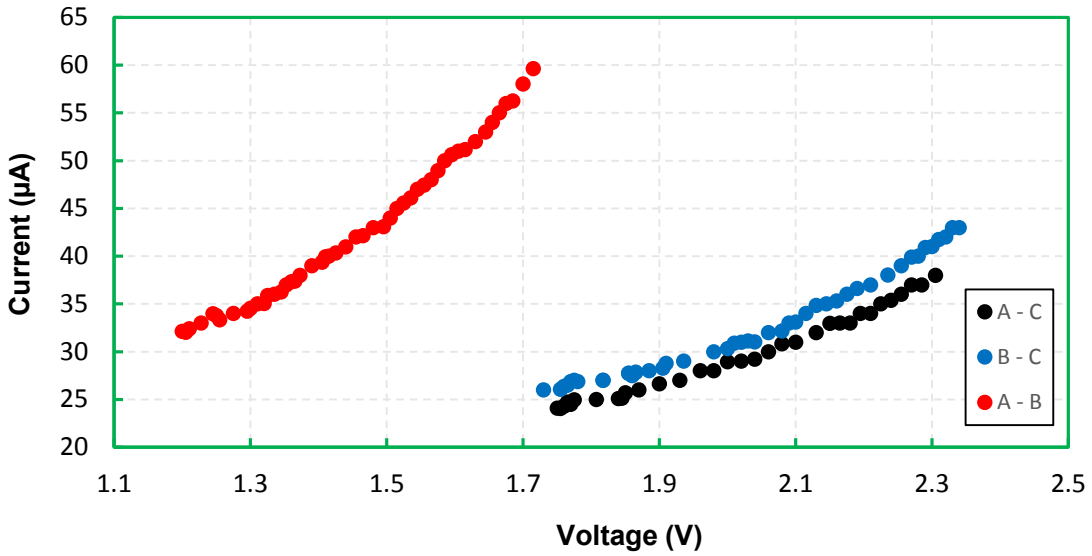

Figure 5.11: Experimental I-V curve for the crossed nanotube device for the three current paths.

5.2: Analysis and Discussion

In evaluating the temperature gradient across the substrate one must have an understanding of the heat source and the mechanism by which the heat is dissipated from it. Here the heat source is characterized by the power, P = IV, and thermal conductivity of the lattice, k_{cnt}. In addition, the thermal contact resistance of the CNT with the substrate and the Pd contacts will dictate how heat will be transferred from the nanotube to the substrate.

The thermal conductivity of MWCNTs has been measured by a number of techniques, described in detail in Chapter 3, and is believed to be between 1000-3000 *W/m.K [83]*. It has a maximum at 320 *K* and decreases at elevated temperature due to Umkalpp scattering. The thermal contact resistance of the nanotube with the SiN have been studied [1] and reported in previous work exhibiting high thermal contact resistance between the SiN membrane and the carbon nanotube, ${}^{SiN}R_c = 250\ m.K/W$,

relative to the low thermal contact resistance of Pd and the nanotubes, ${}^{Pd}R_c = 4.2$ *m.K/W*. Consequently, one would expect that the region of the membrane under the Pd contacts will be the hottest, thus the In islands in this area will melt at lower voltages. However, as evident by the experimental voltage maps for the straight current path, the center of the nanotube heats first (see figure 5.4). The effective heat transfer between the nanotube and the substrate seems to suggest that the thermal contact resistance between the SiN and the nanotube is much smaller than expected.

A different picture emerges however, from the results for the current paths through the nanotube junction (red and blue in figure 5.2). Based on the reported high thermal conductivities of carbon nanotubes, one would expect that upon biasing a section of the nanotube system, the entirety of the nanotube system will heat up due to its inability to support large temperature gradients. However, it was observed that the current carrying region of the nanotube system gets considerably hotter than the unbiased region, as seen in figure 5.5. The observed behavior suggest a more efficient heat dissipation mechanism that is dominant at the current carrying region.

5.2.1 Remote Joule Heating

Preliminary simulations were made using a finite element modeling tool, COMSOL, to study the melting profile of the straight nanotube (black current path). To model Joule heating in our devices we had previously solved

$$\nabla \cdot (\kappa \nabla T) + P - \frac{\Delta T}{R_c} = 0 \tag{5.3}$$

but it became immediately apparent that such solutions produce initial heating of the contacts (see figure 5.12).

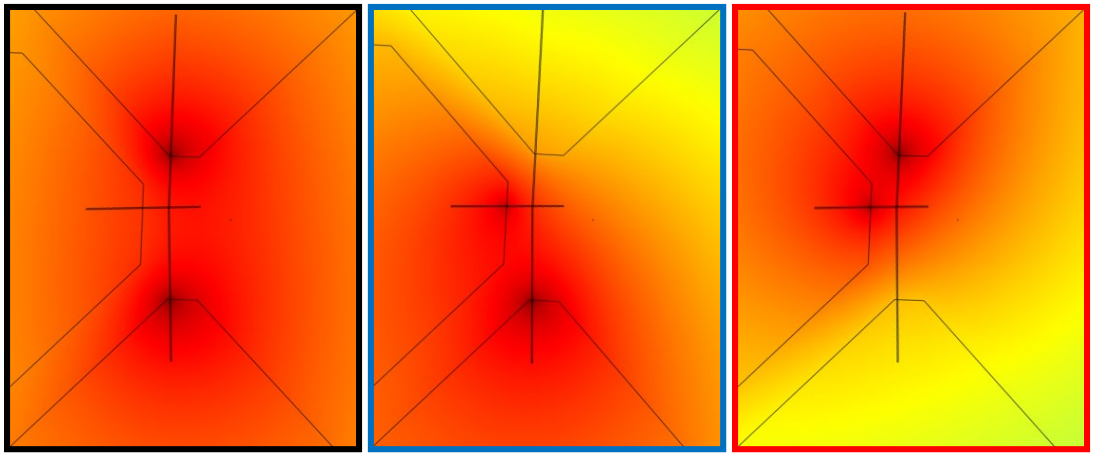

Figure 5.12: Simulated results using a standard joule heating model.

Consequently to match the melting profile, as seen in figure 5.13, we invoke a "remote-heating' parameter, β, which is the fraction of the applied power that is dissipated into the substrate. With the new model the equation can be written as,

$$\nabla \cdot (\kappa \nabla T) + \beta * P + \frac{\Delta T}{R_c} = 0, \tag{5.4}$$

where $\beta = 1$ indicates a 100% power dissipation to the substrate and $\beta = 0$ indicates a standard joule heating model. Simulating the model at the initial melting voltage suggests that at least 86% of the heat in the nanotube must be transmitted directly to the substrate. The value of β is extracted from the simulations by setting it as a free parameter and varying it until the simulated melting profile matches the experimental melting profile at $1.93V$.

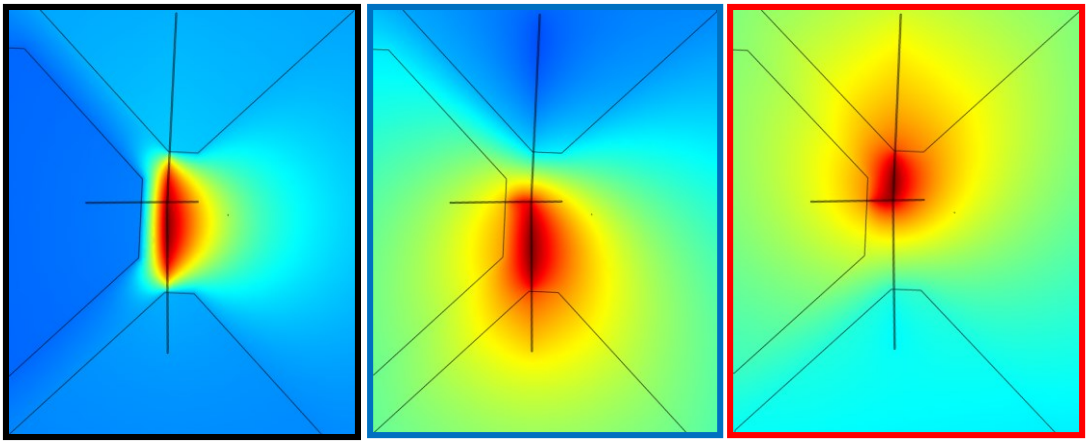

Figure 5.13: Simulated results using a remote heating model where the heat is generated in the SiN, instead of the nanotube.

Even though we can not quantify the exact nature of the energy exchange mechanism from our results we have demonstrated that it depends on the flow of the hot electrons through the nanotube. A possible explanation for the coupling of the electrons with the substrate has been proposed by Slava Rotkin [46]. In the theoretical model, the energetic electrons couple to the surface phonon polaritons, which increase the temperature of the substrate. This process depends on the energy state of the electrons, due to the bias voltage, as they must have sufficient energy to interact with the SPP of the membrane. Consequently, the electrons must be accelerated above a certain threshold potential for remote Joule heating to occur.

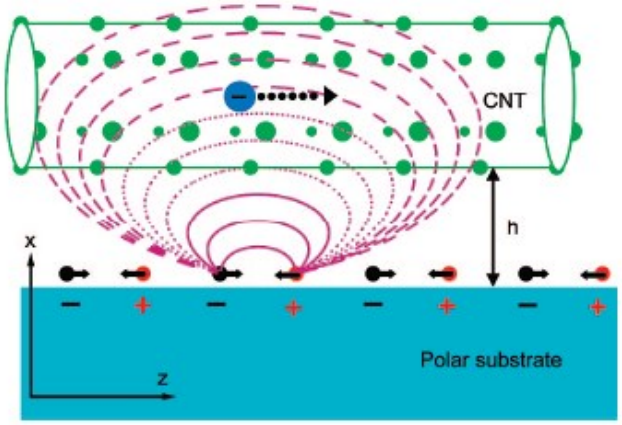

Figure 5.14: Schematic demonstrating the coupling of the hot electrons with the EM field generated by a polar substrate.

5.2.2: Voltage Dependence of Remote Joule Heating

To monitor the dependence of the remote Joule heating on the accelerating voltage, the data at initial melting was compared to elevated biases. From the experimental *I-V* data it is clear that the conductance of the nanotube increases monotonically which suggest an increased population of energetic electrons for higher voltages. Consequently, one would expect the remote Joule heating effect to become enhanced as the voltage is increased. However, from simulating the results at the highest measured voltage, 2.26 *V*, we extracted $\beta = 0.39$, indicating a reduction in remote joule heating for increasing voltage.

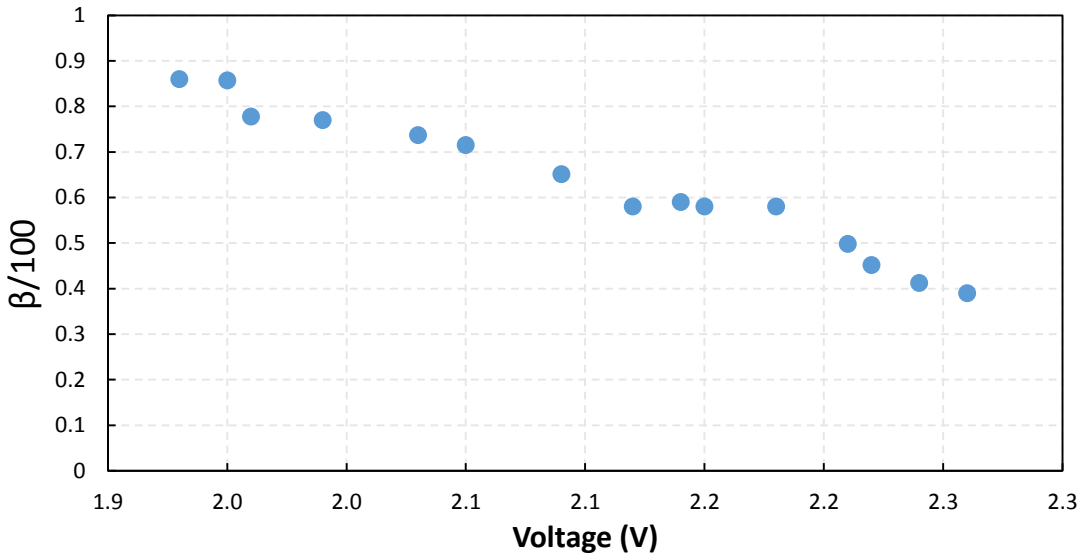

Figure 5.15: Variation in β as a function of applied voltage extracted from the simulations.

Without a concrete physical model to understand the heat transport mechanism it is difficult to assess the meaning of a reduction in remote joule heating. However, since the model directly depends on the thermal conductivity of the substrate a series of control experiments were designed to study if the k_{SiN} varies as a function of voltage. Unfortunately, as we show in the next chapter, the voltage-dependence of k_{SiN} still shows variations that we are unable to accommodate within a physical model. For this reason, it is still unknown if the voltage-dependence of β is intrinsic, due to CNT transport, or extrinsic, due, for example, the temperature-dependent substrate effects.

Chapter 6: Thermal conductivity of SiN (k_{SiN})

The primary thermal imaging technique used in this dissertation detects the phase change of Indium from solid to liquid, at 429 *K*. The temperature of the system under study is dictated by two factors; the heat source and the efficiency of the heat transfer mechanism to the lower temperature reservoir, always at room temperature, 293 *K*. All the measured devices discussed rely on Joule heating of either a Pd heater wire or MWCNTs as heat source. The efficiency of the heat transfer mechanism is quantified by the thermal conductivity of the different materials constituting the device and their thermal contact resistances. From observing the melting profile of the In islands in a Pd heater wire system, it is possible to attain a quantitative understanding of the thermal properties of the SiN membrane to use in more complicated system involving CNTs. Our basic starting assumption is that, unlike Joule heating in CNTs, Pd heater wires should not require a new thermal models to explain their heat dissipation mechanism and thus serve as excellent platform for control experiments. As we show below, this basic assumption may not always prove to be sufficiently valid.

6.1: Device Characterization

The Pd heater wire devices are fabricated using e-beam lithography on electron transparent SiN membranes with varying thicknesses. After lithography, the metals used in fabricating the heater wire and the electric contacts are deposited using a combination of thermal evaporation and e-beam evaporation techniques. As a final step, indium is deposited on the back side of the membrane using thermal

evaporation. The parameters, tools, and the techniques used in fabricating the devices can be found in more details in chapter 4.

Examples of few different types of Pd heater wire devices are shown in figure 6.1. Using the 4-probe electric holder, and depending on the geometry, it is possible to fabricate up to three separate heater wire devices on a given membrane, as seen in figure 6.1b. The lengths of the heater wires studied have ranged from 0.865 μm – 4.0 μm. The larger contact pads supplying the power to the heater wire are designed to be wider such that the heat is generated only primarily in the nanowires.

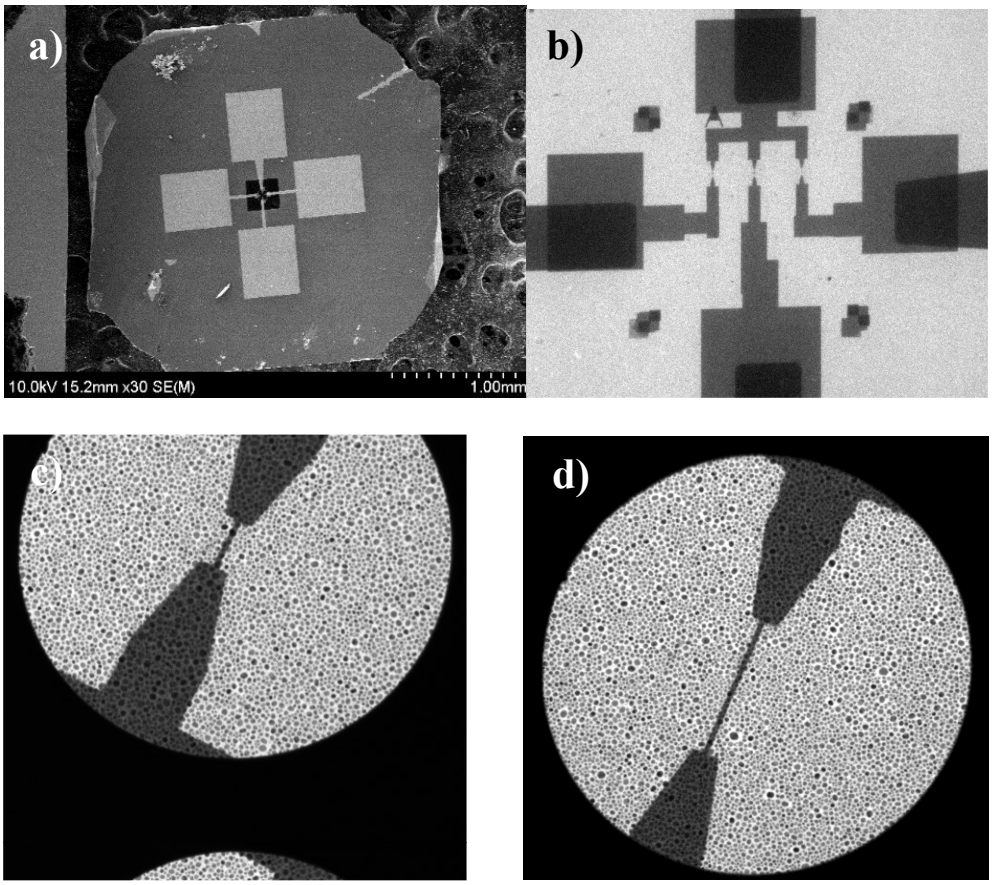

Figure 6.1: (a) SEM image of typical membrane with the 4 large electrical contact pads. (b) A 3 heater wire device, all sharing the same ground electrode. The length of the heater wire range from (c) ~0.85 μm to (d) ~2.5 μm.

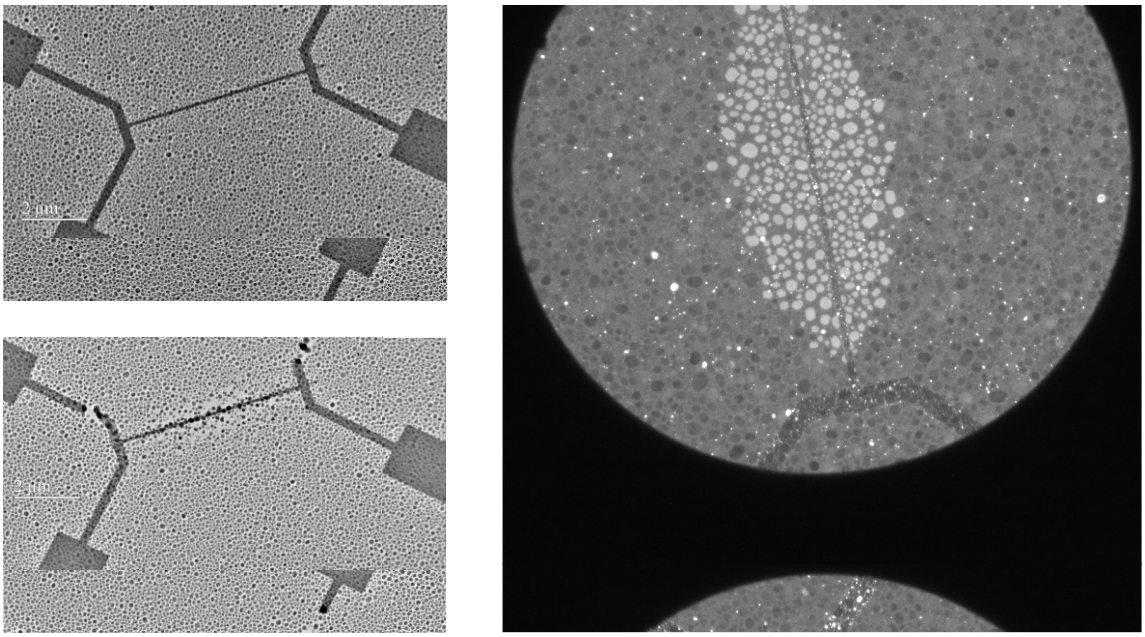

Figure 6.2: DF image of a Pd heater wire device demonstrating the contrast difference between solid (dark) and melted (light) In islands.

The thermal measurement were conducted using a steady-state *DC* Joule heating technique inside a transmission electron microscope. By operating the TEM in the appropriate dark field condition the melting of the In islands was observed by a contrast difference between the solid and liquid islands, as described previously in chapter 4 (see figure 6.2).

6.1.1: Joule Heating

The heat generated in the metal wire due to Joule heating and the heat loss to the substrate is expressed by the steady-state heat diffusion equation:

$$\nabla(k\nabla \mathrm{T}) + Q_{dc} = 0 \qquad (6.1)$$

Where k is thermal conductivity, T is temperature, and Q_{dc} is the heat generated due to Joule heating in the nanowire. The heat generated can be expressed in terms of the applied electric power, $P = IV = V^2/R$, and directly measured using the current and

voltage values from the power supply. The thermal conductivities with the largest influence on the heat dissipation in a given device are the thermal conductivity of the Pd heater wire, k_{Pd}, and the thermal conductivity of the SiN membrane, k_{SiN}.

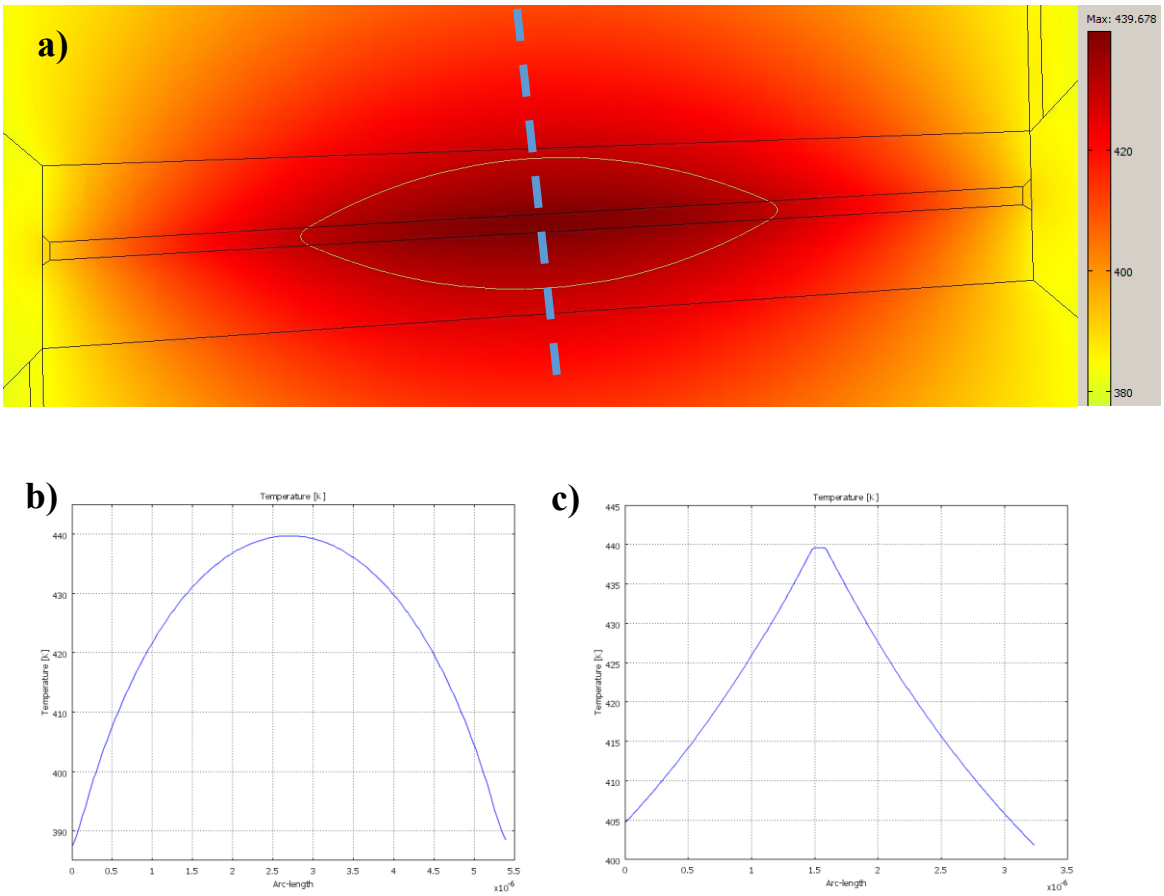

Figure 6.3: (a) Simulated results, showing the temperature gradient across the membrane in the vicinity of the heater wire. (b) Temperature profile of the Pd metal along the length of the heater wire. (c) Temperature profile of the SiN along the dashed line in (a), perpendicular to the heater wire.

6.2: Pd Thermal Conductivity

6.2.1 Pd Thermal Conductivity

The thermal conductivity of the metal can be predicted from its electrical conductivity, σ, based on the Wiedemann-Franz Law, [73], as described in more detail in Chapter 4. As such it is important to have an accurate measure of the electrical conductivity in characterizing the joule heating of the nanowires in a given device. The electrical conductivity of most metals have been precisely measured and have been well documented [84]. However, it can be influenced by extrinsic effects like disorder and grain structure, and as the dimensions of the material decrease and begin to approach the mean free path of the conducting electrons its electrical conductivity may also begin to deviate from the bulk value [85, 86]. In addition, the heat generated from resistive heating is directly dependent on the electrical conductivity of the metal. Consequently, to avoid discrepancy in resistivity measurements throughout the device, due to geometrical variations, a 4-probe device design was implemented. The improved setup allows direct measure of the potential drop across the heater wire and avoids the resulting error in the k_{pd}, due to variations in σ values, as it makes it possible to directly measure the resistivity of the nanowire for each device. Figure 6.4 shows the schematic of one such device and the remaining of this chapter will focus on analyzing such devices.

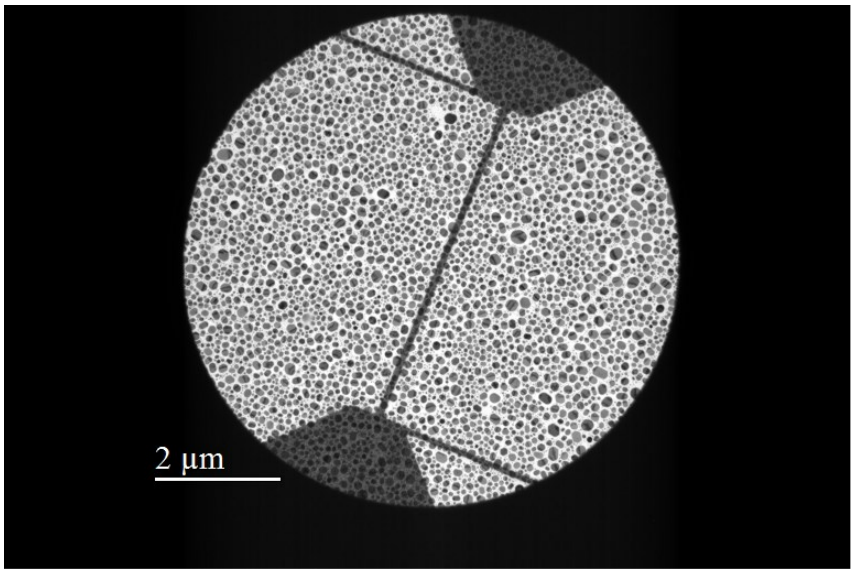

Figure 6.4: BF image of a Pd heater wire additional probes at either sides of the wire to facilitate four probe voltage measurements.

Using an external *DC* source-measure power supply, a potential is applied across the device while the current values are monitored throughout the ramping process using a LabVIEW program. In addition, the two sense nanowires on either side of the heater wires are simultaneously connected to a voltmeter which allows the exact potential drop to be measured. Figure 6.5 shows experimental *I-V* from a typical heater wire device.

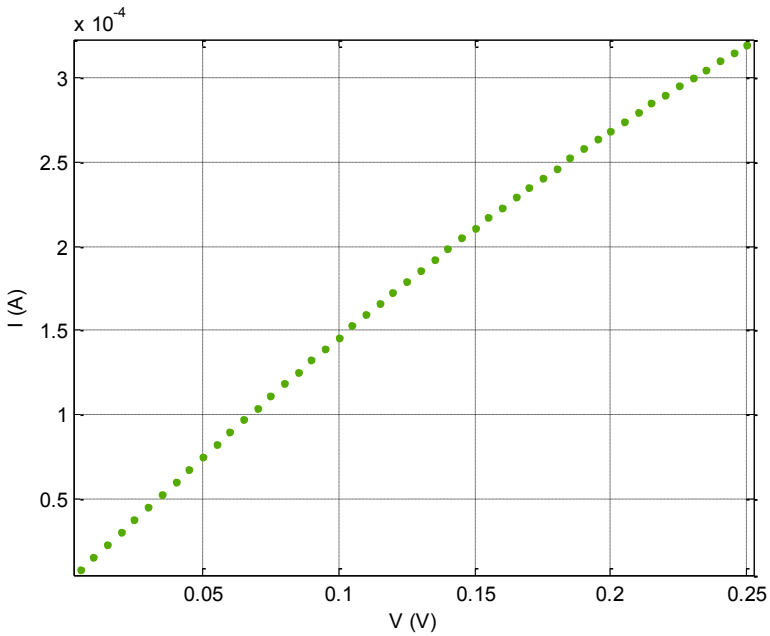

Figure 6.5: Experimental I-V curve from the Pd heater wire device.

And the corresponding resistance values are shown in figure 6.6.

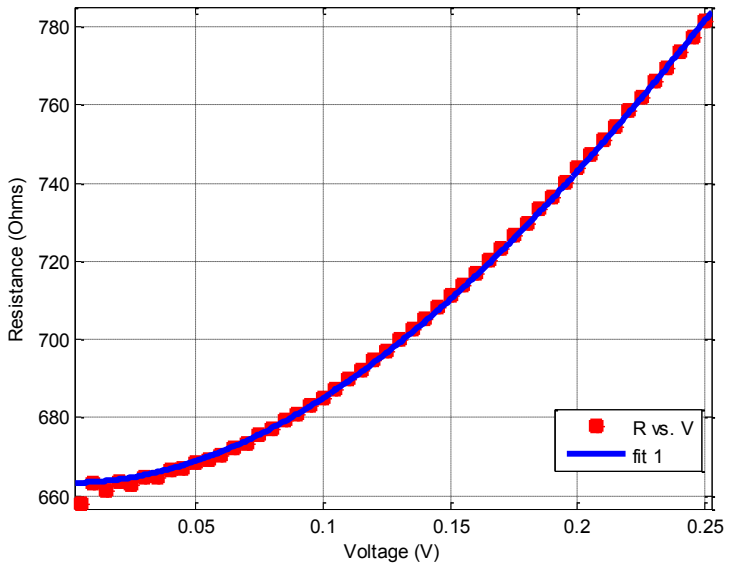

Figure 6.6: Resistance of the Pd heater wire device up to 250mV. The resistance behavior can be explained by a simple joule heating model, blue line.

6.2.2: Thermal Coefficient of Resistance: α

The change in resistance of the device is attributed to the temperature rise across the heater wire due to joule heating. This change is characterized by the thermal coefficient, α, and is represented by

$$R = R_0\big(1 + \alpha(T - T_0)\big) \tag{6.2}$$

where R_0 is the resistance at reference temperature, $T_0 = 293\ K$. The voltage dependence of the calculated resistance values can be understood by modifying equation 6.2 to be defined in terms of Fourier's Law for heat conduction, $Q = k\nabla T$, where the temperature can be expressed in terms of the thermal conductivity and the heat generated in the metal

$$R = R_0\left(1 + \alpha\frac{Q_{dc}}{k}\right) \tag{6.3}$$

Expressing the heat source, Q_{dc}, as a function of electric power, $P = V^2/R$, the equation for the resistance of the heater wire can be written as

$$R \propto R_0\left(1 + \alpha\frac{V^2}{Rk}\right) = \frac{R_0}{2} + \frac{\sqrt{R_0}\sqrt{kR_0 + 4\alpha V^2}}{2\sqrt{k}} \tag{6.4}$$

Equation (6.4) was fitted to the experimental resistance values and shows to be in good agreement and shows typical joule heating behavior (see blue line in figure 6.6). The fit allows the parameters R_0 and α to be precisely determined.

6.3: Measurements and Analysis of k_{SiN}

In addition to the heat source in the system, the thermal conductivity of the membrane is a key component in dictating the observed temperature profile. The k_{SiN} indicates the efficiency by which heat is taken away from the heater wire to the edges of the membrane, maintained at 293 *K*, and it thus defines the thermal gradient across its surface of the substrate. The strength of the TEM thermal imaging technique lies in its ability to provide real time high resolution information about heat conduction by nanomaterials. However, it is important to remember that the measured quantity is the temperature of the In islands, which in turn shows the temperature of the electron transparent substrate they are attached to. Therefore, quantitative understanding of heat dissipation in fabricated devices requires a detailed understating of the thermal characteristics of the In and the membrane.

If the In on the back side of the membrane is deposited as a continuous thin film then its thermal conductivity will greatly influence the observed melting profile. However, due to the discontinuous nature of the In, the thermal conductivity of the membrane, k_{SiN}, dictates the observed melting profile. As such, it is necessary to have a reliable value of the thermal conductivity of the substrate as well as its TBR with the components of the fabricated devices.

6.3.1: Black Body (far-field) Radiation

With no convective heat transport due to the low operation pressure, black body radiative heat transfer mechanism was also taken into consideration in the simulations described below. To this end, the heat diffusion equation was modified by including an additional $(T_0^4 - T^4)$ dependent heat flux based on the Stefan Boltzmann

law. However, due to relatively low operating temperatures of below 600 *K* little radiation effect was observed, with less than 1 *K* variation in the simulated results. Consequently, the simulations assumed no black body radiation and used an exclusively conductive heat transfer model to simulate the experimental results.

6.3.2: Modeling Procedure

These calibration studies are modeled using finite-element analysis of the geometry, which is constructed directly from TEM images, using the commercial package, COMSOL, version 3.5. The model includes the entire structure of the device on the suspended 250 μm x 250 μm window. Due to the heat sinking of the supporting SiO_2 layer, the edges of the membrane are defined to be at room temperature, 293 *K*. The model couples the electrical and heat transport physics to simulate the joule heating and the induced temperature gradient across the SiN membrane, based on the governing equations discussed above. By matching the simulated temperature gradient across the membrane to the observed melting profile of the In islands for a given device geometry at a given voltage bias it is possible to gain quantitative understanding of the electrical and thermal properties. In the model, the thermal conductivity of the membrane is set as a free variable and is varied to find the proper k_{SiN} value which will yield the experimental melting profile. In addition to the k_{SiN}, the resistivity of the metal also plays a critical role in determining the magnitude of the heat generated, which is similarly quantitatively extracted through the simulations by matching the experimentally measured *I-V* curves. The schematic of the iterative modeling process is shown in figure 6.7.

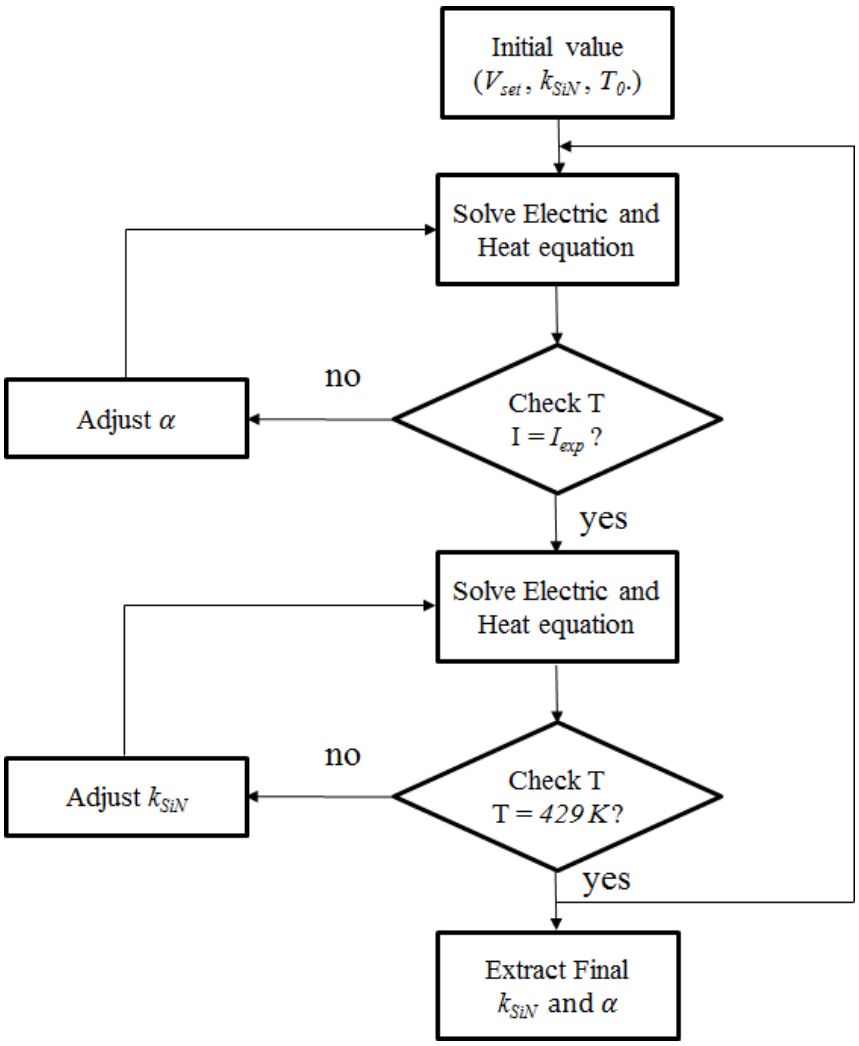

Figure 6.7: Block diagram of the simulation method used to extract k_{SiN} by matching the melting front of the In islands for a given voltage, V_{set}.

The model is set up using a reasonable starting value for the k_{SiN} from literature and the temperature gradient is considered to be uniformly at T_0. As an initial step, the finite-element analysis solves the electrical continuity equation for a given applied voltage, V_{set}, and calculates the appropriate current given the geometry and resistivity of the device. The room temperature resistivity, ρ_o, of the device is calculated by matching the current at lower voltages where there is little temperature rise in the metal due to joule heating. Using the extracted resistivity, ρ_o, the thermal

coefficient of resistance, α, is extracted at higher applied voltages by matching the I_{sim} to I_{exp}. At each iteration step, the new effective resistivity value is used in calculating the thermal conductivity of the metal from the Wiedemann Franz-law and the heat generated by joule heating, Q_{dc}, is calculated.

Next, the model uses the calculated Q_{dc} as a heat source and solves the heat diffusion equation to measure the temperature gradient, T_{calc}, across the membrane. From the experimental TEM pictures, the melting front of the In islands for a given voltage can be observed with great accuracy. Considering a melting point of 429 K for the In islands, the k_{SiN} is varied until the temperature at the position of the melting front becomes 429 K. The model uses the final temperature profile across the device and repeats the calculations to create an improved estimate of Q_{dc} and in turn a new thermal profile until it converges with acceptably small variation in the calculated results (less than 0.1%). The loop is relatively efficient and quickly reaches a convergence in about 5 iterations.

Similar to the published results by Britlinger et. al [63] the thermal conductivity of the SiN membrane was extracted from matching the simulation to the experimental measurements at the lowest voltage where initial melting occurs. From the tested 4-probe devices on 50 *nm* membranes, the extracted k_{SiN} value was between 3.2 -3.97 *W/m.K* similar to the previous published result of 3.6 W/m.K [63]. The variation in the thermal conductivity values were initially attributed to small differences in the membrane due to fabrication process and the induced error from inaccuracies in measuring the electrical properties of the device.

6.3.3 Measurements of SiN-Pd TBR

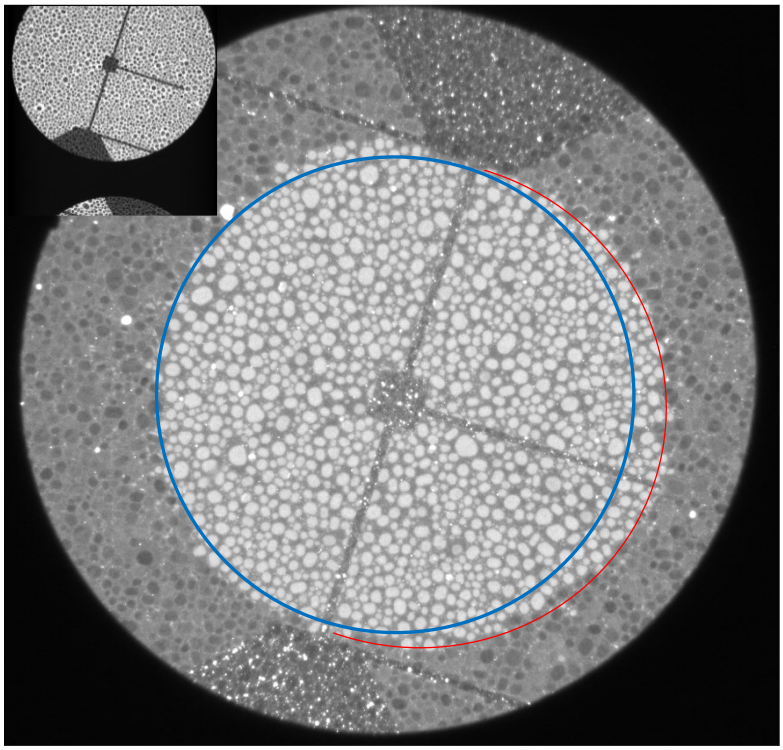

Figure 6.8: DF image of a device used to quantify the thermal contact resistance between the Pd and the substrate from the observed asymmetry, indicated with the red line. The inset is the BF image of the same sample.

As described, the heater wire devices are used to quantify the thermal conductivity of the substrate. However, the extracted value includes the thermal boundary resistance, TBR, between the Pd heater wire and the SiN. This becomes a problem when modeling devices without a Pd heater wire, such as active CNT devices, the Pd-SiN contact resistance needs to be subtracted from the k_{SiN} term. To quantify the contact resistance, the devices were modified by the deposition of a line of Pd metal extending perpendicular to the right of the heater wire, as seen in the inset of figure 6.8. The result from the addition of the Pd line is a noticeable asymmetry in the melting profile of the In islands for a given bias voltage, indicated in figure 6.8,

by the deviation of the red line from the blue symmetrical marker. To incorporate the contact resistance in the model the Q_{dc} term was slightly modified in the governing heat equation by incorporating a thermal contact resistance between the Pd and the SiN, R_{th}.

$$Q - \frac{T_{metal} - T_{SiN}}{R_{th}} \tag{6.4}$$

The new parameter dictates how efficiently heat is transferred from the Pd, T_{metal}, to the nitride, T_{SiN}. From the iterative process an R_{th} value was extracted such that the model simulated the experimentally observed asymmetry. Using this process we extracted a contact resistance of $1x10^{-8}\ m^2\ K\ /W$ for the R_{th} which were used in all successive models. This value is relatively low, compared with other thermal resistances in our devices, and it is consistent with several other published TBR values for comparable material interfaces [87].

6.3.4: Voltage Dependence of k_{SiN}

Having extracted the k_{SiN} for a given device based on its initial melting, the simulated results are compared to experimental melting profiles for consecutive voltage values. Based on the simulations, it is quickly apparent that either the k_{SiN} had to change to match the melting profile, as the potential across the heater wire increased, or there is another unaccounted physical parameter which dictates the thermal gradient, in addition to the k_{SiN}. Figure 6.9 shows the expansion of the melting profile in terms of the distance of the melting front, measured perpendicularly from the center of the heater wire. Plotted as a function of applied voltage, the

melting profile increases as the heater wire is gradually heated via joule heating, as it would be expected from a simple heat transport model.

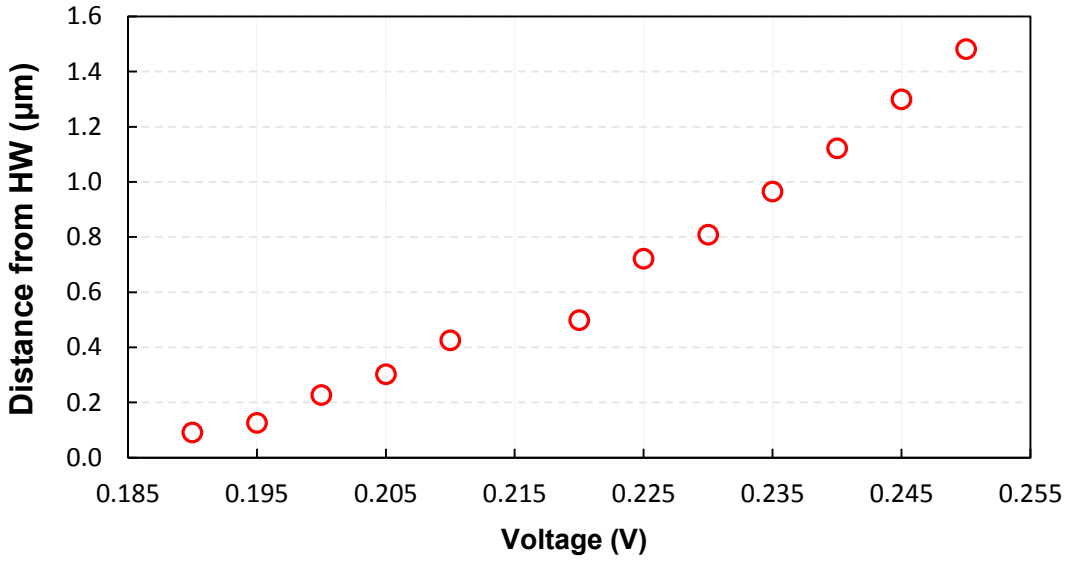

Figure 6.9: Distance of the melting front perpendicular to the heater wire for each voltage step. We note that there is a deviation of melting front at 220 mV which we attribute to the non-uniform size distribution of the In at that vicinity.

The simulation method described above is applied to each voltage step and indicated the need for a change in the value of the k_{SiN} to match the experimental melting profile. The process was carried out for all voltage steps and is plotted in figure 6.10. At each voltage, value the electrical properties are checked to ensure the correct current density within the heater wire. The simulations show a factor of 1.54 increase in the thermal conductivity value as a function of applied bias, from 190mV to 250 mV.

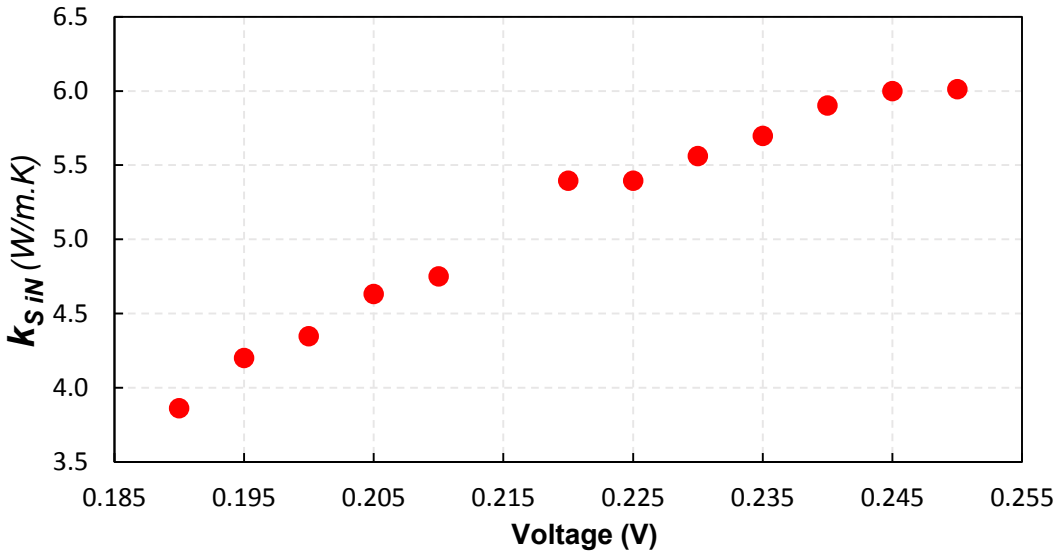

Figure 6.10: k_{SiN} values extracted from the simulations for each voltage step

The same device geometry was tested on a thicker, 100 nm, membrane and finite-element model was again carried out (see figure 6.11). Based on the extracted k_{SiN} values from initial melting points, the results show an increase in the smallest k_{SiN} value by a factor of 2.3 from 3.88 to 9.03 *W/m.K*. This rise in k_{SiN} for thicker membranes may tentatively be assigned to reduced surface scattering of phonons. More significantly, similar to the 50nm membrane, it was observed that simulations required the k_{SiN} to be increased for increasing bias to match the melting profile, as seen in figure 6.12.

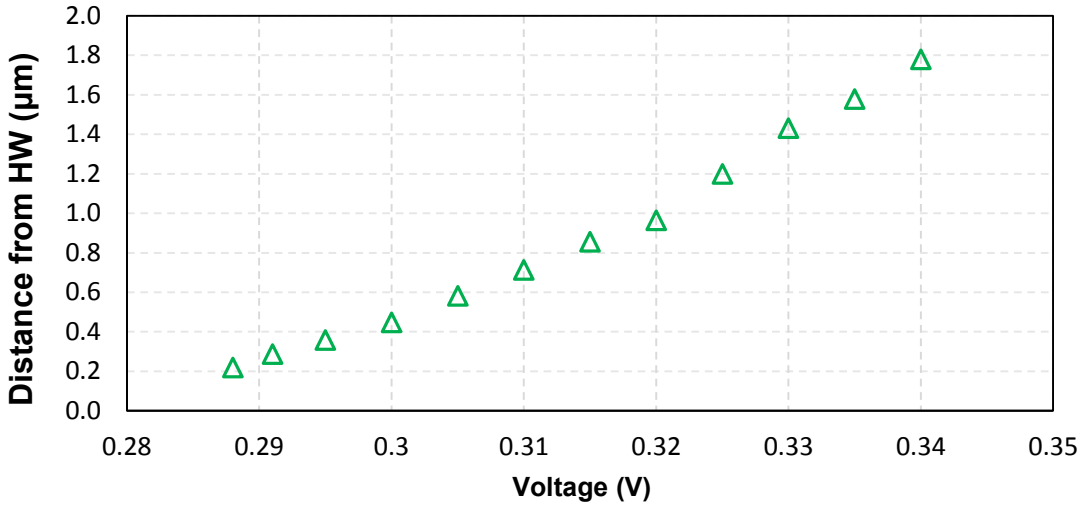

Figure 6.11: Distance of the melting from perpendicular to the heater wire fabricated on a 100nm membrane.

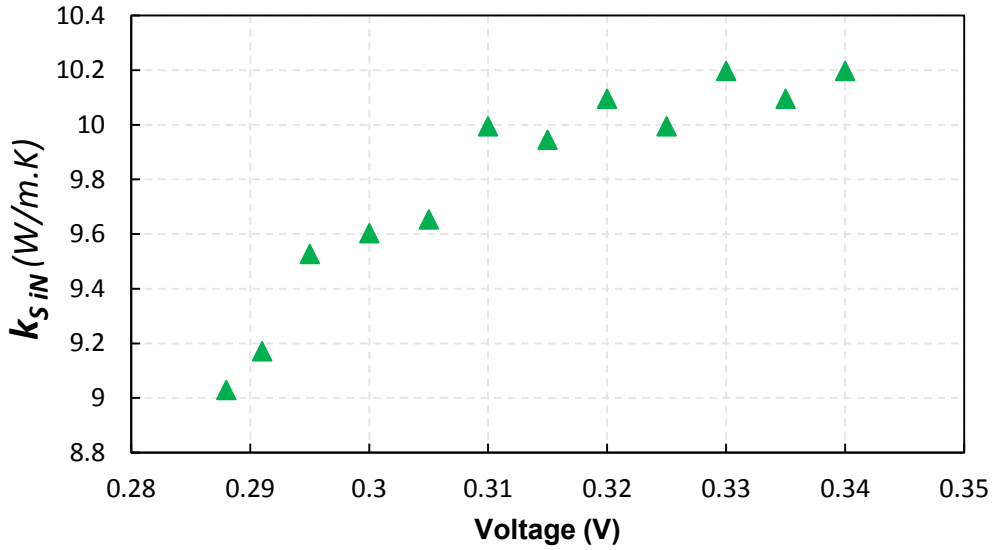

Figure 6.12: k_{SiN} values for a device on a 100nm membrane extracted from the simulations for different applied voltages.

Plotting the data from both 50 *nm* and 100 *nm* thick membranes as a function of applied power clearly demonstrates the required change in the k_{SiN} (see figure 6.13).

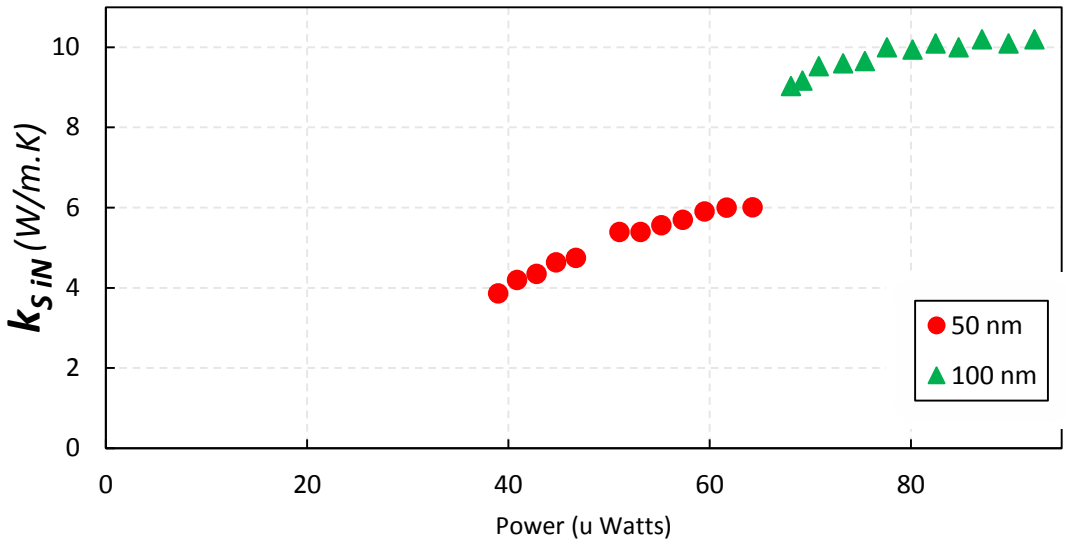

Figure 6.13: k_{SiN} values for both 50nm (blue) and 100nm (orange) as a function of applied power on the heater wire.

Throughout all the simulations discussed, the thermal conductivity of the membrane was considered to be constant across the entire interface. In other words, the k_{SiN} was assumed to have no spatial or thermal dependence. The following section will disregard such assumptions and try to modify the simulation to gain insight into the physical cause for the variation in k_{SiN} observed.

6.3.5: Influence of beam on k_{SiN}

One possible explanation for the discrepancy in the k_{SiN} value may be the effect of the electron beam on the device. As discussed previously, beam effects may cause problems when trying to measure the heat transport mechanism as they can act as additional heat source. The selected imaging conditions ensure that there is negligible beam heating, and that the intensity of the beam is uniform across the field of view. As described in chapter 4, the data is collected at spot size = 4 with the first

condenser aperture inserted to avoid influencing the melting profile of the In islands. In addition, the uniformity of the intensity of the beam is ensured based on the use of a defocused condenser illumination in the operating dark field condition. However, even with eliminating beam heating there may be other beam effects that need to be accounted for when employing our electron thermal imaging technique. For example, it is possible that electrons from the beam are introducing additional phonon scattering mechanisms which reduce the mean free path of the phonons within the substrate, thus reducing the k_{SiN}. Alternatively, the electron may cause the phonon distribution to be non-thermal thus enhancing Umklapp scattering in the exposed region.

In order to test the theory, the simulation was modified to include two regions of SiN. In the model, the membrane in the beam exposed area was given different thermal properties than elsewhere. As seen in figure 6.14, a circular region with radius ~3.5μm was selected such that an independent thermal conductivity value could be given to the area inside the circle, blue area, and the area outside the circle, grey area. Using this model, an iterative process was employed in which the melting front was matched at low voltage of 195 mV by varying k_{SiN_in} while the k_{SiN_out} was varied to match the melting profile at the higher voltage of 240mV. By the conditions imposed in this model the simulation agreed with the experiment at the 195 mV and at 240 mV, with extracted k_{SiN_in} = 2.205 $W/m.K$ and k_{SiN_in} = 6.67 $W/m.K$. However, once again the simulated temperature profile did not match the experimental results for the other voltages (see figure 6.15). From this, we conclude that the model does not reflect an observable phenomenon in our studies.

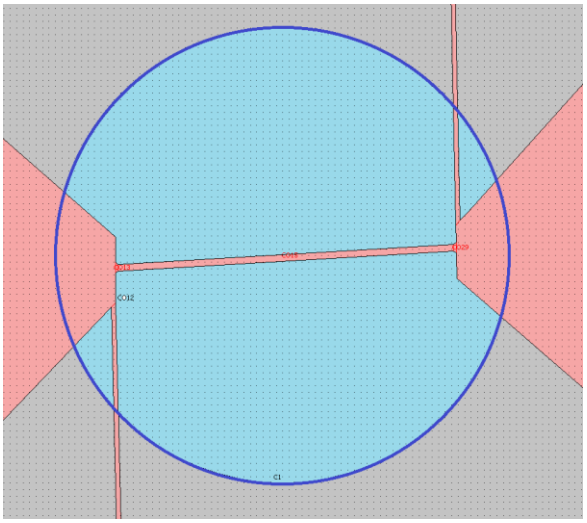

Figure 6.14: Model used to test beam effect, applying a separate thermal conductivity to the beam exposed region (blue) as compared to the rest of the membrane (gray).

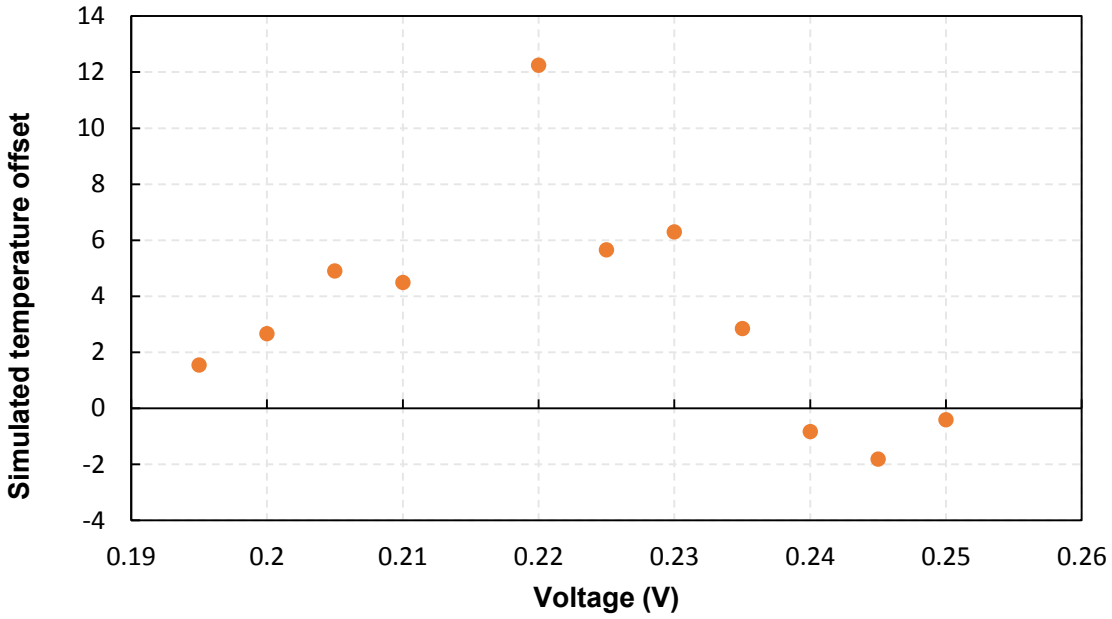

Figure 6.15: Simulation results for testing beam effects using different thermal conductivity values, the simulation produces the correct temperature gradient at 195mV and 240mV however the temperature profile at all other voltages deviate from experimental results.

6.3.6: Influence of In Islands on k_{SiN}

In the simplest models the membrane is treated as having a homogenous thermal conductivity. However, in reality the presence of the In islands create discrete regions of high thermal conductivity due to their high electron conductivity, according to Wiedemann-Franz law. The heterogeneous nature of the thermal conductivity, due to the In, may serve as a *prima facie* explanation for the discrepancy of the simulated thermal profile.

The In islands across the free standing membrane have an average diameter of 100 *nm* and are about 100 *nm* apart. Including islands of such dimensions across the entire 250 x 250 μm model makes the model computationally expensive. Instead the model was designed to include the islands in a small region of interest. The thermal conductivity within the region is the combination of k_{inside} and k_{In} and the thermal conductivity outside the region is denoted by $k_{outside}$, gray region in figure 6.16. For the simulations the k_{In} was defined according to Widemann Franz law to be 81.8 *W/m.K*, based on literature electrical resistivity values for bulk In of 83.7 $n\Omega \cdot m$. The k_{inside} and $k_{outside}$ were extracted, to be 1.14 *W/m.K* and 6.89 *W/m.K* respectively, in an iterative process by matching the melting profile at low voltage, 195 *mV*, and high voltage, 240 *mV*, respectively. Although the model accurately simulated the temperature profile at 195 *mV* and 240 *mV*, it failed to do so in all other voltages. Remarkably the offset in the simulated temperature for the other voltages was similar to the results from section 6.3.5 (see figure 6.17).

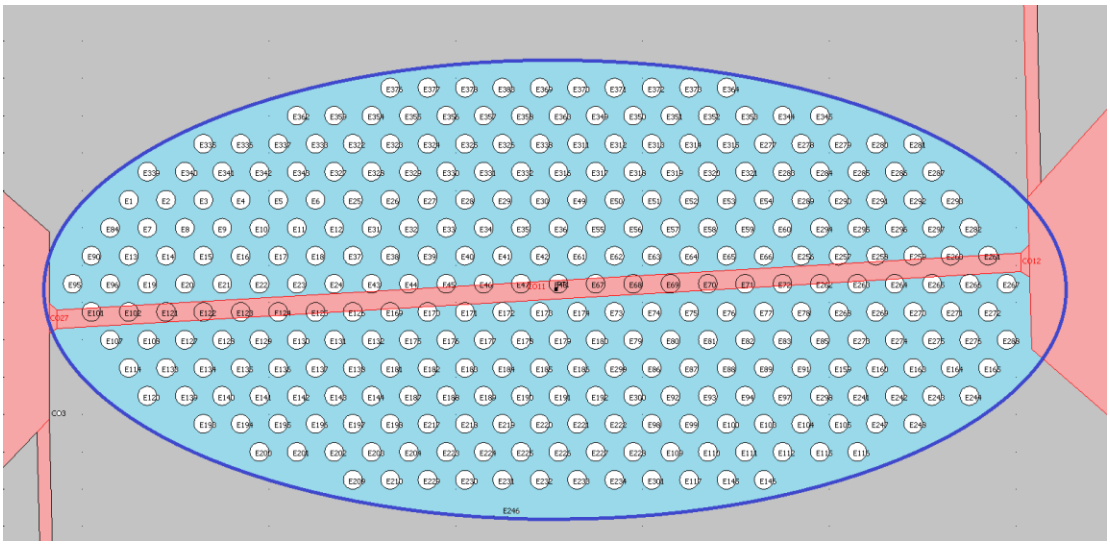

Figure 6.16: Model used to test effect of In islands on the extracted value of the thermal conductivity of the substrate.

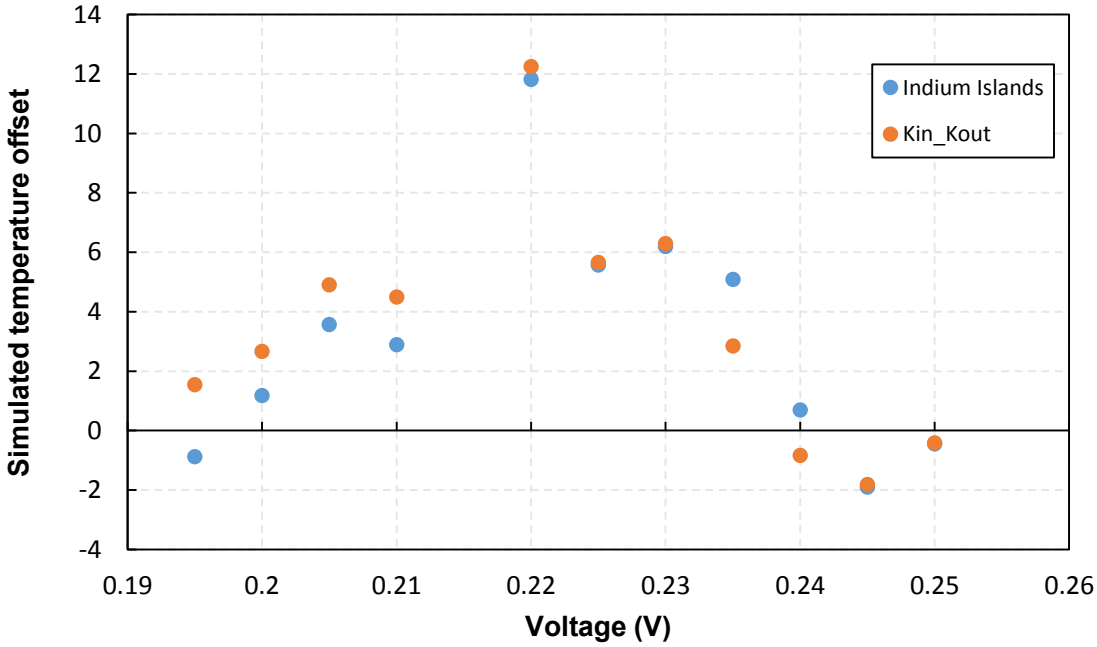

Figure 6.17: Simulation results for testing beam effects using different thermal conductivity values (orange) in addition to results from simulating the effect of individual In islands on the total melting profile (blue).

6.3.7: Influence of Temperature on k_{SiN}

As stated earlier, the models used had treated the k_{SiN} as a constant parameter across the entire membrane. However, it is known that all materials exhibit a temperature dependence on their thermal conductivity [88, 89]. Considering such temperature dependent thermal conductivity will result in a spatially varying k_{SiN} across the substrate due to the temperature gradient from joule heating, which may explain the simulated deviation from the experimental results. As such, the thermal conductivity was treated as a linear function of temperature

$$k_{SiN}(T) = k_0 + m * (T - T_0) \tag{6.4}$$

Where k_0 is the thermal conductivity at room temperature, T_0, and m is the temperature coefficient of thermal conductivity. Having calibrated the metal's thermal coefficient of resistivity, α, using the *I-V* data at low voltages up to 50 mV (with minimal joule heating), was used to extract the value of k_0. Separately, the slope, m, was extracted at 195 mV, V_m, by matching the indium melting profile. With k_0 = 3.6 $W/m.K$ and m = 0.0034 $W/m.K^2$, the simulation was evaluated at other voltage values, and a table of the resulting m values is shown in table 6.1. From this, it is clear that the approach fails to reproduce the experimental observations. None of the linear functions were able to predict the correct temperature gradient for any of the voltages besides V_m. Below, we conduct a more detailed analysis of the temperature dependence of $k_{SiN}(T)$, which holds up this basic observation.

V_m (mV)	195	200	210	220	230	240	250
m ($W\ m^{-1}\ K^{-2}$)	0.0034	0.00789	0.0118	0.0201	0.0221	0.0255	0.0298

Table 6.1: m values extracted from equation 6.4 using $k_0 = 3.6$ and $T_0 = 293\ K$ for different voltages.

In addition to the linear model, a second order polynomial dependence, in terms of coefficient *A*, *B*, and *C* is also analyzed,

$$k_{SiN}(T) = A + B(T - T_0) + C(T - T_0)^2. \tag{6.5}$$

The fitting parameters for this model rely on using the melting profile at 195mV, 225mV, and 250mV to evaluate their corresponding thermal conductivities k_l, k_m, and k_h by solving the system of equations

$$k_l = A + B(T_l - T_0) + C(T_l - T_0)^2$$

$$k_m = A + B(T_m - T_0) + C(T_m - T_0)^2$$

$$k_h = A + B(T_h - T_0) + C(T_h - T_0)^2$$

The constants A, B, and C are expressed in terms of k_l, k_m, k_h and their corresponding temperature T_l, T_m, and T_h extracted from the model.

$$A = \frac{k_m(T_h - T_l)(T_h - T_0)(T_l - T_0) - \big(k_l(T_h - T_m)(T_h - T_0) - k_h(T_l - T_m)(T_l - T_0)\big)(T_m - T_0)}{(T_h - T_l)(T_h - T_m)(T_l - T_m)}$$

$$B = \frac{k_m(T_h - T_l)(T_h + T_l - 2T_0) - k_l(T_h - T_m)(T_h + T_m - 2T_0) + k_h(T_l - T_m)(T_l + T_m - 2T_0)}{(T_h - T_l)(T_h - T_m)(T_m - T_l)}$$

$$C = \frac{k_m(T_h - T_l) + k_h(T_l - T_m) + k_l(T_m - T_h)}{(T_h - T_l)(T_h - T_m)(T_l - T_m)}$$

An iterative process is used to evaluate the parameters at each corresponding voltage, where the final value is used in evaluating the next voltage point. However, once again the process is unable to produce a model to successfully predict the experimental results for all voltages. In this case, the simulations failed to converge,

and iterating among the voltage values produces diverging values of A, B, and C. The quadratic dependence is unable to reproduce the correct melting profile at 195mV, 225 mV and 250 mV for any combination of A, B, and C. As we show below, we may actually conclude that no model for $k_{SiN}(T)$ alone may resolve the discrepancies of our more simple model.

6.3.8: Analysis of ΔT vs. Δk_{SiN}

To compare the disagreement from the simulations to the experimental results, the temperature offset is evaluated for the entire voltage range. From the melting front of the In islands, distance r_{exp} away from the heater wire, the temperature of the substrate is known to be 429 K, denoted as T_{exp} in figure 6.18.

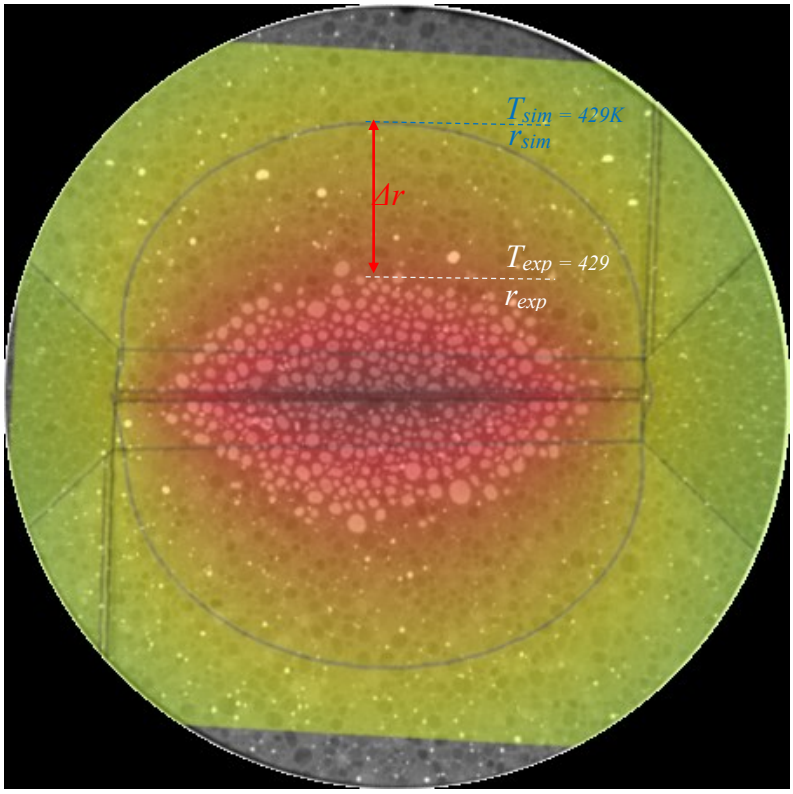

Figure 6.18: Overlay of the simulated and experimental thermal profile of the device indicating the discrepancy between simulation and observed results.

As discussed earlier in this chapter, using the iterative modeling process produces a unique k_{SiN} value for each given voltage, V_k. However, the extracted parameters result in a disagreement at other voltage values where the simulations overestimate the temperature if evaluated for voltages above V_k, $V_{sim} > V_k$, or alternatively underestimate the temperature if $V_{sim} < V_k$. By modeling the device based on a constant k_{SiN} value, extracted from the initial melting voltage at $V_k = 190$ *mV*, all voltages are evaluated and the discrepancy is quantified in terms of deviation in temperature from the melting point of In, 429 *K*, at the experimentally observed melting front location, $T_{sim}(r_{exp}) - 429$.

Figure 6.19 compiles the results and clearly demonstrates that the simulations overestimate the temperature for all voltages. The data also includes the simulated results from the models where k_{SiN} is assumed to depend linearly and nonlinearly on *T*. Surprisingly, both models yield almost identical deviations from the experimental results which is a clear indication that the temperature dependence of k_{SiN} is not the governing source of the error. More interestingly, from figure 6.19 it can clearly be seen that the amount of deviation begins to saturate at distance above 1 μm away from the heater wire, suggesting that an explicit spatially-dependent model may be more reflective of the underlying physics than a temperature-dependent model.

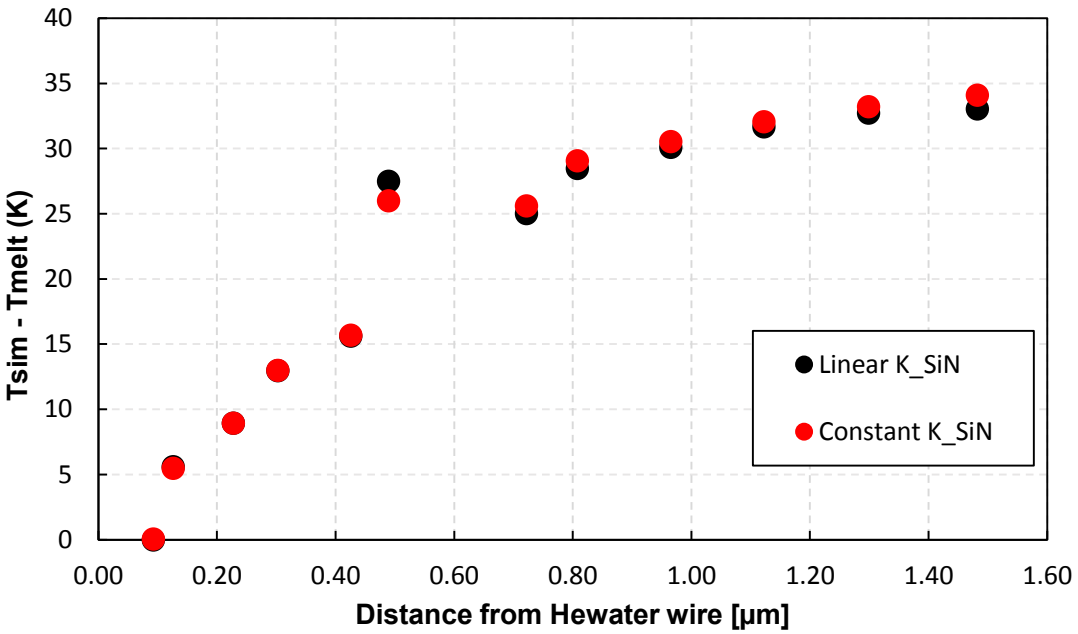

Figure 6.19: The discrepancy between the simulation and experimental results as a function of distance from the heater wire.

6.3.9: Influence of Stress on k_{SiN}

The correlation of the data with the distance from the heat source suggests a spatially dependent k_{SiN}, independent of the temperature gradient across the membrane. One possible cause for such a spatial dependence may be a stress induced variation in the thermal conductivity of the nitride across the region of interest [90,91].

Previous work [90] has shown a reduction in the thermal conductivity from 2.7 *W/m.K* at zero strain to 0.34 *W/m.K* (see figure 6.20).

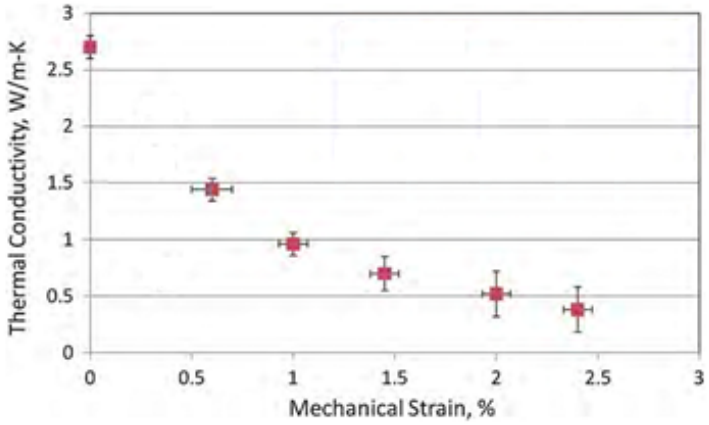

Figure 6.20: Reduction in substrate thermal conductivity due to mechanical strain.

The deposition of the metal electrodes on the free standing membrane causes a strain in addition to the estimated 0.2% residual strain [92]. However, the strain caused by device fabrication is quite far from the typically required fracture strain of 3% [93,94], thus it is unlikely that the strain gradient is the cause of the deviations of k_{SiN} that our modeling suggest. A qualitative understanding of the level of strain on the membrane can be seen from AFM images of one such device (see figure 6.21).

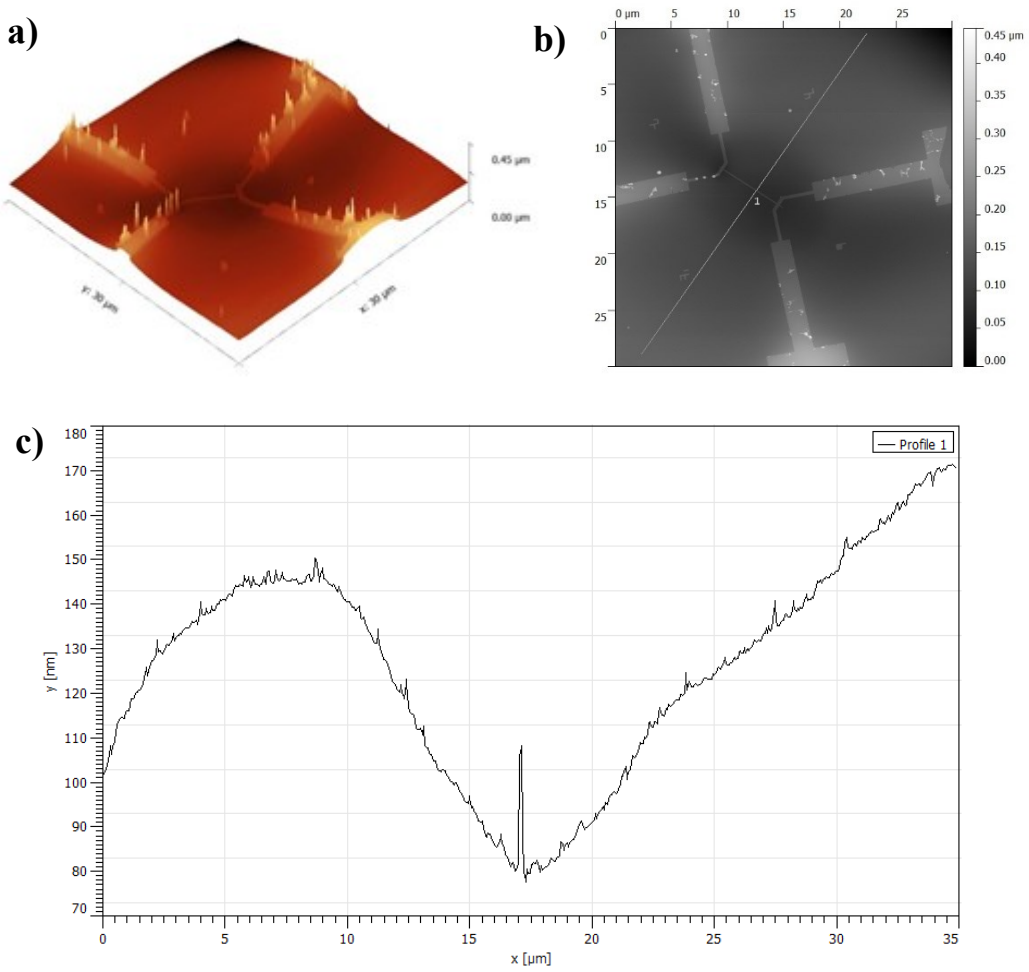

Figure 6.21: (a) AFM image of a typical heater wire device demonstrating a systematic rippling. (b) Line scan across the heater wire indicates 100nm of ripple over 35 µm.

Even though the data demonstrates a noticeable systematic rippling across the device, 100 *nm* of ripple over 35 μm is not very much when considering the total area to be 250 μm wide. This is consistent with a level of strain much less than 0.1%, the minimum required to produce an observable change in k_{SiN}. Thus, stress induced thermal effects should not be observable in our device geometries.

6.3.10: Explicit Spatial Dependence of k_{SiN}

Based on the different models, it is plausible to expect a spatially dependent k_{SiN}. To this end, the model was revised to include regions of varying thermal conductivity based on the position relative to center of the heater wire, as shown in figure 22. The geometry of the region was chosen to reflect the observed elongated shape of the melting profile along the length of the heater wire. Using the model, a unique k_{SiN} value is assigned to each region such that the simulated temperature gradient agrees with the experimental results.

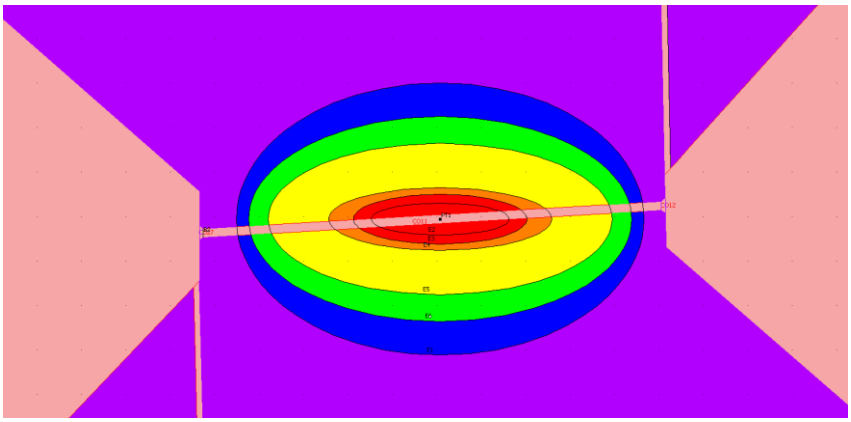

Figure 6.22: Model used to assign a unique k_{SiN} value to different region of the membrane

Since any change in one region directly influences the thermal profile in the other regions, the model could not be successfully compiled using a simple iterative method, as it quickly diverged. Consequently, to extract the individual conductivity of each region, the model parameters were simultaneously varied for all areas for multiple voltages using a constant of proportionalities for each region. The results, shown in figure 6.23, allowed the model to successfully and uniquely predict the correct melting profile of the In islands. The data presented as a function of distance

from the heater wire show a clear monotonically increasing thermal conductivity with increasing distance. In addition, it can be seen that the thermal conductivity begins to saturate after 1 μm away from the wire. Little can be said regarding the first data point, based on initial melting at 190 mV, which relies on the phase change of only a single 100 nm indium island. Considering the spatial resolution of the imaging technique it may be reasonable to ignore the first data point in initial efforts to understand the observed trend.

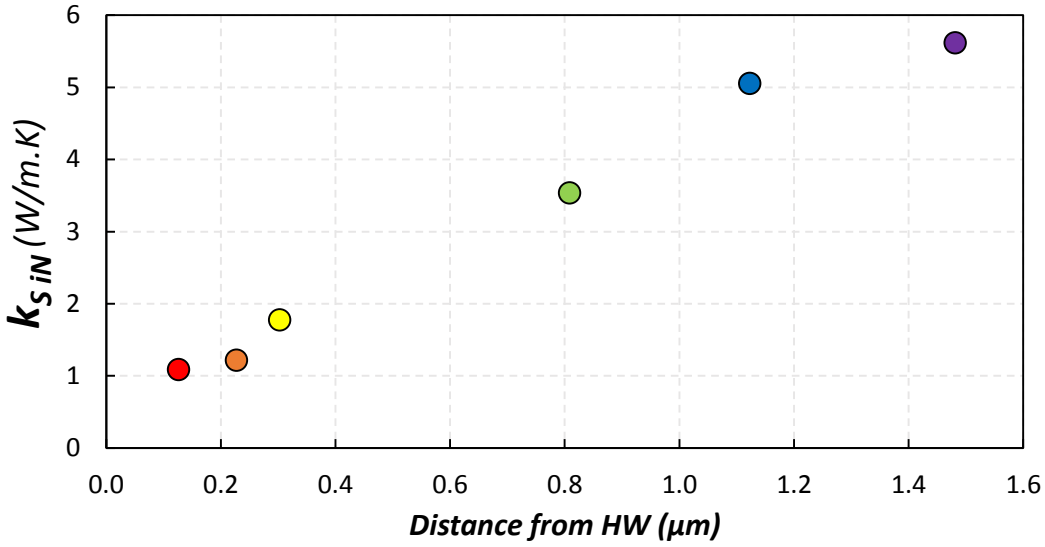

Figure 6.23: Extracted k_{SiN} values for each individual region, the colors in the plot correspond to the region sharing the same colors in figure 6.22.

The strength of the spatial dependent model can be clearly seen when the results are compared to the previous simulations, which used a unique k_{SiN} for each voltage, as seen in figure 6.24. Using a constant thermal conductivity extracted by matching the melting profile at the low voltage of 190 mV ($k_{SiN} \sim 3.86$ $W/m.K$) the simulation clearly overestimates the temperature gradient of the device (see figure 6.24a). While on the other hand, using a constant thermal conductivity extracted by matching the melting profile at the high voltage of 250 mV ($k_{SiN} \sim 6.01$ $W/m.K$)

underestimates the temperature gradient as seen in figure 6.24b. It is only when using the spatial dependent model that the simulated results, as shown in figure 6.24b, agree with the experimental melting profile (figure 6.24a).

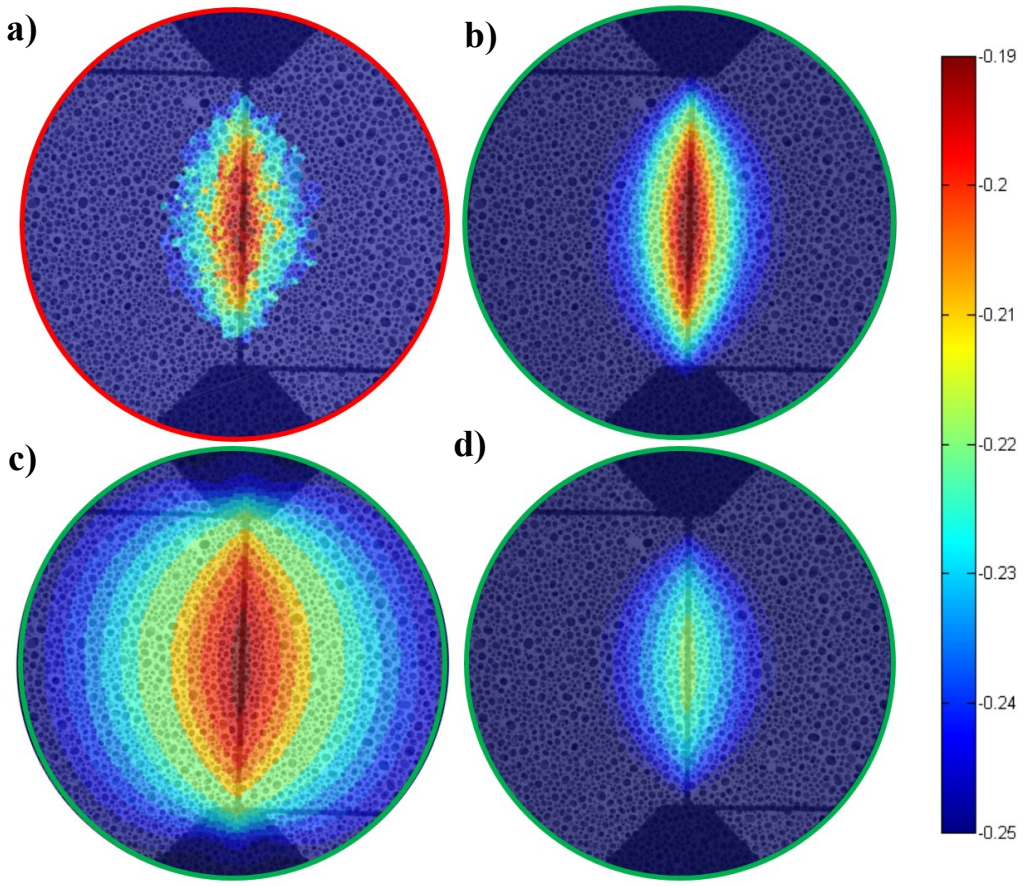

Figure 6.24: (a) Experimental thermal map indicating the voltage where each island melts. (b) Simulated voltage map generated using the spatial dependent model. (c) and (d) Simulated voltage map generated using a constant k_{SiN} extracted by matching the melting profile at the low voltage (c) and high voltage (d).

It is important to note that this is the first model presented that satisfactorily predicts the observed indium melting profiles and their voltage dependence. However, this model invokes an explicit and arbitrary spatial dependence to k_{SiN},

which prevents the utility of the model for measuring unknown thermal quantities in other similarly fabricated structures. If a model of the underlying physics for the spatial-dependence of k_{SiN} could be developed, it might allow such studies to be conducted in the future. We now turn our focus to developing such a model.

6.4: Near field thermal conduction

One plausible cause of a distance-dependent thermal model can be understood in terms of near-field radiation. As described in more detail in chapter 1, near-field radiation exists in all materials with a non-zero temperature due to thermal and quantum fluctuations. Generally, radiation is described in terms of Plank's black body radiation for two bodies with distances greater than the dominant emitting wavelength, $d > \lambda$. However, when objects are separated by less than the dominant wavelength, $d < \lambda$, near-field radiation may sometimes play an important role as a heat transport mechanism [14,20].

With temperatures of about 429-600 K the associated peak wavelength is between 6.75 – 4.83 μm, calculated from Wien's displacement law

$$\lambda_{peak} T = b \qquad (6.6)$$

where b is the Wien's displacement constant, equal to 2.897 x 10^{-3} (m K) [95]. Consequently, considering the sub-micron geometry of the devices under consideration, and the maximum melting profile of below 1.6μm it is reasonable to suspect near-field effects possibly to play a role in heat dissipation.

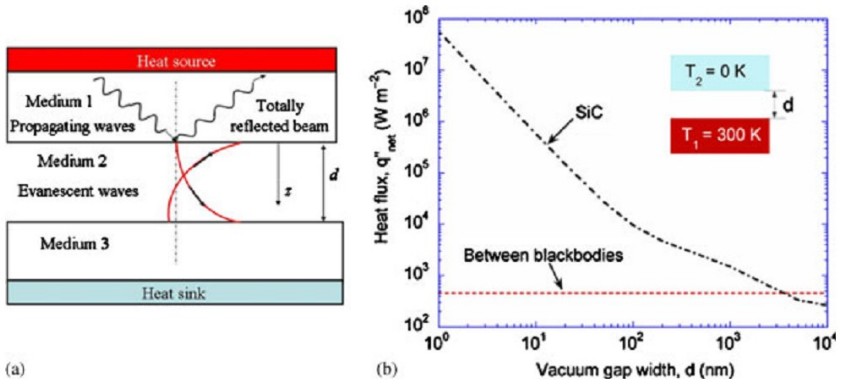

Figure 6.25: (a) Schematic illustrating evanescent waves between two flat surfaces with d < λ. (b) Radiative heat transfer between two SiC plates [19].

Near-field radiation results in enhanced heat transport mechanisms due to evanescent electromagnetic fields which exist on surface of emitters [19]. Although these evanescent waves result in considerable increase in heat transport close to the interface, their effects exponentially decreases with distance. Based on such a model, it is reasonable to expect enhanced heat transfer close to the heater wire. Using such basis it is possible to qualitatively explain the simulated discrepancy with the experimental results.

Even though the model does not incorporate the physics to correctly reproduce the near-field enhanced heating data, which show a decreased k_{SiN} near the heater wire, it is possible to simulate the same behavior in terms of the conductive heat transport model. The exponentially decreasing near-field effects as a function of distance results in a temperature gradient across the membrane relative to the heat source such that it is sharpest closest to the heater wire. In a conductive model, the temperature gradient is related to the thermal conductivity and the heat generated in the nanowire by Fourier's law, $\nabla T = \frac{Q}{k}$. As discussed above, the Q_{dc} value is

accurately quantified from the *I-V* data and thus the k_{SiN} is the degree of freedom used to simulate the correct thermal profile across the membrane. As such, given the inverse relation of k_{SiN} with the temperature gradient a near-field effect will be manifested by a spatially dependent k_{SiN}, with the smallest value closest to the heat source. Consequently, the results from our model with different regions of thermal conductivity qualitatively support a near-field phenomena that shows an increasing thermal conductivity near the heat source. The saturation at distances greater than 1μm represents the decaying strength of the evanescent waves.

6.4.1: Delocalized Heat Source Model

Without a well-established physical model to simultaneously include conductive and radiative near-field heat conduction, it would be difficult to quantitatively explain the experimental data. However, modifications were made to the conductive heat transport physics aimed at qualitatively explaining the temperature gradient without the need to rely on different thermal conductivity regions. To this end, the heat generated by Joule heating inside the Pd heater wire was altered to mimic a near-field phenomena. Under normal conditions, the heat source generated from the flow of electrons is bound completely within the Pd heater wire and drops to zero at its immediate vicinity with the nitride, where the total heat source can be represented by a rectangular cross-section with its width corresponding to the width of the heater wire. However, to simulate distance-dependent heat transport enhancement with respect to the position of the heater wire the heat source is modified by two-dimensional convolution with a Gaussian function, which

delocalizes the heating directly into the SiN, with a strength decaying with distance away from the heater wire.

To correctly modify the Q_{dc} term, the joule heating finite element model was evaluated by analyzing the electric model separately from the thermal model. First an electric model was used to calculate the amount of heat generated within the wire, Q_{dc}. Next the Q_{dc} was extracted from this model and its Fourier transform obtained. Using the product of this Fourier transform and that of a simple Gaussian function, *f(x)*, the Q_{dc} was blurred out from the well-defined boundaries of the heater wire. In the study the function is defined as

$$f(x) = e^{-\frac{((X-X_0)^2+(Y-Y_0)^2)}{\sigma^2}} \tag{6.7}$$

Where X and Y indicate the position of the center of the peak and σ controls the width of the distribution. Afterwards, an inverse Fourier transform produces the convoluted heat source to use as a modified input in a thermal model of heat conduction based on the unmodified thermal conductivities of the device.

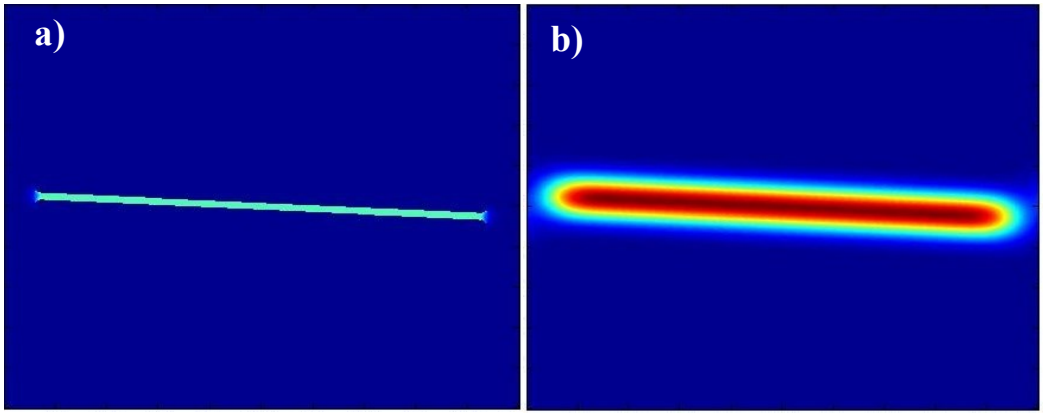

Figure 6.26: (a) The heat generated within the limits of the nanowire. (b) Blurring of the heat using 2D convolution with a Gaussian function.

Expanding the heat source serves to simulate the near-field radiation, in which case it should eliminate the need for a spatially dependent k_{SiN}. Consequently the correct model will depend on a fixed k_{SiN} value, which quantifies the conductive heat dissipation property of the SiN, and a Gaussian σ value which indicates the decay length of the evanescent waves. However, this simplified near-field conduction model was unable to produce such a result as it lacked the correct boundary condition at the Pd interface. Blurring the heat source not only serves by simulating near-field heating of the substrate but also expands the heat generated onto the Pd contacts. However, due to the large thermal conductivity of the Pd, much of the heat is quickly dissipated away from the nanowire, as the σ value is increased. As shown in table 6.2, as σ increases, the k_{SiN} values decrease precipitously in order to maintain the same temperature profiles as the delocalized heating transfers heating power into the Pd metal leads. The unphysically low k_{SiN} values indicate a notable failure of the model. Therefore, to accurately use the Gaussian method to simulate the near-field phenomena one must impose a boundary condition at the interface of the Pd contacts, such that the heat is only expanded only onto the substrate. Such an improved simulation of near-field effects is unfortunately outside the scope of this dissertation.

σ	0	30	300	1000	3000	5000
k_{SiN} ($W\ m^{-1}\ K^{-1}$)	3.6	3.46	3.38	1.36	0.027	0.0087

Table 6.2: Extracted k_{SiN} at 190mV for different σ values

6.5: Thermal Coefficient of Resistance, α

Further evidence that suggests the need for a more advanced thermal model in understanding the heat dissipation in our devices can be found by close examination of the simulated electrical parameters. As discussed above, the resistivity of the metal is subject to change due to thermal effects, the rate of which is defined by the coefficient α, the thermal coefficient of resistance. Within the experimental temperature range, the coefficient α should be constant as the resistance linearly increases with temperature [84]. Furthermore, since the thermal conductivity of the substrate dictates the temperature of the system, the extracted α will depend on the assigned k_{SiN} value. Expectedly, given a fixed k_{SiN}, a single α should accurately predict the correct *I-V* characteristics of the device for the entire range of voltages measured. However, if our model, as described in section 6.3.4 is altered to match the melting profile for each bias step then the corresponding α will also change (see figure 6.27), which is not physical. Consequently, it stands to reason that even though the thermal conductivity of the membrane can be used as a degree of freedom to attain the correct simulated melting profile, the physics governing it is flawed. Conversely, a near-field mechanism could potentially explain the variation in the temperature profile without requiring variations k_{SiN} or α.

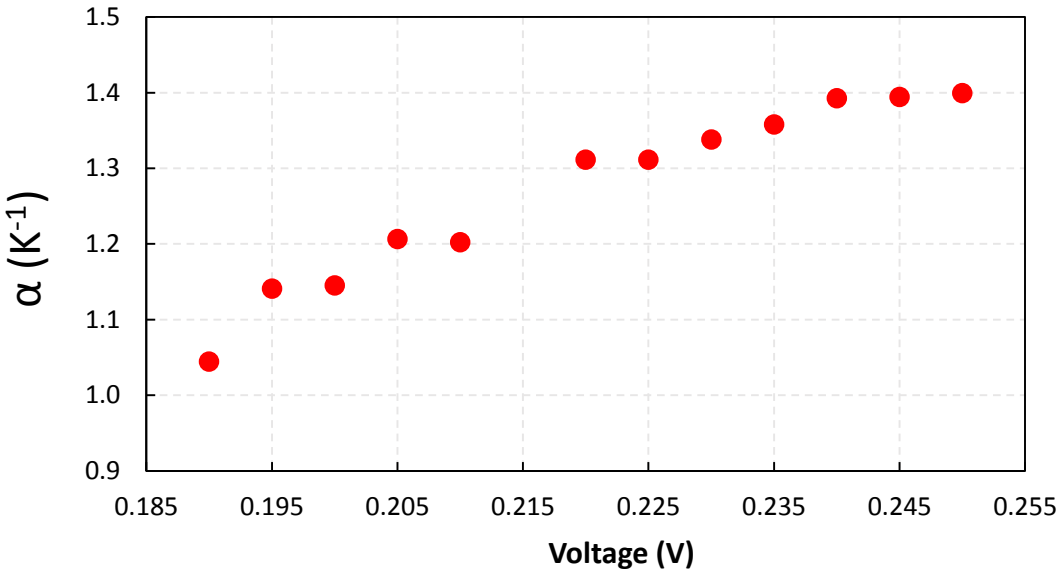

***Figure 6.27: Required change in the thermal coefficient of resistance to account for the change in k_{SiN}* for different applied voltages.**

6.6: Implication on Previous Results

The sensitivity of the described measurement procedure on measuring near-field thermal transport could be a remarkable future strength of the technique. Evidence of the near-field effects have only recently become apparent and as such were ignored in previous work. Consequently, it is important to evaluate the previous results by considering the possible influence of near-field radiation.

As discussed above, the evanescent surface waves will serve to provide enhanced heat transport. Simulating the experiments with a purely conductive heat transport model must compensate the additional heating from near-field effects. Consequently, the lattice thermal conductivity is overestimated and the extracted k_{SiN} values serve as an upper limit [63].

Previous measurements [1,2] also included passive and active CNT devices. The thermal boundary resistance of the CNT-SiN and CNT-Pd system was assessed based on the asymmetry in the melting profile due to enhanced thermal transport through the nanotube. The asymmetry was evaluated at equidistance positions from the heat source and demonstrated a reduction in the TBR by increasing the contact area of the nanotube via Pd deposition [1]. Since the strength of the near-field radiation decays exponentially with distance away from the heat source it is reasonable to assume the same amount of enhancement on either side of the heater wire, with and without the CNT, and therefore the relative TBR calculated should not change significantly, in a model that includes near-field effects.

The effects of near-field enhancement should also be evaluated for studies which rely on the CNT as the heat source. The thermal measurements of these

devices indicate a remote joule heating of the substrate via the nanotube's hot electrons. The outcome of a remote Joule heating phenomena is analogous to near-field radiation. In both models there is an enhanced heat transfer in addition to conductive thermal transport. Even though both mechanism have similar effects, they can not individually explain the observed experimental thermal profile. As described in section 5.2.2, the decrease in the remote joule heating parameter, β, for increasing voltages is a possible strong indicator of the presence of near-field enhancement. As the distance of the melting front increases for elevated voltages the relative strength of the evanescent near-field waves decreases which is manifested in decreasing β. However, a pure near-field model can not explain why only the In islands under the current carrying region of the nanotube melt and thus uniquely indicates the presence of remote Joule heating in addition to possible near-field enhancement. In addition, the results of active CNT devices [2] suggest that the nanotube stays cold as the substrate is heated. However, the presence of near-field effects may suggest that the nanotube does, in fact, heat up, although perhaps not enough to melt the islands. These results may indicate the presence of both near-field and remote heating effects and are collectively quantified in the β parameter in results presented here in chapter 5 and in reference 2. However, the presence of a near-field conduction mechanism alone is not enough to explain the prior results on remote Joule heating. Although near-field effects may partially compensate for the remote Joule heating effect, as described above, remote Joule heating remains as a necessary and significant component of any model to describe the results presented in [2].

Chapter 7: Conclusion

In conclusion we have provided conclusive evidence of remote joule heating of the supporting SiN membrane via the current carrying MWCNT with even greater confidence than in prior studies. The experimental melting profile in the crossed nanotube device can not be explained with traditional joule heating model and the results further necessitate a model with additional heat transfer mechanisms. From the observed temperature gradient of the substrate we can conclude that the hot electrons flowing in the nanotube are responsible for heating the substrate. The process results in a net energy loss for the accelerated electrons as the energy is transferred to thermal energy within the phonons of the substrate. In principle, such an event would result in a reduction in the electron mobility, which may be an indication of the onset of remote heating phenomena. However, our electrical measurement technique lack sufficient sensitivity to measure a reduction in mobility.

Due to the direct dependence of the remote heating mechanism on the energy of the electrons, we also explored the effects of varying potentials. Despite increasing the bias voltage of the electrons, we observed a reduction in the amount of remote heating, which may seem counterintuitive at first glance and hints at the presence of additional mechanisms which previously not taken into consideration. Motivated by the apparent reduction in the remote heating quantity we conduct a series of controlled experiments to quantify possible variations in the thermal conductivity of the substrate, k_{SiN}, due to temperature, stress, and beam exposure. From the simulations of our control experiments, we observe a variation in the k_{SiN} values with applied voltages, exhibiting an increase in the k_{SiN} for increasing voltage. Through a

series of simulations, the resulting candidates for such a variation for the thermal conductivity were analyzed and some excluded. However, the results strongly indicate a spatial dependence on the k_{SiN} which, with further considerations, would suggest an indication of near-field radiation.

From the combined simulated and experimental results, we believe we have demonstrated the electron thermal microscopy's remarkable sensitivity in measuring near-field thermal radiation. The ability to quantify enhancement due to near-field heating is of great scientific and engineering interest. Here, we propose future work which will take advantage of the sensitivity of the measurement technique to explore the near-field phenomena in addition to experiments with nanotubes, which will aim to further characterize the remote joule heating process.

7.1: Future Work

7.1.1: Near-field Enhancement Heat Transport

We propose an experimental setup which can directly compare near-field heating in different surfaces. The proposed device will be identical to the Pd heater wire devices measured previously with the addition of slits on either the right or left side of the wire. The fabrication of the slits will consist of an additional e-beam lithography step followed by an etching process. The length of each slit will be 0.5 μm with its width dictated based on the resolution of the lithography. The slits will be patterned parallel to the heater wire, at less than 500nm away, with an end to end distance of 500 nm. A series of 5 such lines of discontinuous slits will be patterned on one side of the heater wire which will drastically alter the nature of the evanescent

waves. Consequently, such a device will produce a noticeable asymmetry in the melting profile due to varying degree of the near-field heating.

7.1.2: Polariton vs. Plasmon

It is believed that polar substrates undergo a much greater near-field enhancement [14]. As such, it would be obvious to conduct the experiments on non-polar membranes, such as silicon or diamond. However, fabricating electron transparent non-polar membranes is of great difficulty. Instead, it is possible to evaluate the effects of plasmons vs. polaritons on the nature of the near-field radiation by relying on the slits once again. However, to study the influence of plasmon induced changes in the surface waves we propose to omit etching the slits and instead deposit 30nm of metal. By comparing such a device with an etched slit experiment, we can gain further insight into the mechanism of heat transfer via the evanescent waves (see figure 7.1).

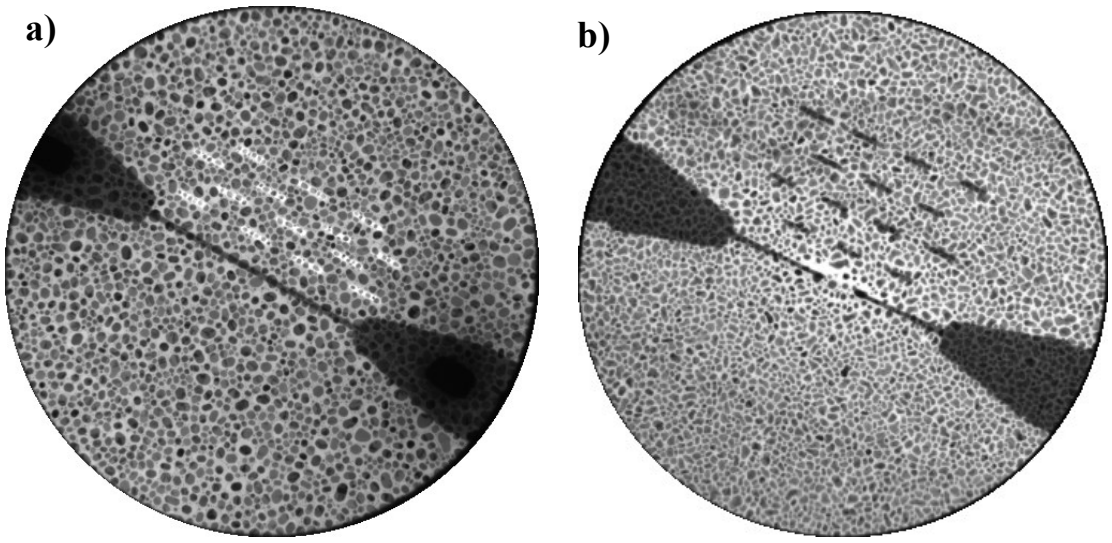

Figure 7.1: Bright field images of a device with slits (a) and with Pd gratings (b).

From preliminary experiments conducted on SiN membranes with slits (figure 7.2a) and Pd grating (figure 7.2b), one can observe that the presence of the slits reduces the heat transport. This may be explained in terms of a reduction in the thermal conductivity of the membrane at the thinner regions. However, in the device with the Pd grating, one can clearly notice that the metal impedes the heat transport as seen in figure 7.2b, despite the higher thermal conductivity of the Pd. The results suggest that the metal behaves as a mirror in reflecting the heat flow and is possibly imposing a boundary condition on the evanescent near-field radiation propagating on the membrane.

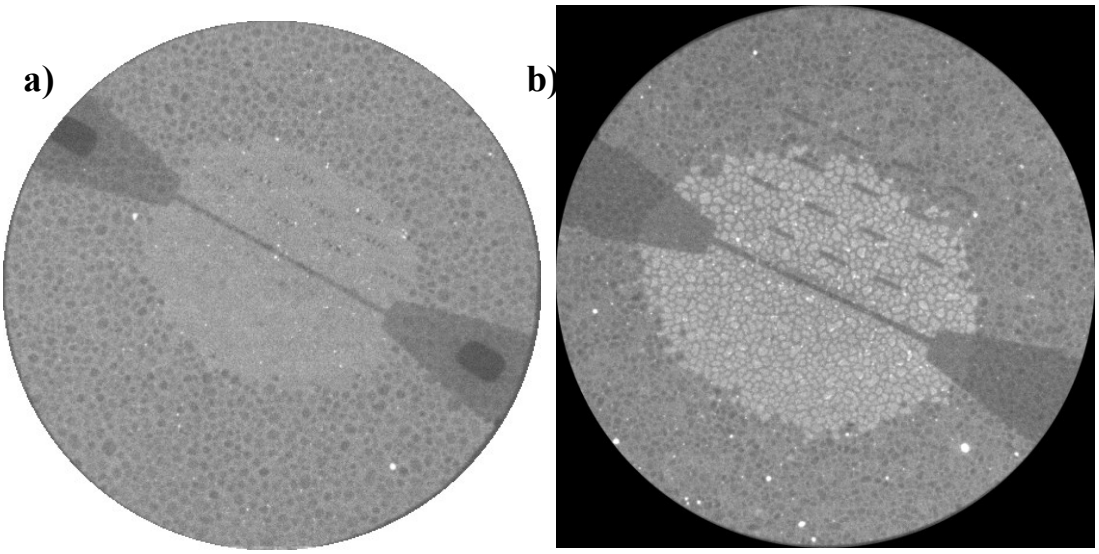

Figure 7.2: Melting profile of the device with slits (a) and with Pd gratings (b).

7.1.3: Correction of the Gaussian Model

With the possible ability to observe near field radiation, we propose the development of a model to qualitatively describe the near-field heat transfer in a given mode. Similar to our efforts to simulate the near-field phenomena we propose

using a conductive heat transfer model and blurring the heat generated within the wire by a Gaussian function. However, to avoid the dissipation of the heat from the electrical contacts, with high thermal conductivity, the heat source must be subtracted from those regions. The physical origin of this correction would be the electromagnetic boundary condition at the conducting metal surfaces, which would typically be reflective for both far-field and near-field radiation. In this model, the total heat must be normalized and added to the system, so as not to violate conservation of energy. Using such a model, it is possible to simulate heat transfer mechanism which has a dimension intensity with increasing distance from the source, characterized by the width of the Gaussian, which behaves similarly to near-field radiation.

7.1.4: Variation in Remote Joule Heating due to Applied Voltage

Furthermore, by quantifying the near-field heating in our devices we can subtract it from the crossed nanotube device and understand the variation in the strength of the remote heating phenomena as a function of applied voltage. The accuracy of a near-field model can be tested by applying it to the results in chapter 6, by incorporating a correct near-field model the temperature gradient of the substrate should be accurately reproduced for all applied voltage values with a single k_{SiN} value. In addition, such a model can then be used to separate the effects of near-field heat transport from remote Joule heating in an effort to study the voltage dependence of the remote Joule heating phenomena.

Moreover, it is believed that remote joule heating will only occur if the electrons have enough energy to couple to the phonons of the substrate. As such, the

remote heating process should not exist at low bias voltages. Studying the low bias regime is difficult given the current experimental setup, as the melting of indium requires an elevated temperature and higher operation power which may not be reached at the low bias regime. Although replacing the In with a low melting point metal might be the most obvious approach, doing so will lead to many challenges as there are few metals with the desired benefits of In. Instead, it would be possible to elevate the temperature of the substrate to few degrees below the melting point of In such that a small bias will be sufficient to melt the islands thus allowing the study of the low bias regime. These devices will require the fabrication of additional heater wires in the vicinity of the CNT which will act as heating the substrate. Evaluation of such devices would not have been possible prior to the work outlined in this dissertation as enhancement from near-field heating would have overcrowded the remote heating process. Consequently, it is important to quantify the nature of possible near-field heating effects in order to study variation in the strength of remote joule heating.

Furthermore, we have discussed the decrease in electron mobility due to loss of energy in the electron system within the nanotube. Although our measurements do not have the necessary sensitivity to measure the change in mobility, it would be possible to use high sensitivity electrical measurements to pinpoint the voltage necessary to induce coupling of the electrons with the substrate. The process can be observed by a reduction in conductance of the nanotube.

Bibliography

1. K. H. Baloch, N. Voskanian, J. Cumings, APL 97, 061901 (2010)
2. K. H. Baloch, N. Voskanian, M Bronsgeest, J. Cumings , Nature Nano. (2012)
3. S. Berber, Y. K. Kwon, and D. Tomanek, Phys. Rev. Lett. 84, 4613 (2000).
4. Durkop, T.; Getty, S. A.; Cobas, E.; Fuhrer, M. S. Nano Lett. 4, 35–39 (2004).
5. S. J. Tans, R. M. Verschueren, and C. Dekker, Nature, vol. 393, pp. 49-52, (1998).
6. A. Javey, P. Qi, Q. Wang, et al., Proc. Natl. Acad. Sci. 101, 13408 (2004).
7. J. Kong, J. Cao, and H. Dai, Applied Physics Letters, vol. 80, pp. 73, (2002).
8. M. J. Biercuk , M. C. Llaguno , M. Radosavljevic , J. K. Hyun , A. T. Johnson and J. E. Fischer, Appl. Phys. Lett., 80, 2, (2002)
9. E. Pop, Nano Res. 3, 147 (2010).
10. Cahill et al. J. Appl. Phys., 93, 2 (2003).
11. C. Kittel, H. Kroemer, Thermal Physics, W. H. Freeman and Company. (2000) .
12. E. T. Swartz, R. O. Pohl, Rev. Mod. Phys., 61, 3 (1989).
13. A. A. Balandin, IEEE Potentials, 21 (2002).
14. R. Siegel, J. Howell. Thermal Radiation Heat Transfer, Taylor and Francis, 4th Edition, (2002).
15. M. Planck. The Theory of Heat Radiation, Dover Publications, New York, (1991).
16. M. F. Modest. Radiative Heat Transfer, Academic Press, 2nd Edition, San Diego, (2003).

17. A.I. Volokitin, B.N.J. Persson. Physical Review B 63, 205404, (2001).

18. D. Polder, M. Van Hove. Physical Review B 4(10), 3303-3314, 13 (1971).

19. S.Basu, Z.M. Zhang and C.J. Fu International Journal of Energy Research 33(13), 1202-1232, (2009).

20. A. I. Volokitin, B. N. J. Persson, Rev. Mod. Phys. 79, 1291–1329 (2007).
21. S. Ijima. Nature, 354, 56 (1991).

22. L.V. Radushkevich, V. M. Lukyanovich, Zurn Fisic Chim. 24, 111, (1952).

23. R. H. Baughman, A. A. Zakhidov, W. A. Heer. Science, 297, 5582 (2002).

24. R. Martel, V. Derycke, C. Lavoie, J. Appenzeller, K. K. Chan, J. Tersoff, Ph. Avouris, Phys. Rev. Lett. 87, 256805, (2001).

25. Dresselhaus et all. Phil. Trans. R. Soc. Lond. A, 362 2065-2098 (2004).

26. K. S. Novoselov, A. K. Geim, S. V. Morozov, D. Jiang, Y. Zhang, S. V. Dubonos, I. V. Grigorieva, A. A. Firsov, Science, 306, 666–669 (2004).

27. M. S. Dresselhaus, G. Dresselhaus, P. C. Eklund, Science of Fullerenes and Carbon Nanotubes. Academic Press, San Diego, CA, (1996).

28. P. L. McEuen, M. S. Fuhrer, and H. Park IEEE Trans. Nanotechnol. 1, 78 (2002).

29. R. Saito, M. Fujita, G. Dresselhaus, and M. S.Dresselhaus, Applied Physics Letters,vol. 60, pp. 2204-6, (1992).

30. Z. Yao, C. Dekker, and P. Avouris, in Topics in Applied Physics, vol. 80, M. S. Dresselhaus, G. Dresselhaus, and P. Avouris, Eds. Berlin: Springer, 147-171 (2001).
31. F. Kreupl, A. P. Graham, M. Liebau, et al., in Proc. International Electron Devices Meeting (IEDM) (IEEE, San Francisco, CA, 2004).

32. S. Berber, Y. K. Kwon, and D. Tomanek, Phys. Rev. Lett. 84, 4613 (2000).

33. C. Yu, L. Shi, Z. Yao, D. Li, A. Majumdar,. Nano Lett. 5, 1842–1846. (2005).

34. J. Yu, R. K. Kalia, and P. Vashishta J. Chem. Phys. 103, 6697 (1995).

35. J. Hone, M. Whitney, C. Piskoti, and A. Zettl, Phys. Rev. B 59, R2514. (1999).

36. Yamamoto, T., S. Watanabe, and K. Watanabe, Phys. Rev. Lett. 92, 75502. (2004b).

37. J. Hone, B. Batlogg, Z. Benes, A. T. Johnson, and J. E. Fischer, Science 289, 1730 (2000).

38. E. Pop, D. Mann, Q. Wang, K. E. Goodson, and H. Dai, Nano Lett. 6, 96. (2006).

39. W. J. Evans, M. Shen, and P. Keblinski, Appl. Phys. Lett. 100, 261908 (2012).

40. M. A., Panzer, and K. E. Goodson, J. Appl. Phys. 103, 094301 (2008).

41. Z.-Y. Ong, and E. Pop, Phys. Rev. B 81, 155408 (2010).

42. R. E. Walkup, P. Avouris, Phys. Review B 58, 13870 (1998).

43. V.Bahadur, J. Xu, Y. Liu, T. S. Fisher, J. Heat Transfer 127, 664 (2005).

44. Z. Yao, C. L. Kane, C. Dekker. Phys. Rev. Lett., 84, 2941–2944 (2000).

45. G. D. Sanders, et al. J. Phys.: Condensed Matter 24, 4977–4994 (2012).

46. V. Perebeinos, S. V. Rotkin, A. G. Petrov, and P. Avouris, Nano lett. 9, 1, 312 (2009).

47. D. G. Cahill, P. V. Braun, G. Chen, D. R. Clarke, S. Fan, K. E. Goodson, P. Keblinski, W. P. King, G. D. Mahan, A. Majumdar et al., Appl. Phys. Rev. 1, 011305 (2014).

48. Kim, P., L. Shi, A. Majumdar, and P. L. McEuen, Phys. Rev. Lett. 87, 215502 (2001).

49. M. T. Pettes, and L. Shi, Adv. Funct. Mater. 19, 3918 (2009).

50. M. Fujii, X. Zhang, H. Xie, H. Ago, K. Takahashi, T. Ikuta, H. Abe, and T. Shimizu, Phys. Rev. Lett. 95, 065502 (2005).

51. I. K. Hsu, R. Kumar, A. Bushmaker, S. B. Cronin, M. T. Pettes, L. Shi, T. Brintlinger, M. S. Fuhrer, and J. Cumings, Appl. Phys. Lett. 92, 063113 (2008).

52. X. Huang, J. Wang, G. Eres, and X. Wang, Carbon 49, 1680 (2011).

53. V. V. Deshpande, Hsieh, S.; Bushmaker, A. W.; Bockrath, M.; Cronin, S. B.. Phys. Rev. Lett., 102, 105501 (2009).

54. A. W. Bushmaker, V. V. Deshpande, M. W. Bockrath, and S. B. Cronin, Nano Lett. 7, 3618 (2007).

55. Q. Li, C. Liu, X. Wang, and S. Fan, Nanotechnology 20, 145702 (2009).

56. P. G. Collins, M. Hersam, M. Arnold, R. Martel, and P. Avouris, Phys. Rev. Lett. 86, 3128 (2001).

57. H. Y. Chiu, V. V. Deshpande, H. W. C. Postma, C. N. Lau, C. Mikó, L. Forró, and M. Bockrath, Phys. Rev. Lett.95, 226101 (2005).

58. E. Pop, Nanotechnology, 19, 295202 (2008).

59. D. G. Cahill, Rev. Sci. Instrum. 61, 802 (1990).

60. T.-Y Choi, D. Poulikakos, J. Tharian, and U. Sennhauser, Nano Lett. 6, 1589 (2006).

61. Z. Wang, D. Tang, X. Zheng, W. Zhang, and Y. Zhu, Nanotechnology 18, 475714 (2007).

62. L. Shi, J. Zhou, P. Kim, A. Bachtold, A. Majumdar, P. L. McEuen, J. Appl. Phys., 105, 104306 (2009).

63. T. Brintlinger, Y. Qi, K. H. Baloch, D. Goldhaber-Gordon, and J. Cumings, Nano Lett., 8(2), 582 (2008)

64. E. Hecht, Optics 4th Ed. Addison-Wesley Reading MA (2003).

65. P. Hawkes, The beginnings of Electron Microscopy. Academic Press. (1985).

66. R. Egerton, Physical principles of electron microscopy. Springer (2005).

67. D. B. Williams and C. B. Carter, Transmission Electron Microscopy, Plenum Press, New York (1996).

68. L. Reimer, H. Kohl, Transmission Electron Microscopy: Physics of Image Formation. Springer (2008).

69. K. H. Baloch, Ph. D. Thesis, Dept. of Chemical Physics, University of Maryland. (2010)

70. SiN membranes are obtained from Silson Ltd.

71. Aqua Save is sulfonated polyoniline obtained from Rayon Mitsubishi

72. MWCNTs are obtained from Sigma-Aldrich Inc.

73. N. W. Ashcroft, N. D. Mermin, Solid State Physics, 1st Ed, Cengage Learning (1976)

74. T. Hertel, R. E.Walkup, P. Avouris, Phys. Rev., B 58 (20), 13870–13873, (1998).

75. E. Pop, D. Mann, J. Cao, Q. Wang, K. E. Goodson, and H. J. Dai, Phys. Rev. Lett. 95, 155505 (2005).

76. J. Y. Park et al., Nano Lett. 4, 517 (2004).

77. C. L. Kane, E. J. Mele, R. S. Lee, J. E. Fischer, P. Petit, H. Dai, A. Thess, R. E. Smalley, A. R. Verschueren, S. J. Tans, C. Dekker, Europhys. Lett., 41, 683 (1998).

78. M. P. Anantram, Phys. Rev. B, 62, R4837 (2000).

79. B. Bourlon, C. Miko, L. Forró, D. C. Glattli, and A. Bachtold, Phys. Rev. Lett. 93, 176806 (2004).

80. P. C. Collins, M. S. Arnold, P. Avouris. Science 292 706 (2001).

81. P. G. Collins and P. Avouris, Appl. Phys. A, vol. 74, pp.329 -332 (2002).

82. P. Castrucci, C. Scilletta, S. Del Gobbo, M. Scarselli, L. Camilli, M. Simeoni, B. Delley, A. Continenza, M. De Crescenzi Nanotechnology, 22.115701/115701–115701/115708 (2011).

83. A. M. Marconnet, M. A. Panzer, K. E Goodson,. Rev. Mod. Phys. 85, 1295–1326 (2013).

84. CRC Handbook of Chemistry and Physics, 84th Ed. W. M. Haynes. CRC Press: Boca Raton, FL, (2003).

85. S.M. Shivaprasad, L.A. Udachan, M.A. Angadi Phys. Lett., 78A, 187 (1980).
86. Y. Hanaoka, K. Hinode, K. Takeda, and D. Kodama, Mater. Trans. 43, 1621 (2002).

87. D. G. Cahill, W. K. Ford, K. E. Goodson, G. D. Mahan, A. Majumdar, H. J. Maris, R. Merlin, and S. R. Phillpot, J. Appl. Phys. 93, 793 (2003).

88. G. Bakan, L. Adnane, A. Gokirmak, H. Silva, H.. J. Appl. Phys. 112, 063527 (2012).

89. M. von Arx, O. Paul, H. Baltes, J. Microelectromech. Syst. 9, 136 (2000).

90. M. T. Alam, M.P. Manoharan, M.A. Haque, C. Muratore, A. Voevodin, J. Micromech. Microeng., 22, 045001 (2012).

91. R. C. Picu, T. Borca-Tasciuc, M. C. Pavel, J. Appl. Phys. 93, 3535-9 (2003).

92. P.J. French, P.M. Sarro, R. Mallee,, E.J.M.Fakkeldij,,R.F. Wolffenbuttel Sensors Actuators A 58 149–57 (1997).

93. W. Chuang, T. Luger, R. K. Fettig, R. Ghodssi, J. Microelectromech. Syst. 13 870-9 (2004).

94. A. Kaushik, H. Kahn, A. H. Heuer, J. Microelectromech. Syst. 14, 359-67 (2005).

95. F. P. Incropera, D. P. Dewitt. Fundamentals of Heat and Mass Transfer, John Wiley & Sons, 4th Edition, (1996).